Simulations of Daily Extremes and Diurnal Variations of Precipitation over East and Southeast Asia by Climate Models

LUI, Yuk Sing

A Thesis Submitted in Partial Fulfillment

of the Requirements for the Degree of

Master of Philosophy

in

Earth and Atmospheric Sciences

The Chinese University of Hong Kong

September 2017

Thesis Assessment Committee

Professor WONG, Teng Fong (Chair)

Professor TAM, Chi Yung Francis (Thesis Supervisor)

Professor LAU, Ngar Cheung Gabriel (Committee Member)

Professor ZHOU, Wen (External Examiner)

Abstract of Thesis titled:

Simulations of Daily Extremes and Diurnal Variations of Precipitation over East and Southeast Asia by Climate Models

Submitted by **LUI, Yuk Sing**

for the Degree of **Master of Philosophy in Earth and Atmospheric Sciences**

at The Chinese University of Hong Kong in **September 2017**.

Abstract

Monsoon systems, tropical cyclones (TC), and diurnal rainfall are some of the most important meteorological phenomena that contribute to summertime extreme precipitation over East to Southeast Asia. How well these phenomena are reproduced by numerical models, and how they will be modulated by climate change are the two research questions this thesis seeks to explore. This thesis herein uses two different methods for obtaining high-resolution climate simulations.

The first method is to drive high-resolution atmospheric global climate models (AGCMs) using prescribed sea surface temperature, which is sometimes referred to as "global downscaling". Based on simulations from a 20-km Meteorological Research Institute atmospheric general circulation model (MRI-AGCM), we have examined the impacts of climate change on precipitation extremes in the Asian monsoon region during boreal summer. The AGCM projected robust increases of the summertime extreme precipitation particularly over Eastern China, the Meiyu-Baiu rainband, Bay of Bengal and Central India at the end of 21st century. Besides, the AGCM projected an increase of accumulated tropical cyclone rainfall over northern South China Sea and southeastern China, and a decrease east of the Philippines and in southern Japan in the globally-warmed future, which can be attributed to the more intense TC rainrate and pronounced suppressed TC activity, respectively. In general, non-TC weather

systems are the main contributor to enhanced precipitation extremes in various locations, except over Taiwan where TC-related rainfall is more important.

Another method is to dynamically downscale GCM outputs by using regional climate models (RCMs), whose skills to capture various physical processes must be evaluated against observations beforehand. Therefore, in the second part, we examine the sensitivity of precipitation simulations over the CORDEX-Southeast Asia domain to the cumulus convection scheme used in the Regional Climate Model version 4 (RegCM4). With the ERA-Interim reanalysis as lateral boundary conditions, simulations using the Emanuel cumulus convection scheme everywhere (EE), and those using a "mixed convection scheme" (MC; namely with the Emanuel scheme over ocean and the Grell scheme with Arakawa Schubert(AS)-type closure over land), have been compared for the 2001-2010 period. EE and MC are equally good in capturing JJA mean and the annual cycle of precipitation. However, Empirical Orthogonal Function (EOF) analysis indicates that MC undermines the representation of diurnal cycle (DC) of precipitation by weakening the second EOF mode. The latter corresponds to afternoon peaks over coastal inland regions of western Indochina and southeastern China, and evening/midnight peaks over mountain ranges of Sumatra, Borneo and New Guinea. Further analyses reveal that underestimated peaks over former regions are mainly related to reduced low-level air temperature as well as enhanced cloud cover around 1200 to 1500 local time; whereas those over latter regions are associated with suppressed low-level moisture convergence due to poor representation of interaction between local circulation and complex terrain around 1800 to 0000 local time.

摘要

季風系統、熱帶氣旋及日變化降雨, 是導致東亞至東南亞地區夏季極端降水的重要氣候現象。數值模型如何描述這些現象, 以及這些現象在人為氣候變遷下會怎樣改變, 是本論文的首要研究方向。在此, 本論文利用兩種不同的高解析度氣候模擬方法。

第一種方法是以指定的表面海溫去運行高解析度大氣模型，簡稱為全球降尺度。透過分析日本氣象廳氣象研究所的二十公里解析度大氣模型（MRI-AGCM）的數據，我們探討氣候變遷對亞洲季風地區的夏季極端降水的影響。大氣模型預測在本世紀末，夏季極端降水在華東地區、日本週邊的梅雨區、孟加拉灣及印度中部會有顯著增強。此外，大氣模型預測在全球暖化影響下，隨著颱風降水強度增強，夏季颱風累積雨量在南海北部和中國東南部地區增加，而颱風活躍度降低，會導致菲律賓以東和日本南部的累積雨量減少。普遍來說，各地區極端降水增強的主要原因是非熱帶氣旋的天氣系統, 其中一個例外是台灣, 熱帶氣旋對其夏季極端降水更為重要。

第二種方法是利用以全球模式為背景做動力降尺度的區域模式模擬。區域模式能否正確地表現各種物理過程尤其重要，因此，在第二部份，我們評估區域模式（RegCM4）在模擬東南亞降水方面，對積雲參數法的敏感性。透過利用 ERA-Interim 再分析數據作為側面邊界條件，及分別利用 Emanuel 積雲參數法（下稱為 EE）和「混和」積雲參數法（下稱為 MC），我們對比了這兩組敏感性實驗在 2001 至 2010 期間的結果 。這兩組實驗在夏季平均和季節變化降水方面的表現均較為理想。不過，我們透過經驗正交函數分析，發現 MC 低估第二個模，以致在日變化降水的模擬欠佳。第二個模對應的是， 印支半島西

部和中國東南部沿海內陸地區的下午峰值，以及蘇門答臘、婆羅洲和新幾內亞山脈地區的深夜峰值。透過進一步分析，我們發現峰值被低估的主要原因是，對於前者地區，低層氣溫在當地時間約 1200 至 1500 降低及雲量增多；對於後者地區，因當地環流和地勢的相互作用的表現欠佳，以致低層的水份輻合在當地時間約 1800 至 0000 被抑制。

Acknowledgement

First of all, I would like to express my gratitude to my supervisor, Professor Francis Tam. He is open-minded to research ideas, he always encourages his students to explore different research fields and gives them considerable amount of freedom. Meanwhile, he always guides one back on the right track or inspires one with new insights at the right moment. Without his support and guidance, this thesis would not have been possible.

Thanks to the supports from both the Department and Professor Francis Tam, during my 2-year study in CUHK, I was given many opportunities to attend workshops and international conferences, where I can present my research work to others, to interact with professionals and scientists, and more importantly to explore the frontiers' research areas. They were remarkable and unforgettable experiences for a postgraduate student and they are lessons that one cannot learn from lectures.

I am also grateful to my thesis assessment committee members, Professor Gabriel Lau and Professor Wong, for reviewing and commenting on my work. In particular, I would like to show my appreciation to Professor Gabriel Lau for generously sharing us the MRI-AGCM dataset. At last, I would like to thank everyone that I worked with in this two years, especially the group members in our research group. It had been wonderful working with, debating with and learning from them in the past two years.

Table of Contents

List of Figures

List of Tables

Chapter 1

Introduction

Numerical modelling is a process to solve physically-based equations by appropriate simplification of reality. As in many scientific fields, it is very useful in many areas of climate studies, especially where experiments are either costly, undesirable or impossible. For example, reanalysis and data assimilation involve the use of models to create a spatiotemporally-complete and dynamically-consistent estimate of our climate system, while it is not practical to build a very dense network of radiosondes or remote-sensing stations around the globe. Furthermore, climate engineering such as stratospheric aerosol injection is usually not welcomed; experimental studies can only be achieved through modelling. More importantly, numerical simulations can be used to test our scientific understanding of various processes as well as to project the future. For instance, we can compare simulations with and without the urban landscape to estimate the urbanization effect, or we can compare present-day and future-day simulations to assess the potential impact of global warming.

1.1 Regional-scale climate modeling

Typical GCMs have a horizontal resolution of 150 to 300 km. They are particularly useful for projecting large-scale features of climate change, given a future greenhouse gas emission (or concentration) scenario. However, they are not able to capture extreme events as well as responses due to local forcings since any signal beyond their highest resolved wavelength is truncated (e.g. Giorgi et al. 2009). Realising such spatial-scale gap between information provided by global climate models (GCMs) and inputs needed for policy-making and engineering purposes, scientists make use of

various techniques to relate GCM projections to regional impact assessment studies to bridge such a gap (from a scale of ~200km to a scale of 50 km or less).

One of these regional-scale modelling techniques is to run a stand-alone atmospheric component of GCM (i.e. AGCM) at very high resolution by prescribing sea surface temperature (SST) patterns, which is sometimes referred as “global downscaling”. Another two techniques involve the concept of “downscaling”. They are, namely, “statistical downscaling” and “dynamical downscaling”. The former statistically relates coarse GCM outputs to the observed local climate variables, by assuming stationary relationship between them; whereas the latter nests a high-resolution RCM within the output from a GCM (or an ensemble of GCMs), by feeding the RCM with large-scale GCM data as boundary conditions (e.g. Wilby and Wigley 1997).

Climate models with better representation of topographical forcing and land-sea contrast, and more sophisticated internal physical processes can add mesoscale features that are absent or poorly represented in the large-scale flow of GCMs. These “added values” include topographic rainfall, extreme precipitation, tropical cyclone activity, to name but a few (e.g. Giorgi 2006). However, note that RCMs are not intended to strongly modify the large-scale flows of GCMs and they are equivalently important in regional-scale climate studies; otherwise, it is more or less “garbage in, garbage out”.

1.2 Cumulus convection parameterization

Due to coarse resolution of grid-point models or finite wavenumbers for spectral models, small-scale (sub-grid) yet important physical processes cannot be represented explicitly in model environment. Therefore, physical parameterization schemes are

used to represent the sub-grid or complex processes by relating them to known large-scale (grid-resolvable) model variables. For example, the typical size of cumulus clouds is few hundred meters to few kilometers only, which means that their related processes cannot be resolved explicitly in GCMs and RCMs. They are small yet important in releasing latent heat and modifying the large-scale vertical sounding. Cumulus convection scheme serves to represent these sub-grid scale adjustment processes and reduce thermodynamic instability such that large-scale precipitation scheme is not overly activated. Different types of cumulus schemes are formulated with different triggering mechanisms, depiction of moist-convective processes and interaction with large-scale environment.

Three mass-flux type cumulus schemes are involved in this thesis. (1) Yoshimura scheme: is used in MRI-AGCM, which is based on Tiedtke scheme (Yukimoto et al. 2011). It is modified to allow multiple detailed entraining and detraining plumes to exist continuously between two Tiedtke-type convective updrafts. (2) Grell scheme: is an option in RegCM4, which is based on Arakawa-Schubert scheme (Grell 1993). It considers only a single updraft and modified to include a downdraft. Closure assumption on the rate of stabilization by the convection is needed, where two options are available, namely Arakawa-Schubert closure and Fritsch-Chappell closure. (3) Emanuel scheme: is another option in RegCM4 (Emanuel 1991; Emanuel and Živković-Rothman 1999). It allows convective drafts to move between all layers from cloud base to cloud top such that mixing in clouds is highly episodic and inhomogeneous, as opposed to a continuous entraining/detraining plume.

Grell scheme and Emanuel scheme have different triggering mechanisms: for the former, convection is activated when the vertical distance between the lifting

condensation level and and level of free convection is smaller than a specified threshold depth; whereas for the latter, a convection is activated when the level of neutral buoyancy is greater than the cloud base level. However, it should be noted that the difference between the two schemes is not limited to the triggering mechanism but also the representation of physical processes of a convection. Regarding the difference in their performance in activating convection, Emanuel scheme in general tends to generate more intense convection, dry out the atmospheric moisture more efficiently and produce more intense convective precipitation, as compared to Grell schemes (Zanis et al. 2009). A more efficient drying of the atmosphere also leads to reduced cloudiness and allows more shortwave radiation reaching the ground, thereby causing warmer low-level temperature and in turn reinforcing the convection.

1.3 Extreme precipitation

As compared to lower-moment climate statistics (e.g. climatological-mean precipitation), higher moment statistics such as moderately extreme precipitation is sometime of primary importance in climate impact studies. However, the terminology of precipitation extremes is usually broadly defined among these studies, where they could refer to various characteristics (e.g. percentile-based, duration-based and proportion-based) of the tail of precipitation's probability density function (PDF) or impacts caused by extreme events such as tropical cyclones (TCs; see Zwiers et al. 2013). In the former case, they can be characterized by both non-parametric (e.g. Expert Team on Climate Change Detection and Indices; ETCCDI; see Klein Tank et al. 2009) and parametric approaches (e.g. Generalized Extreme Value and gamma distributions; see Groisman et al. 1999; Semenov and Bengtsson 2002; Wilby and Wigley 2002; Kharin and Zwiers 2005; Min et al. 2011). In the latter case, projection

of TC activity can be conducted by either explicit simulation of TCs by AGCMs (e.g. Murakami et al. 2012; Zhao et al. 2012), dynamical downscaling by RCMs (e.g. Knutson et al. 2008; Emanuel 2013; Kossin et al. 2016) or genesis potential index analysis (e.g. Wu et al. 2014; Zhang et al. 2017).

It is generally understood that precipitation extremes increase at a significantly faster rate than the globally-mean precipitation (e.g. Easterling 2000; Meehl et al. 2000; Donat et al. 2016), although the rate of amplification of extremes may be weaker in model simulations than observations (e.g. Allan and Soden 2008). The Clausius-Clapeyron (CC) relation of vapor pressure states that the air's moisture-holding capacity increases by roughly 7% per 1K increase in lower-tropospheric temperature, which serves as a thermodynamic constraint on the scaling of precipitation extremes under global warming in regions where the nature of the flows does not change much (Pall et al. 2007). On the other hand, globally-averaged precipitation is constrained by the global energy budget and is expected to increase at a slower rate under global warming (Allen and Ingram 2002).

Different types of circulation systems (e.g. monsoon systems, TCs, frontal systems and diurnal cycle) can affect precipitation statistics in the Asian monsoon region (e.g. Qian et al. 2002; Ding and Chan 2005; Jiang and Zipser 2010), and their trends under global warming could be different (e.g. Chang et al. 2012; Huang et al. 2016). Thus, East to Southeast Asia is of particular interest to regional climate impact studies. Therefore, in chapter 2, we are motivated to study the impacts of climate change on summertime precipitation extremes in the Asian monsoon region, based on simulations from the high-resolution MRI-AGCM.

1.4 Diurnal precipitation

Another example of higher order climate statistics is diurnal variations of precipitation. The difference in mechanisms of DC over land versus sea is long recognized as a fundamental land-sea contrast in their atmospheric responses to radiative forcing (e.g. Yang and Slingo 2001). Over land areas, daytime surface shortwave heating increases low-level temperature and moisture, destabilizes the lower troposphere, and favors convection, thereby resulting a middle to late afternoon precipitation maximum over continental areas; whereas surface longwave cooling increases lower-tropospheric stability, suppresses convection and causes a precipitation minimum at night. Over oceanic regions, nighttime longwave cooling at cloud top outweighs that at cloud base, destabilizes the upper troposphere, and promotes deep convection, thereby leading to a midnight to early morning precipitation peak over the open ocean. On the other hand, shortwave heating at cloud top increases upper-tropospheric stability, suppresses convection and gives rise to a precipitation minimum during daytime (e.g. Randall et al. 1991)

However, this idealized picture is complicated by many other physical processes such as land-sea and mountain-valley breezes (e.g. Zhou and Wang 2006; Huang and Wang 2013), diurnal gravity waves (e.g. Shige and Satomura 2000) , modulation associated with intraseasonal variability (e.g. Ichikawa and Yasunari 2008), interaction between local and large-scale circulations (e.g. Yin et al. 2009) and tidal variations in the atmospheric pressure (e.g. Dai 2001). Thus, DC simulation can test model deficiencies on representing the fundamental physical processes with the use of parameterization schemes, in which cumulus convection has most direct impact. Thus, in chapter 3, we will examine the sensitivity of DC simulations over the

Southeast Asia to the cumulus convection schemes used in the RegCM4, in addition to seasonal mean and annual cycle.

Chapter 2

Future changes in Asian Summer Precipitation Extremes

2.1 Background

Climate change can bring great impacts on the society by changing both the frequency and intensity of extreme events. Many studies have been devoted to understanding how global warming might influence the characteristics of extreme precipitation, both in the global (e.g., Frich et al. 2002; Groisman et al. 2005; Alexander et al. 2006; Lau and Wu 2007; Zhang et al. 2011) and the regional/local perspectives (Qian and Lin 2005; Wang and Zhou 2005; Zhai et al. 2005; Chen et al. 2007). Researchers have also made use of climate models to project future changes in intense rainfall (Sun et al. 2007; Sillmann and Roeckner 2008; Jiang et al. 2012; Sillmann et al. 2013). Under a warmer background climate, precipitation extremes is expected to increase at a rate much faster than the globally-mean precipitation (Easterling 2000; Meehl et al. 2000; Allen and Ingram 2002; Donat et al. 2016). According to the Clausius-Clapeyron (CC) relation, the atmospheric moisture-holding capacity increases by about 7% per degree K increase in the lower-tropospheric temperature. Although the CC relation is useful for scaling precipitation extremes (Pall et al. 2007), other dynamic factors such as changes in the upward velocity may also be important for considering the impact of global warming on intense rainfall (IPCC 2012). In fact, super-Clausius-Clapeyron (superCC) scaling of sub-daily precipitation extremes in Europe and Japan have been reported (Lenderink and van Meijgaard 2008; Fujibe 2013).

It is well known that tropical cyclones (TC) can lead to very intense local precipitation. Over the western north Pacific (WNP) basin, TCs contribute significantly (about 11%) to the total rainfall during the peak TC season (Jiang and Zipser 2010). In the global mean sense, projections using high-resolution models give

an increase (decrease) of TC intensity and TC (frequency) by 2-11% (6-34%) at the end of 21st century (Knutson et al. 2010). Reductions in the global as well as the hemispheric mean TC numbers are probably robust and independent of model physics (Murakami et al. 2011). On the other hand, future changes of TC activity and TC-related rainfall for individual basins remain uncertain (Sugi et al. 2009; Knutson et al. 2010; Murakami et al. 2012). Several studies have identified a reduction of TC frequency in western North Pacific (WNP) in the globally-warmed future (Yokoi et al. 2009; Murakami et al. 2011; Kossin et al. 2016), while others project an insignificant change (Manganello et al. 2014). The study by Chang et al. (2012) suggests that trends of intense rainfall due to TC and non-TC systems can be drastically different. It is still unclear how extreme rainfall in the Asian monsoon region might be affected by TCs in the future climate.

Recently, Mizuta et al. (2012) and Murakami et al. (2012) examined the performance of the 20-km resolution atmospheric general circulation model of Meteorological Research Institute (MRI-AGCM3.2S) in capturing the Asian monsoon circulation as well as TC activities. The high-resolution AGCM is capable of simulating local features such as orographic precipitation (e.g. over Taiwan and Philippines), and large-scale phenomena such as the Asian summer monsoon. The model can also give realistic TC circulation and precipitation, TC occurrence frequency and its interannual variability in WNP (Murakami et al. 2012). Motivated by these results, this chapter makes use of the same AGCM to further examine the impact of global warming on rainfall statistics due to TC and non-TC weather systems.

2.2 Model experiments and methodology

2.2.1 AGCM experiments

The MRI-AGCM3.2S is based on the global spectral model developed by MRI of the Japan Meteorological Agency (JMA), and has been used for projecting the future climate, daily precipitation extremes and TC activity. It is a hydrostatic, primitive-equation model at the T959 resolution (corresponding to a grid size of ~20x20 km) with 64 unevenly-spaced vertical levels reaching 0.01 hPa in the vertical. The radiation scheme from the JMA operational model is used (JMA 2007), while cumulus convection is parameterized based on a mass-flux scheme (Yukimoto et al. 2011). The planetary boundary layer and the land surface are represented by the Mellor and Yamada (1974) scheme and the new Simple Biosphere (New-SiB) land surface model (Hirai et al. 2007), respectively. More detailed descriptions of this model were given by Mizuta et al. (2012). To realize the present day (PD) climate in this model, the AGCM was integrated with the Hadley Centre (Rayner et al. 2003) monthly-mean SST and sea ice concentration observed from 1979 to 2003. For the future globally-warmed (GW) climate, the averaged SST and sea ice projections by 18 models for the 2075-2099 period were used as the lower-boundary forcing (Murakami et al. 2012). These model projections were produced under the Special Report on Emissions Scenarios (SRES) A1B scenario, for the Coupled Model Intercomparison Project phase 3 (CMIP3) (Solomon et al. 2007). A schematic diagram of the experimental set-up is given in Fig. 2.1.

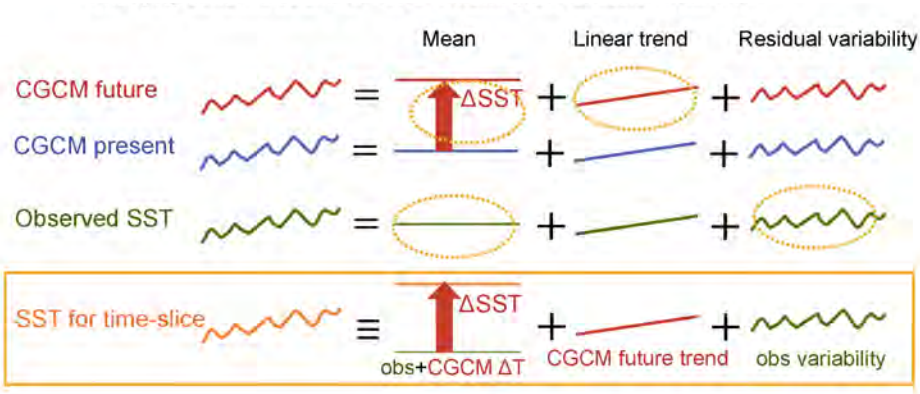

Fig. 2.1: Schematic diagram showing the set-up of the time-slice experiments for present-day (from 1979 to 2003) and globally-warmed future (from 2075 to 2099) (adopted from Kitoh 2015).

In order to evaluate the performance of the MRI AGCM in capturing the Asian monsoon circulation and TC activities, various observational and reanalysis products were used in this study. Here the precipitation products from the Tropical Rainfall Measuring Mission 3B42 version 7 (TRMM3B42v7) (Huffman et al. 2007) and the Asian Precipitation-Highly-Resolved Observational Data Integration Towards Evaluation version 1101 (APHRODITEv1101) for monsoon Asia (Yatagai et al. 2012) were selected for this purpose. The high spatial (0.25°×0.25°) and temporal (3-hourly) resolution TRMM3B42 dataset provides precipitation rate estimates by combining microwave, infrared measurements from multiple satellites as well as adjustment from gauge observations when possible (Huffman et al. 2007). In this study, the TRMM3B42 3hourly dataset is converted to daily precipitation rate for the period of 1998-2013. The APHRODITE dataset, which is produced by interpolating rain gauge observations, provides gridded daily precipitation rate over land within 0-55°N, 60-150°E, for the 1979-2003 period. Many studies have used this gauge-based dataset for studying the mean precipitation (Xie et al. 2007; Sohn et al. 2012) and extremes (Kamiguchi et al. 2010). Zhao and Yatagai (2014) performed a gauge data analysis

(adopted from APHRODITE) on daily precipitation records from the Chinese stations and found that the TRMM3B42v6 (an older version as compared to the one used in this study) rainfall estimates agree well with the gauge data, but notable underestimation is found in the western China. Also, they found that TRMM3B42 tends to overestimate the extreme daily precipitation over the southeastern China and underestimate the moderate precipitation over the northwestern China. In addition, the Joint Typhoon Warning Center (JTWC) best track data for TCs in WNP were used. Note that in this study, only TCs with maximum 1-min-sustained wind speed of 18 m s^{-1} or greater (i.e. tropical storm intensity) were considered for the JTWC data. Finally, upper-air meteorological variables such as winds and temperature from the Japanese 55-year Re-Analysis (JRA-55) monthly data were also used for model evaluation.

2.2.2 Methods for quantifying precipitation extremes

To assess the AGCM's performance in capturing extreme events and to quantify their changes, two commonly used indices were adopted to characterize intense rain rates. They are (i) the 95th percentile of daily precipitation during wet days (Prec95p), and (ii) the simple daily precipitation intensity index (SDII), which is defined as the accumulated precipitation divided by the number of rain days over a particular period of time. Throughout this study, wet (dry) days are defined as days with accumulated precipitation above (below) 0.1 mm. Besides using these empirical indices, we have also investigated the use of the parametric gamma distribution to characterize the daily mean precipitation during wet days. The two-parameter gamma distribution function is given by

$$f(x) = \frac{1}{\beta^{\alpha}\Gamma(\alpha)} x^{\alpha-1} e^{-x/\beta}, \qquad x, \alpha, \beta > 0 \tag{2.1}$$

where α and β are the shape and scale parameters respectively, and Γ(α) is the gamma function. The dimensionless α parameter characterizes the shape of the gamma distribution. When α < 1, the PDF is a hyperbolically decreasing distribution; when α = 1, it becomes an exponential function; in the limit of $\alpha \to +\infty$, it approaches a normal distribution. The parameter β represents the spread of the distribution, and can be interpreted as a measure of the variability of the daily mean precipitation. It is widely recognized that the gamma distribution provides a fairly good fit to the observed and also model-simulated (Groisman et al. 1999; Semenov and Bengtsson 2002; Wilby and Wigley 2002).Cho et al. (2004) reported that the PDF of daily precipitation rates from TRMM could be well represented by the gamma distribution, especially in wet regions. The parameters α and β can be estimated using the method of maximum likelihood. To test the goodness of fit of the gamma distribution, K-S test was applied in this study. It is used to test the null hypothesis that the data comes from a theoretical distribution function, based on the maximum difference between the empirical and theoretical cumulative distribution functions (CDF):

$$D_n = \max_x |F_n(x) - F(x)| \tag{2.2}$$

where $F_n(x)$ is the empirical CDF for a dataset with a sample size n and $F(x)$ is the theoretical CDF. The null hypothesis is rejected at a given significance level if the statistics exceed a critical value in a standard table. In general the shape parameter is spatially and temporally more stable compared to the scale parameter (Groisman et al. 1999; Semenov and Bengtsson 2002; Wilby and Wigley 2002). Here the scale parameter is included as one of the precipitation indicators in this study.

2.2.3 Deducing TC-related rainfall

We have also performed analysis of precipitation due to TC occurrences. Here TCs are tracked by the algorithm similar to that used by Murakami et al. (2012), which is based on 6-hourly AGCM outputs. A TC-like system in the model is identified whenever: 1) the local maximum 850 hPa vorticity exceeds 2.0×10^{-4} s^{-1}; 2) the local maximum wind speed at 850 hPa exceeds 17.0 m s^{-1}; 3) the sum of maximum temperature deviations at 300, 500 and 700 hPa exceeds 2.0 K, with the deviation defined as the departure from temperature averaged over a 10°×10° box centered at the position of maximum 850 hPa vorticity; 4) the maximum 850 hPa wind speed is larger than that at 300 hPa; and 5) the lifetime of the system must be 36 hours or more and the genesis must happen over the ocean. TC occurrence frequency (TCF) is defined as the total count of TC occurrences within each 5°×5° grid box for every 6 hours. The first detected position is defined as the TC genesis location, except at the boundaries of the study domain. TC genesis frequency is also defined similarly to TCF (whereas for JTWC 6-hourly best track data, the first detected position is defined as the location where the TC first attained a maximum 1-min-sustained wind speed of 18 m s^{-1} or greater, and TCF and TGF are defined accordingly in the same way). Finally, based on the positions of identified TCs at every 6 hours, we can further stratify precipitation over each grid box into TC and non-TC related rainfall. According to the criterion suggested in previous studies (Jiang and Zipser 2010), rainfall within 5° (i.e. roughly 500 km) from the TC center is considered to be associated with TCs. This way, 6-hourly precipitation can then be converted into TC and non-TC precipitation.

Fig. 2.2 shows the fraction of TC rainfall to total rainfall over MJJAS based on the AGCM outputs for the period of 1979-2003. The geographical distribution and the area-averaged value (0.102) are very close to those given by Jiang and Zipser

(2010) , although they focus on JJASON. Based on the TRMM-3B42 dataset, they found that the TC rainfall fraction ranges from around 0.2 to 0.4 in WNP basin and the area-averaged value is 0.11.

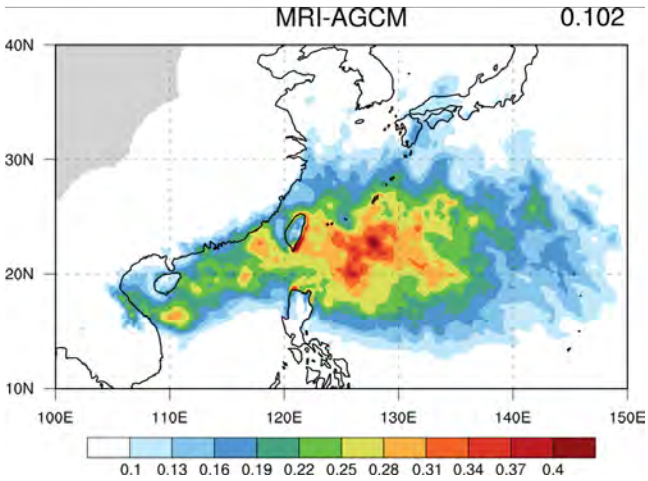

Fig. 2.2: The fraction of TC rainfall to total rainfall over MJJAS based on MRI-AGCM3.2S simulations for the period of 1979-2003. The TC rainfall fraction averaged over the domain of 0-50°N, 60-150°E is shown in upper right corner.

2.3 Simulations of present-day precipitation characteristics

Before examining the impact of global warming on precipitation characteristics, the capability of the MRI AGCM in capturing the summertime circulation and precipitation over the Asian monsoon area is first assessed. Fig. 2.3 shows the May-to-September (MJJAS) climatological mean precipitation rates computed from TRMM, as well those based on model simulations for the present climate. It can be seen that the AGCM can capture well the major monsoon rain features in this region, such as the western north Pacific Intertropical Convergence Zone (ITCZ), rainfall over BOB and the Indian subcontinent, and the Meiyu-Baiu rainbelt. It is noteworthy that orographic precipitation such as that over the Western Ghats, the foothill of Himalayas and the Philippines are also well reproduced by the model. On the other hand, values

over SCS to the Philippine Sea (southern coast of China and east of Japan) appear to be overestimated (underestimated). The biases over SCS to the Philippine Sea (southern coast of China and east of Japan) are probably related to the overestimated westerly (underestimated southerly) moisture flux to that region and to a lesser extent the slightly weaker westward extension of the subtropical high (see Mizuta et al. 2012). The precipitation rate averaged over 0-50°N, 60-150°E is about 5.84 mm day^{-1}, which is comparable to that based on TRMM for the same area (~5.50 mm day^{-1}). Also shown in Fig. 2.3 are the corresponding 850 hPa wind fields from JRA55 and those based on the AGCM run, for the same period of 1997-2003. The climatological mean low-level circulation is also reasonably captured by this model. Indeed, the simulated wind branches associated with the Indian and East Asian monsoon systems match well with those depicted in the JRA55 climatology.

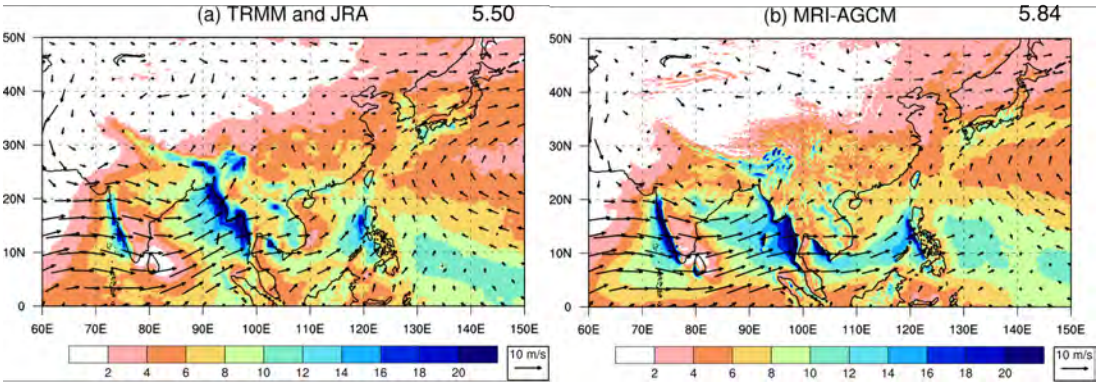

Fig. 2.3: Climatological mean daily precipitation rate (shading; units: mm day^{-1}) and 850hPa winds (see scale arrow at bottom right) over MJJAS based on (a) TRMM3B42v7 and JRA55 data for the 1998-2013 period, and (b) MRI-AGCM3.2S outputs for the period of 1979-2003. The precipitation rate averaged over the domain of 0-50°N, 60-150°E is shown in upper right corner of each figure.

We have also examined the month-to-month evolution of the precipitation field in the same domain. Fig. 2.4 compares the model-simulated May to September monthly-mean precipitation with observations. The AGCM can produce well the

seasonal progression of the Asian monsoon precipitation in different regions. In May, heavy rainfall is observed in BOB and north to northeastern part of the Indochina Peninsula, which roughly marks the onset of the Asian summer monsoon (Fig. 2.4a). In the meantime, enhanced precipitation is discernable in the Yangtze River Basin. This onset signature of the rainy season is captured by the AGCM (Fig. 2.4f). In June, the monsoon rainfall continues to intensify and extend its coverage over the Indian and East Asian monsoon regions (Fig. 2.4b). At the same time the ITCZ migrates northward and merges with the SCS rain patch, forming a more continuous rain band over WNP. Concurrently, the Meiyu-Baiu front progresses northward, bringing prolonged rainfall to central-eastern China and Japan during their Meiyu and Baiu season, respectively. The above seasonal march of the monsoon rain features is also seen in the AGCM environment (Fig. 2.4g). In July, the Meiyu front continues to advance northward, affecting the North and Northeast China, and bringing the Changma season to Korea (Fig. 2.4c). The overall band-like rainfall pattern that spans progressively over South China, Taiwan, central China, Northeast China, Japan and Korean Peninsula from June to July is commonly referred as Meiyu-Changma-Baiu rainbelt. This active phase is characterized by a rainfall peak during the EA summer monsoon period. The passage of the rainbelt is then followed by a monsoon break in August (Fig. 2.4d). At the same time, the Indian monsoon gradually weakens and the ITCZ retreats southward. In September, the narrow rainbelt strengthens and migrates southward; this monsoon revival marks another distinct peak in the monsoon rainfall period in East Asia (Fig. 2.4e). Again, the above-mentioned temporal features including the active phase, break and revival of the EA summer monsoon is also reasonably reproduced by the AGCM (see Figs 2.4h, 2.4i and 2.4j). Similar to the biases over SCS to the Philippine Sea as reflected in the climatological MJJAS-mean

precipitation, monthly mean precipitation is slightly overestimated in BOB from June to August and is probably related to the overestimated westerly moisture flux there.

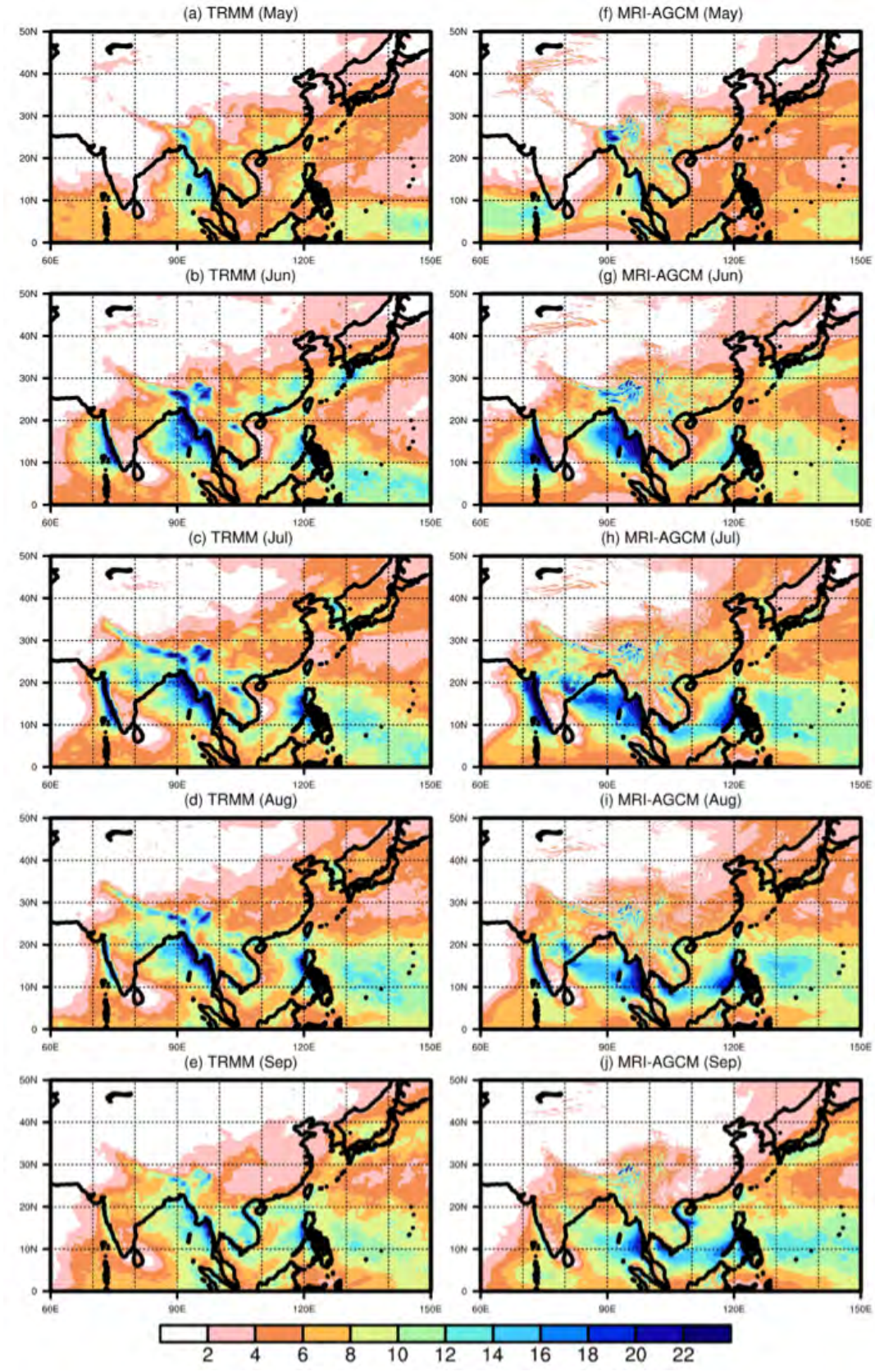

Fig. 2.4: Climatological monthly mean precipitation rate (units: mm day^{-1}) for (a, f) May, (b, g) June, (c, h) July, (d, i) August and (e, j) September, based on (a, b, c, d, e) for TRMM3B42v7 and (f, g, h, i, j) for MRI-AGCM3.2S data for the periods of 1998-2013 and 1979-2003, respectively.

In addition to assessing the AGCM seasonal mean circulation and precipitation, we have compared model simulated precipitation extremes with observations. For definitions of precipitation extremes, please refer to subsection 2.2.2. Fig. 2.5 compares the SDII based on AGCM simulations for the present climate, with values computed using TRMM and the APHRODITE datasets. From TRMM (and to a lesser extent APHRODITE), it is seen that the geographical distribution of SDII bears much similarity with the mean precipitation pattern in the Asian monsoon area. In general, locations with intense daily mean rainfall are collocated with those having large seasonal averages in summer. The MRI AGCM data reflect this phenomenon, and indicate extreme daily precipitation rates over the Western Ghats, the BOB region, central to southern SCS west of the Philippines and south of Japan. Compared with TRMM, the model simulated SDII is underestimated, with a negative bias of ~3.20 mm day^{-1} over SEA and EA monsoon region; the same comparison with APHRODITE, however, gives an overestimation of ~ 1.11 mm day^{-1}. In addition to domain-wide biases, we have also compared the AGCM-simulated PDFs of daily precipitation with observed PDFs based on TRMM and APHRODITE, particularly over Eastern China, Meiyu-Baiu rainband, Bay of Bengal and Central India, to see the regional distribution difference between the AGCM outputs and observed precipitation datasets (which will be later discussed in subsection 2.4).

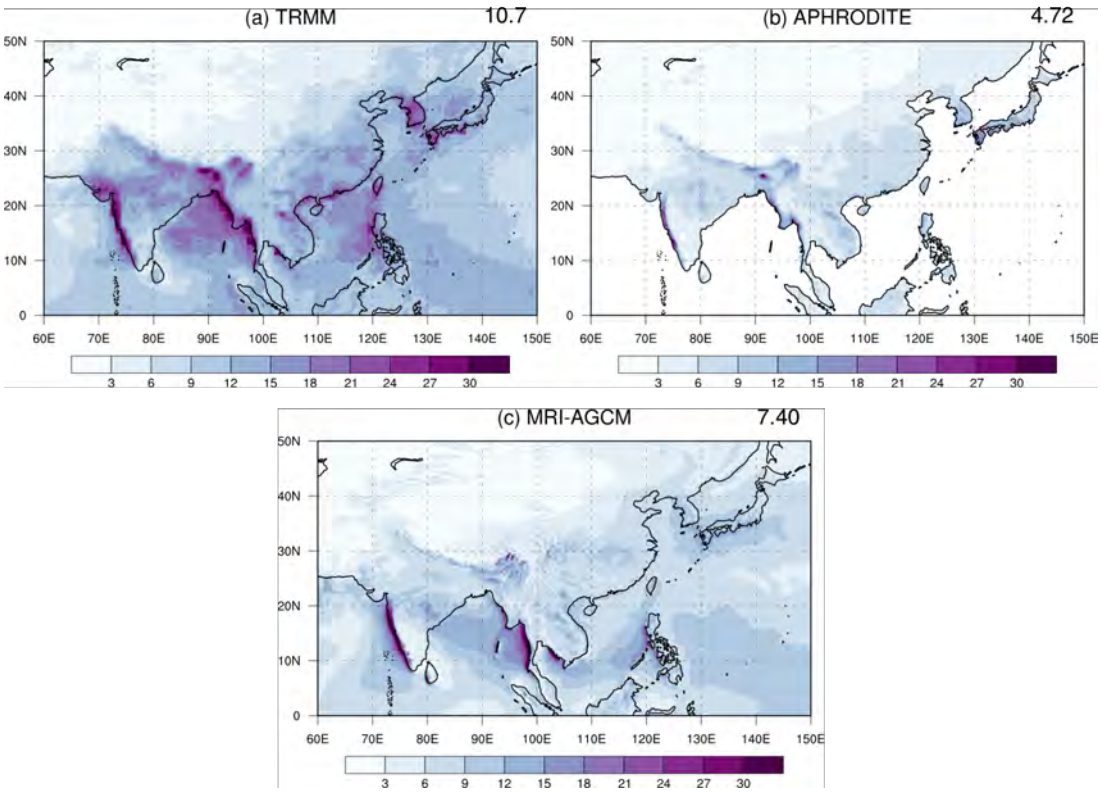

Fig. 2.5: SDII (units: mm day^{-1}) for MJJAS computed based on (a) TRMM3B42v7 for the 1998-2013 period, (b) APHRODITEv1101, and (c) MRI-AGCM3.2S for the 1979-2003 period. The SDII value averaged over the domain of 0-50°N, 60-150°E is shown in the upper right of each panel; for APHRODITEv1101, the average SDII is computed over land area only.

Finally, the pattern correlation between AGCM and observed (either TRMM- or APHRODITE- based) is about 0.8. Table 2.1 summarises the performance of the AGCM in simulating various measures of precipitation characteristics, by giving the pattern correlation coefficient, mean bias and root-mean-square error of the seasonal mean, Prec95p, and SDII when compared with observational datasets. It was found that the AGCM has good skills in capturing the observed climatological large-scale patterns of these metrics, with pattern correlation coefficients ranging from 0.76 to 0.87.

Table 2.1: Pattern correlation coefficient (PCC), mean bias, and root-mean-square error (RMSE) between daily precipitation statistics from MRI-AGCM and TRMM3B42v7 over the domain of 0-50N, 60-150E, and that between model and APHRODITEv1101 over land area in the same domain.

		Seasonal mean	SDII	Prec95p
	Definition	Precipitation total divided by number of days	Precipitation total divided by number of wet days	The 95th percentile of the set of the daily precipitation in wet days
TRMM3B42v7 (MJJAS, 1998-2013)	PCC	0.867	0.791	0.756
	Mean Bias	0.312 mm day^{-1}	-3.20 mm day^{-1}	-16.8 mm day^{-1}
	RMSE	2.03 mm day^{-1}	4.55 mm day^{-1}	21.5 mm day^{-1}
APHRODITEv1101 (MJJAS, 1979-2003)	PCC	0.840	0.817	0.805
	Mean Bias	0.726 mm day^{-1}	1.11 mm day^{-1}	1.72 mm day^{-1}
	RMSE	2.22 mm day^{-1}	2.51 mm day^{-1}	7.72 mm day^{-1}

As mentioned earlier, precipitation can be subsequently divided into two subsets, namely non-TC and TC-related rainfall. Fig. 2.6 shows the calculated SDII and Prec95p of non-TC and TC-related rainfall individually, based on AGCM simulations for the present climate. It is found that Fig. 2.6a resembles Fig. 2.5c very closely in terms of the geographical distribution and magnitude, thereby suggesting that non-TC rainfall (e.g. monsoon-induced rainfall) dominates in extreme precipitation over the Asian monsoon region. Small differences between Fig. 2.6a and Fig. 2.5c are found over areas with intense TC-related precipitation, such as northern SCS, coastal SEC and Baiu region (see Figs. 2.6c and 2.6d). The area-averaged SDII and Prec95p of AGCM-simulated non-TC-related (TC-related) rainfall are 6.94 and 22.4 (27.9 and 109) mm day^{-1} respectively.

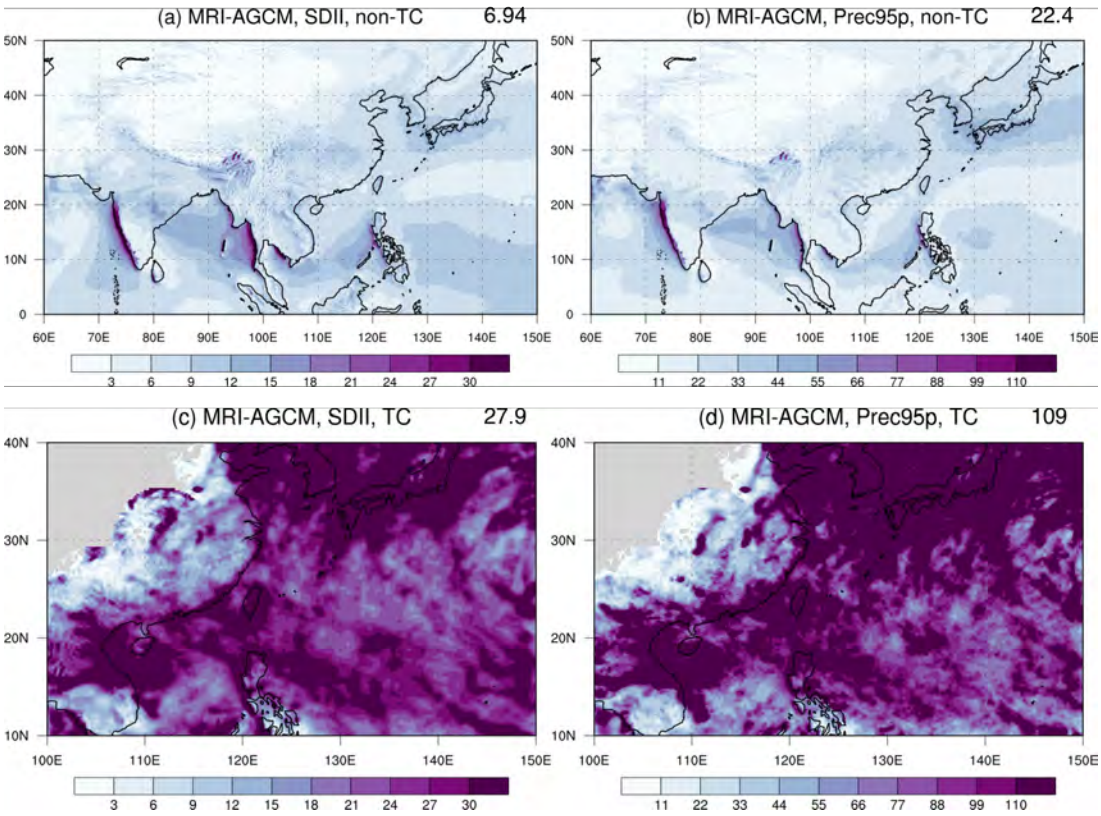

Fig. 2.6: (a) SDII and (b) Prec95p (units: mm day^{-1}) for non-TC related precipitation. The SDII and Prec95p values averaged over the domain of 0-50°N, 60-150°E is shown in the upper right of the panels. (c) and (d) as in (a) and (b), but for TC-related precipitation. The SDII and Prec95p values averaged over the domain of 10-40°N, 100-150°E is shown in the upper right of the panels. The SDII and Prec95p values are computed based on MRI-AGCM3.2S outputs over MJJAS for the 1979-2003 period.

Besides the time mean summer monsoon circulation, the ability of the AGCM in reproducing TC activity in boreal summer was also assessed. Fig. 2.7 shows the observed and model simulated TCF in the WNP basin in MJJAS. Observations indicate a region with the most frequent TC occurrences over and to the east of the Luzon Strait, with an average of 12.5 TCs found in WNP during the MJJAS season. It is obvious that the model can reproduce well both the TCF pattern and also the total storm number per season (11.9 TCs).

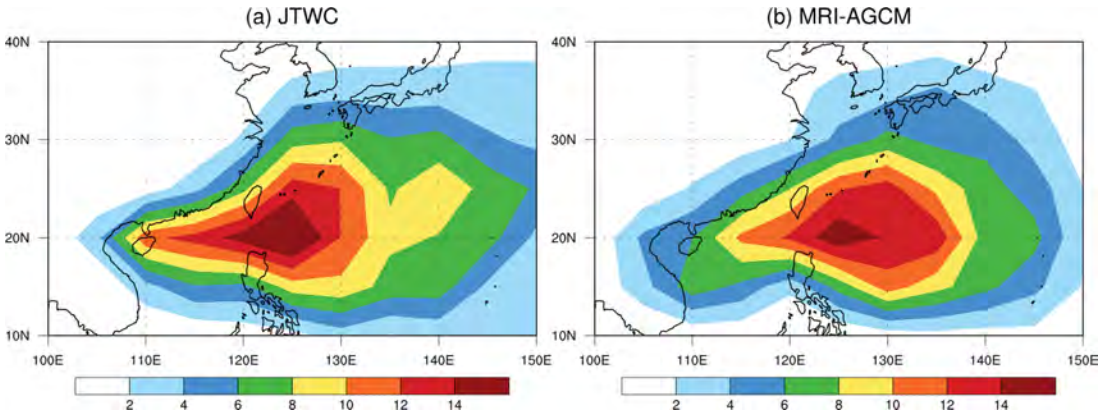

Fig. 2.7: TC occurrence frequency per season over each 5°×5° grid box in MJJAS based on (a) JTWC best track data, and (b) MRI-AGCM3.2S simulations. Statistics are computed for the 1979-2003 period.

Inspection of the observed TC genesis in WNP reveals two peaks located in SCS and east of the Philippines; the MRI AGCM also gives a very similar distribution, despite having underestimated the genesis frequency in the SCS region (Fig. 2.8). Overall, these assessments indicate that the model can give fairly realistic precipitation and TC behavior over the Asian monsoon and WNP regions. Next, we shall infer the impact of global warming on summertime precipitation extremes and TC-related rainfall based on future climate projections from this AGCM.

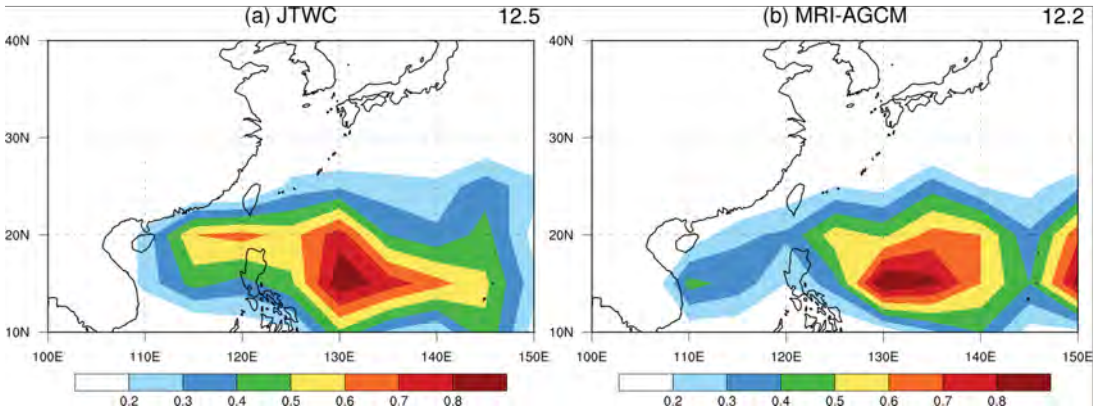

Fig. 2.8: As in Fig. 2.5 but for TC genesis frequency per season. The average number of TCs generated per year over the domain of 0-50°N, 60-150°E is shown in upper right corner of each figure.

2.4 Projected changes in precipitation intensity

Changes of the seasonal mean monsoon circulation are first examined, by comparing the model GW and PD simulations. Fig. 2.9 shows the GW minus PD MJJAS mean precipitation rates, 850hPa wind fields and surface air temperature using these AGCM runs. It can be seen that the seasonal mean rainfall will be enhanced over many locations in South and East Asia. Robust increase is found over BOB, the western Pacific ITCZ and some of the marginal sea areas, the Meiyu-Baiu rainbelt, Central India, the Eastern and also northeastern part of China. On the other hand, there are insolated regions where the seasonal mean rainfall will be reduced under global warming. In particular, an anomalously dry zone extending from coastal Vietnam to WNP can be inferred. Precipitation rates over the Western Ghats are also reduced. Overall, the mean rain rate averaged over 0-50°N, 60-150°E is projected to increase by 0.34 mm day^{-1} near the end of the 21st century. Changes in the low-level wind take the form of an anomalous anti-cyclone over WNP, while easterly anomalies are found over the tropical Indian Ocean and central-to-southern SCS. These suggest an overall slightly weakened Asian summer monsoon wind circulation (a weakened Indian monsoon wind circulation but a strengthened East Asian monsoon wind circulation) but heavier monsoon rainfall in the GW climate, consistent with many previous works (e.g. Vecchi and Soden 2007). For the surface air temperature, there is an increase over all locations in the Asian monsoon domain. The surface warming is stronger over land than over the ocean, and its signal tends to be greater over the Tibetan Plateau, and in high-latitude regions such as northern China and Mongolia. The model gives a 2.76 (2.98) K increase in the MJJAS mean surface (lower-tropospheric) air temperature over Asia by the end of the 21st century.

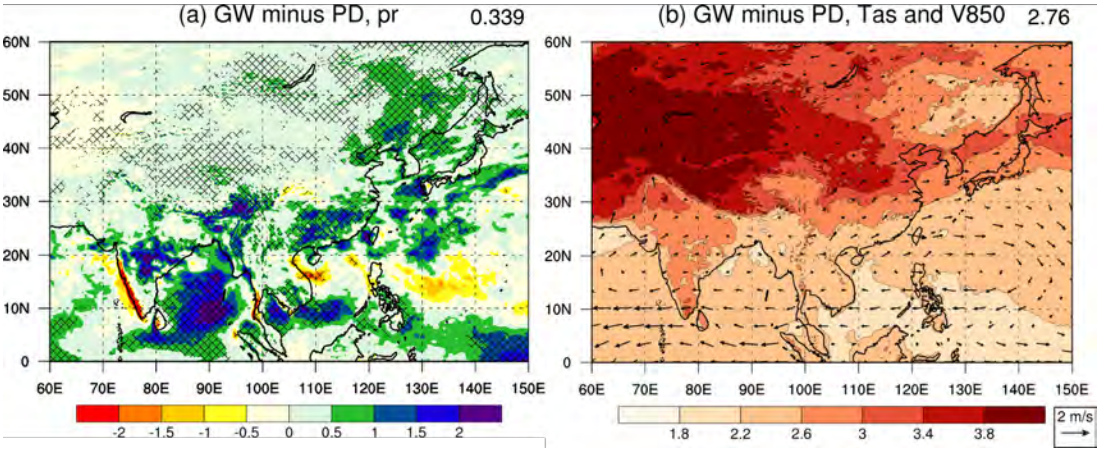

Fig. 2.9: Globally-warmed minus present-day (a) daily mean precipitation rate (units: mm day^{-1}), and (b) mean surface air temperature (units: K) averaged over MJJAS based on MRI-AGCM simulations. Their averaged values over the domain of 0-60°N, 60-150°E are shown in the upper right of each panel. Cross-hatches in (a) indicate that the differences are statistically significant at the 99% confidence level or above according to the two-sided Student's t test. Also shown in (b) are the MJJAS mean of globally-warmed minus present-day 850hPa winds (see scale arrow at bottom right).

We now focus on future changes in extreme precipitation given by the AGCM simulations. Figs. 2.10a and 2.10b show the computed SDII for the future GW climate and the GW minus PD values of the same index, respectively. It is noteworthy that SDII was found to increase significantly over locations where the mean rainfall also increases (see Fig. 2.9a). The Prec95p index also gives very similar changes in the extreme precipitation (see Fig. 2.10c). In particular, four regions with a coherent increase of both the mean and extreme precipitation can be identified, namely Eastern China (25-32N, 108-122E), Meiyu-Baiu rainband (30-35N, 125-145E), BOB (6-17N, 85-95E), and Central India (17-22N, 74-82E). We have also computed changes of the scale parameter, which is used for characterizing the gamma-fitted daily precipitation (see chapter 2.2). Fig. 2.10d gives the GW minus PD values of the scale parameter over locations where the gamma distribution can well represent the daily rainfall PDF. The goodness of fit was assessed by first carrying out the K-S test, for each summer from 1979 to 2003. The gamma distribution is then assumed to be valid if, at a

particular location, there is 80% (or more) of summer seasons during which the test reaches the 10% significance level. Out of these four abovementioned regions, two of them (Eastern China and BOB) indicate a positive change of the scale parameter. Overall, the above suggests a robust increase of both the seasonal mean and daily extremes of precipitation over these four sub-domains, due to the influence of global warming.

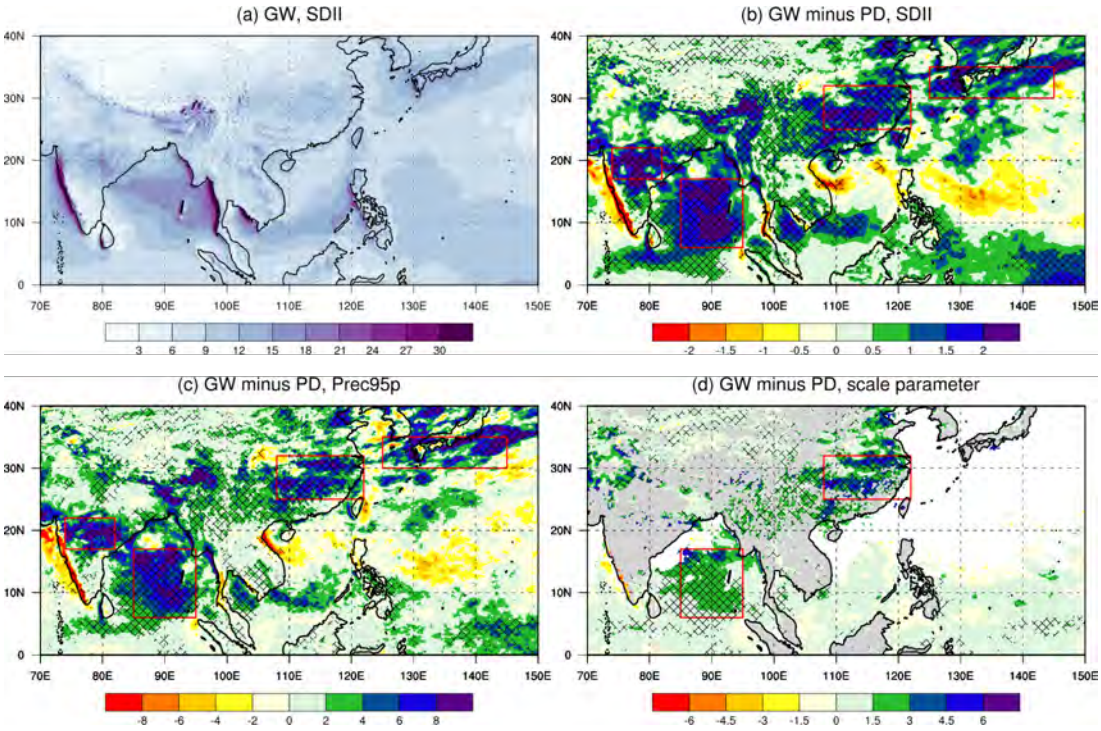

Fig. 2.10: (a) SDII during MJJAS for a future projected (globally-warmed) climate. Globally warmed-minus-present day (units: mm day^{-1}) of (b) SDII, (c) Prec95p and (d) scale parameter for fitted gamma distributions of daily precipitation rates in MJJAS, based on MRI-AGCM simulations. For scale parameter, only grids with present-day non-zero precipitation PDF showing goodness of fit of gamma distribution for at least 80% of seasons (using K-S test at significance level α = 0.1) are shown. Cross-hatches in (b), (c) and (d) indicate that the differences are statistically significant at the 99% confidence level or above according to the two-sided Student's t test.

The area-averaged values of these projected changes are listed in Table 2.2. Increase in both the seasonal mean precipitation and extremes are statistically

significant at the 99.9% level. Changes in the mean precipitation (Prec95p) averaged over Eastern China, Meiyu-Baiu rainband, BOB and Central India are 0.655 (4.22), 0.510 (3.56), 1.58 (5.77) and 1.24 (6.89) mm day^{-1}, respectively. Note that there is a discrepancy between the magnitudes of changes in the mean and extreme indices; this is in accordance with other studies, which show that the far tail of the daily precipitation PDF tends to extend more to higher values compared to the mean, causing the PDF to become more right-skewed under the influence of global warming (e.g. Allen and Ingram 2002).

Table 2.2: Globally-warmed minus present-day values of various statistics for the daily precipitation rate, averaged over different domains. Also shown are the same differences (in parentheses), divided by the corresponding regional changes in the MJJAS mean temperature. All projected changes of mean and precipitation extremes are statistically significant at the 99.9% level (Monte Carlo Permutation Test). Projected rate of extreme rainfall change per unit change of the lower-tropospheric temperature ranges from about 2.8 to 8.5 % K^{-1}.

	δMean (mm day^{-1})	δSDII (mm day^{-1})	δPrec95p (mm day^{-1})	δScale (mm day^{-1})
Eastern China (25-32N, 108-122E)	0.655 (4.15%/K)	1.34 (5.64%/K)	4.22 (5.35%/K)	2.81 (7.72%/K)
Meiyu-Baiu rainband (30-35N, 125-145E)	0.510 (2.76%/K)	0.934 (3.15%/K)	3.56 (2.84%/K)	N/A
Bay of Bengal (6-17N, 85-95E)	1.58 (5.36%/K)	1.76 (5.50%/K)	5.77 (6.42%/K)	2.05 (7.72%/K)
Central India (17-22N, 74-82E)	1.24 (6.12%/K)	2.02 (7.43%/K)	6.89 (8.47%/K)	N/A

From the four regions considered above, the PDFs of area-averaged daily precipitation rates generated from the AGCM are further examined. Fig. 2.11 gives the results computed based on the PD and GW experiments. Also shown are the observed PDFs based on TRMM (for all four regions) and APHRODITE (for Eastern

China and Central India only) datasets for comparison. Consistent with the results for SDII (see Fig. 2.5), TRMM (see red dashed curves) tends to give stronger daily extreme in comparison with the AGCM (blue curves). On the other hand, the model generated PDFs appear to be consistent with those estimated using the APHRODITE datasets over land (see brown dashed curves). Regarding the influence of global warming, it can be inferred that the probability of extreme rainfall is enhanced in the GW model environment, compared to the PD simulations. Such increment in the heavy precipitation likelihood is especially obvious for daily rain rates of about 30mm day^{-1} or more. In fact, the probability of 30-40mmday^{-1} events is projected to increase by about 10-40%, depending on the location of interest (see green curves in lower panel of each figure). Both the SDII and Precp95p values also increase in these regions (see vertical lines in Figs. 2.11a to 2.11d). Statistical tests further testify that that the PDFs from the GW and PD experiments are indeed different in all four regions, significant to the 99.9% level (based on the K-S test). It is also notable that the increase in Precp95p is larger than that in SDII, such that the PDF for daily precipitation rates is becoming more right-skewed over all four regions under the influence of global warming.

In addition to comparing the empirically determined PDFs, daily rain rates for Eastern China and BOB and their changes were also characterized using gamma distributions. This can be done by first estimating the regionally-averaged shape and scale parameters, in both PD and GW experiments. Lower panels of Figs. 2.11a and 2.11c show the ratio of PDFs from GW to those from PD runs, computed based on fitted gamma distributions with the corresponding shape and scale parameters determined over Eastern China and BOB areas (see black dashed lines). It is seen that the ratio of PDFs based on parameterized distributions agrees well with that computed

from the raw PDFs, at least up to the present-day 95th percentile values (around 30 mm day^{-1}) for both regions. Since the shape parameter only changes slightly (from 0.672 to 0.647, or a fractional change of -3.72% in Eastern China, and 1.30 to 1.24, i.e. a fractional change of -4.62%, in BOB), one may also assume that the shape parameter remains the same in the two AGCM experiments, to first approximation. Under such an assumption, the ratio of the PDF of GW to that of PD experiments can be approximated by:

$$\frac{f_{GW}}{f_{PD}} = \left(\frac{1}{c}\right)^{\alpha_{PD}} e^{\left(\frac{1}{\beta_{PD}}\right)\left(1-\frac{1}{c}\right)x} \tag{2.3}$$

where α_{PD} and β_{PD} are the present-day shape and scale parameters, and c is the scale parameter from GW divided by that from the PD experiment. It was found that β_{PD} over Eastern China (BOB) is 13.4 mm day^{-1} (10.1 mm day^{-1}), with an increase of 20.9% (20.8%) in the GW experiment. Using these estimates, we further examine whether it is valid to use the scale parameter alone to explain the changing PDF. By ignoring changes of the shape parameter (i.e. using Eq. 2.3), it can be seen that the fractional increase in extreme daily precipitation rates is overestimated (see pink dashed lines in lower panels of Figs. 2.11a and 2.11c). This is especially obvious in Eastern China, and less so in BOB region. Thus, for characterizing changes in moderate precipitation extremes, the shape parameter can be assumed to be constant (such that Eq. 2.3 is valid). For very extreme values (say greater than 99th percentile), however, the gamma distribution seems not capable in representing their changes due to global warming; it always tends to overestimate the increase of probability for extremely heavy rainfall (compare black dashed with green curves Figs. 2.11a and 2.11c).

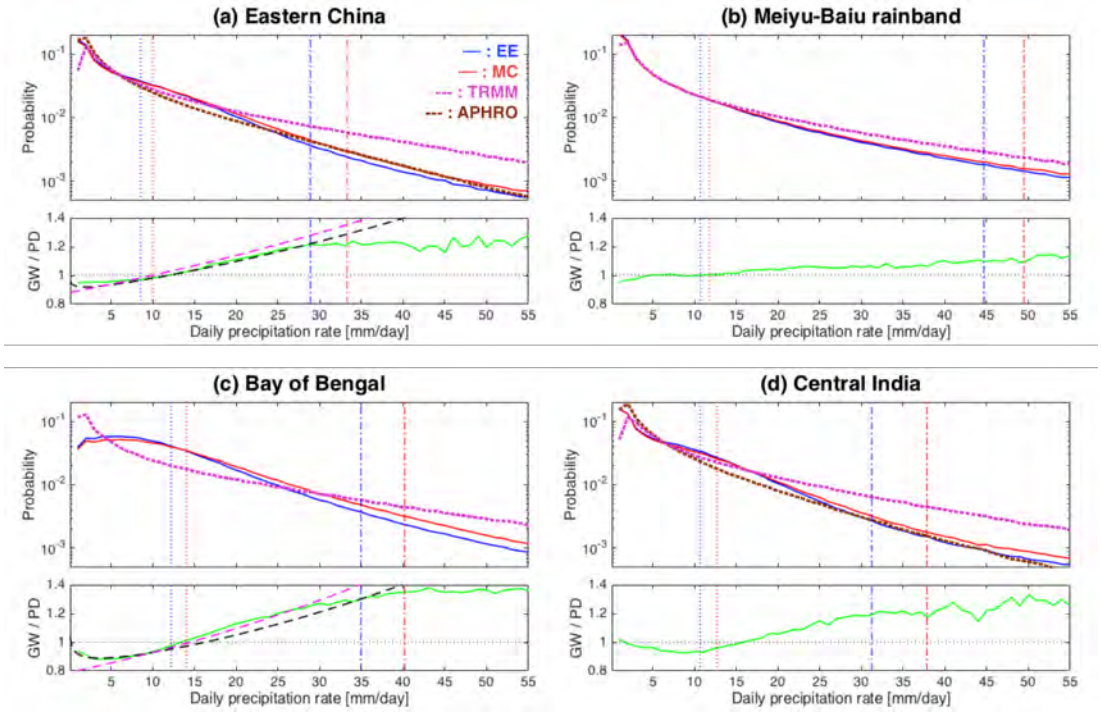

Fig. 2.11: Probability density function (PDF) for present-day (in solid blue) and globally-warmed (in solid red) daily precipitation rates, based on MRI-AGCM simulations from the region of (a) Eastern China (25-32N, 108-122E), (b) Meiyu-Baiu rainband (30-35N, 125-145E), (c) Bay of Bengal (6-17N, 85-95E) and (d) Central India (17-22N, 74-82E). The observed PDFs for present-day daily precipitation rates based on TRMM-3B42V7 (dotted pink) and APHRODITEv1101 (dotted brown) are included for Eastern China and Central India; for the Meiyu-Baiu rainband and Bay of Bengal regions, only those based on TRMM-3B42V7 are shown. Lower panel in each figure gives the globally-warmed PDF divided by the present-day PDF over each region (in solid green), with the fitted gamma distribution function in the globally-warmed future divided by that in present-day (in dashed black), and the same quantity estimated according to Eq. 2.3 (in dashed pink). The blue and red dotted (dot-dashed) vertical lines represent the present-day and globally-warmed SDII (Prec95p) respectively. See text for details.

It is also instructive to compute the rate of change of extreme precipitation per unit degree of warming, and to compare such a rate at different locations with that predicted by the CC relation (see Introduction). Here the projected lower-tropospheric warming was estimated by the GW minus PD seasonal mean temperature, averaged over the 500 to 1000hPa. Percentage changes of SDII and Precp95p divided by such temperature change were then computed at every grid point. The same quantity for the scale parameter is also included in Eastern China and BOB. The probability

distributions of their gird point values over the four regions with robust precipitation increase are given in Fig. 2.12. It was found that over Eastern China, BOB and Central India, changes in both the mean and extreme precipitation rates are in general agreement with the CC relation, i.e. the probability values generally peak around 7 % K^{-1} (see vertical dashed line in panels). It is also noteworthy that both the mean and extreme rain rates seem to behave in the same manner under the global warming influence. However, over the Meiyu-Baiu rainband region, the most likely change in precipitation rates was found to be about 3 % K^{-1} only. To reduce the uncertainty in estimating daily precipitation, we have also taken the spatial average of the changes of these extreme indices per unit temperature change (see Fischer et al. 2013); the resulting values range from about 3 to 8 % K^{-1} (Table 2.2). The area average of the projected change in daily mean precipitation rate per unit lower-tropospheric temperature change in the whole domain (0-60°N, 60-150°E) was found to be 3.05 % K^{-1}.

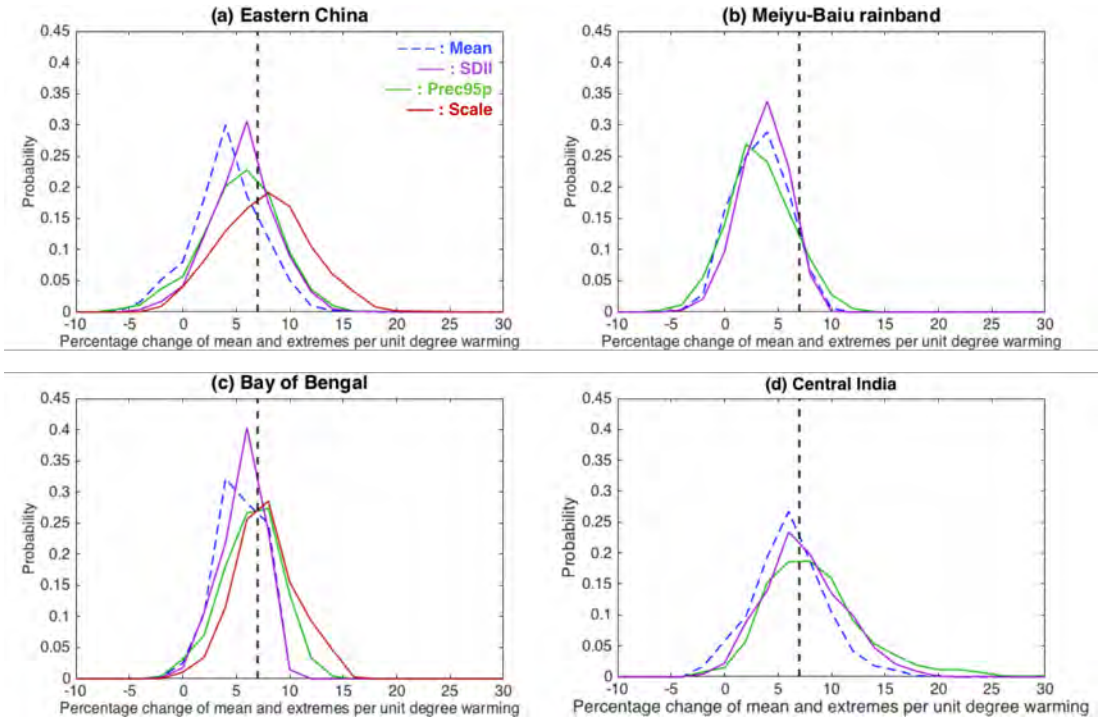

*Fig. 2.12: Probability distribution of changes in the time mean precipitation rates (*dotted blue line*), SDII (*purple*) and Prec95p (*green*) per unit degree of warming in the lower-to-mid troposphere in MJJAS, in the globally-warmed compared to the present-day simulations, over grid boxes within (a) Eastern China (25-32N, 108-122E), (b) Meiyu-Baiu rainband (30-35N, 125-145E), (c) Bay of Bengal (6-17N, 85-95E) and (d) Central India (17-22N, 74-82E). The probability distribution of changes in the scale parameter (*red*) for gamma-fitted daily precipitation rates, per unit degree of warming, is shown only for (a) Eastern China and (c) Bay of Bengal (6-17N, 85-95E). See text for details.*

2.5 Projected changes in tropical cyclone rainfall

In this subsection, the same sets of AGCM simulations were used to examine how climate change might influence TC precipitation over various East Asia locations. Figs. 2.13a and 2.13b show the TCF in the GW experiments, as well as the GW minus PD TCF values, respectively. It is clear that there is an overall reduction of TC activity over the SCS and WNP regions, under the influence of global warming. TCF east and northeast of the Philippines is significantly affected, with a decrease about of 5 to 6 TCs per season. TC occurrences are also strongly suppressed over northwestern SCS near Vietnam and in southern Japan. Inspection of the GW minus PD seasonal mean

circulation revealed anomalous sinking motion in the mid-troposphere and low-level anti-cyclonic flow over SCS and east of the Philippines (see Figs. 2.14a and 2.14c). Furthermore, in the vicinity of southern Japan, there is enhanced vertical wind shear (see Fig. 2.14b). The above circulation changes are consistent with suppressed TC activity over these regions. We have also computed TC composites of the mean sea-level pressure (MSLP) and TC-related precipitation, for TCs identified in the PD and GW experiments. Fig. 2.13c shows the azimuthally averaged results as a function of distance from the TC center, based on GW minus PD composites. The composite minimum SLP of a TC in the model is projected to decrease by ~ 85 Pa (~ 0.1%), while the rain rate will increase by up to 70 mm day^{-1} (~ 25% within 100 km) due to global warming; the latter is slightly larger than the fractional change in rain rate given by Knutson et al. (2015). In fact, the precipitable water over WNP is projected to increase in GW in comparison to the PD experiment (see Fig. 2.14d). Enhanced precipitation related to each TC is thus consistent with more moisture in the atmosphere under a warmer background climate.

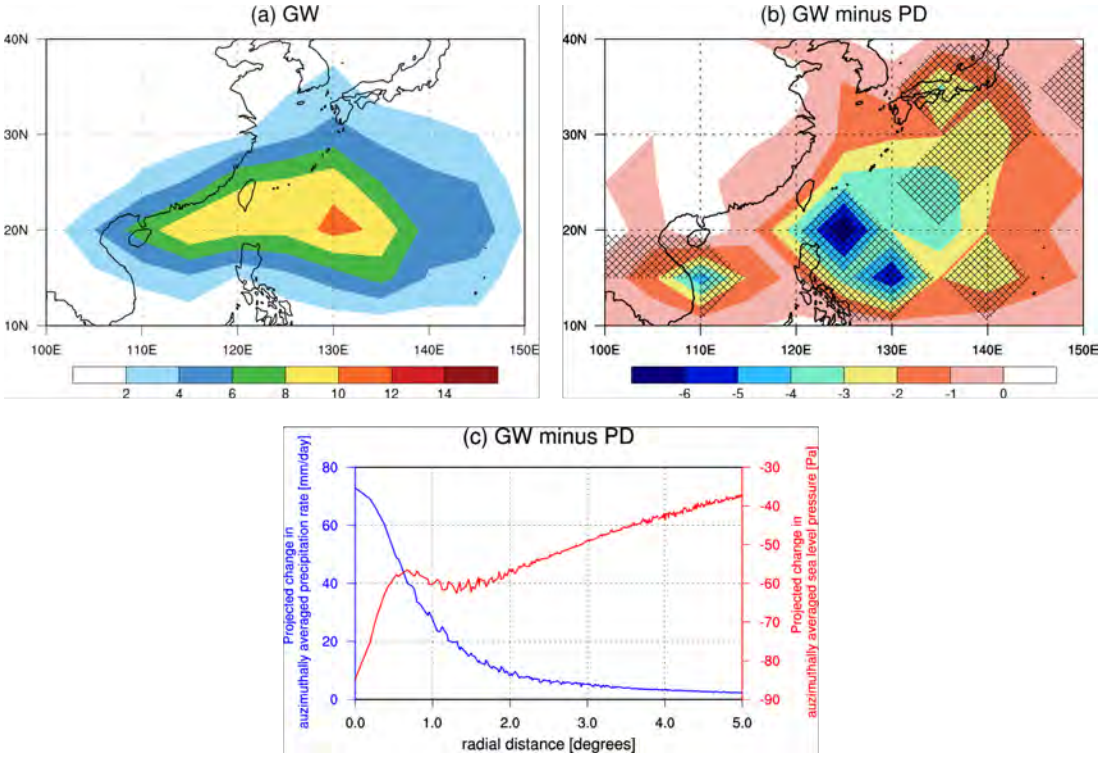

*Fig. 2.13: (a) As in Fig. 2.5(b) but for future (globally warmed) climate simulations. (b) Globally-warmed minus present-day TC occurrence frequency per season over each 5°×5° grid box in MJJAS. (c) Auzimuthally averaged precipitation rate (*blue, *in units of mm day*$^{-1}$*;) and MSLP (*red, *in units of Pa) as a function of distance from TC center, based on TC composites in the same season from MRI-AGCM simulations. Cross-hatches in (b) indicate that the differences are statistically significant at the 90% confidence level or above according to the two-sided Student's t test.*

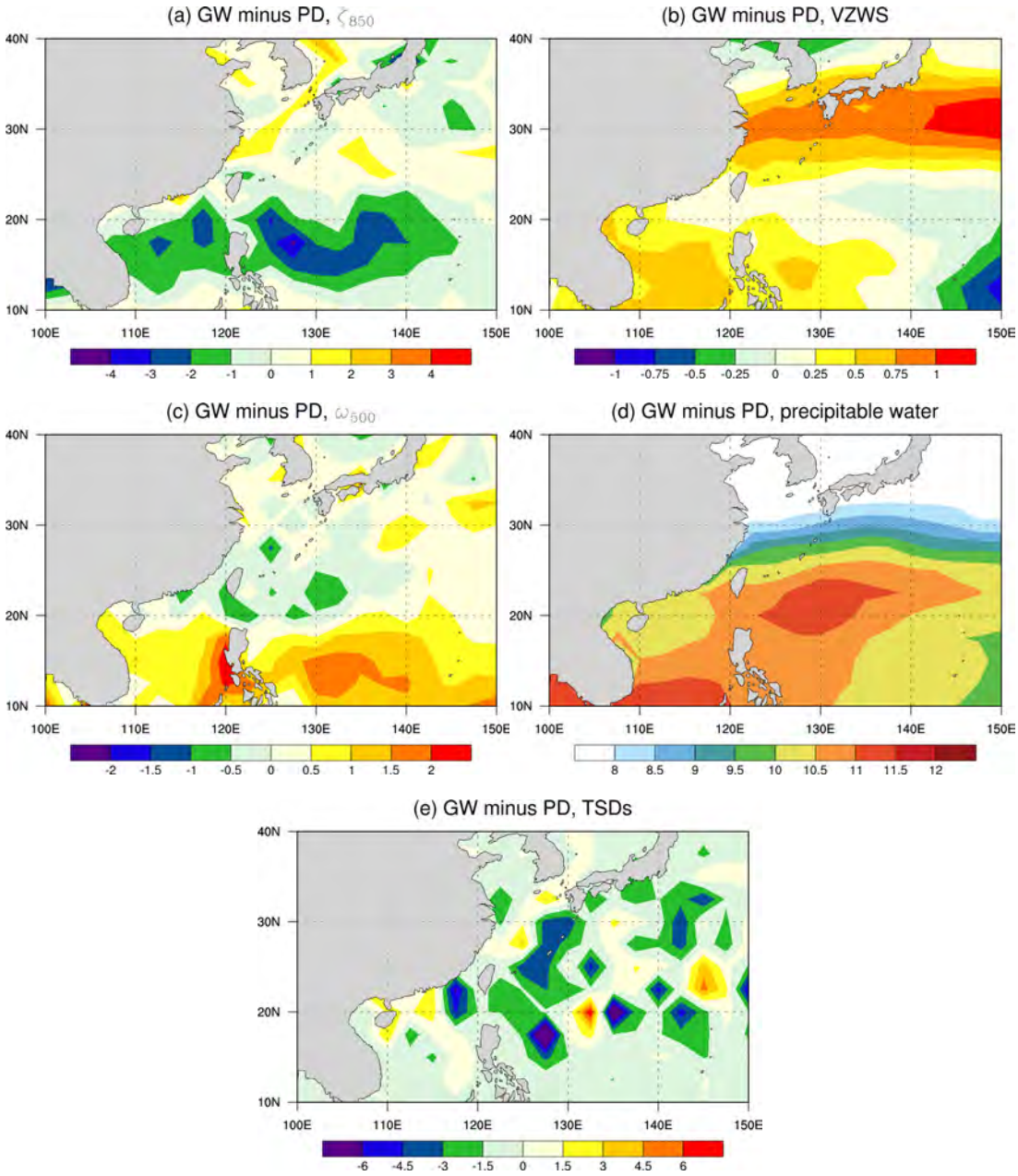

Fig. 2.14: Globally-warmed minus present-day (a) relative vorticity at 850hPa (unit: 10^{-6} s^{-1}), (b) vertical zonal wind shear (VZWS, zonal wind at 300hPa minus zonal wind at 850hPa; unit: m s^{-1}), (c) vertical pressure velocity at 500hPa (unit: 10^{-1} Pa s^{-1}), (d) precipitable water (PW; unit: kg m^{-2}), and (e) variance of tropical synoptic-scale (2-8-day) disturbances (TSDs; unit: 10^{-10} s^{-2}), interpolated on a 2.5°×2.5° grid in MJJAS.

With increased TC rain rate but at the same time fewer TC storm days in the future GW climate, a question thus arises: how does the magnitude and geographical distribution of accumulated TC-related rainfall change accordingly? Figs. 2.15a and 2.15b show the geographical distribution of TC-related accumulated rainfall from the

PD and GW simulations; also shown is the difference between values from these two runs (Fig. 2.15c). It can be seen that there are robust changes in the accumulated TC rainfall over Southeastern China (22-28N, 108-120E), Taiwan (21.5-25.5N, 120-122E), the Meiyu-Baiu rainband (30-35N, 125-145E), northwestern SCS (14-18N, 105-113E), and east of the Philippines (14-20N, 123-130E). Such GW minus PD differences can be further written as the contributions from two terms, one due to change of TC rain rate and the other due to change of TC storm days as follows:

$$\begin{aligned}\delta TCP &= R_{GW}N_{GW} - R_{PD}N_{PD} \\ &= \tfrac{N_{GW}+N_{PD}}{2}(R_{GW} - R_{PD}) + \tfrac{R_{GW}+R_{PD}}{2}(N_{GW} - N_{PD}) \\ &= \bar{N}\delta R + \bar{R}\delta N \end{aligned} \quad (2.4)$$

where R_{PD} and R_{GW} are the mean TC rain rates in mm day^{-1} in the PD and GW runs, respectively; N_{PD} (N_{GW}) denotes the mean TC storm days for the PD (GW) experiments. $\bar{N}$ and δN are the average and difference between N_{PD} and N_{GW} respectively; $\bar{R}$ and δR are defined similarly. These two components are calculated at every grid point and averaged over each geographical region. Their area averages as well as their sum total are presented in Fig. 2.15d. Despite the reduced numbers of storm days in Southeastern China and Taiwan, having more precipitation per TC leads to an increase of accumulated rainfall by 18.4 and 16.3 mm respectively. In contrast, the accumulated TC rainfall per season is projected to decrease by 25.5, 50.6 and 64.9 mm over the Meiyu-Baiu region, SCS and the east of the Philippines respectively; this is mainly due to the reduction of storm days in these locations.

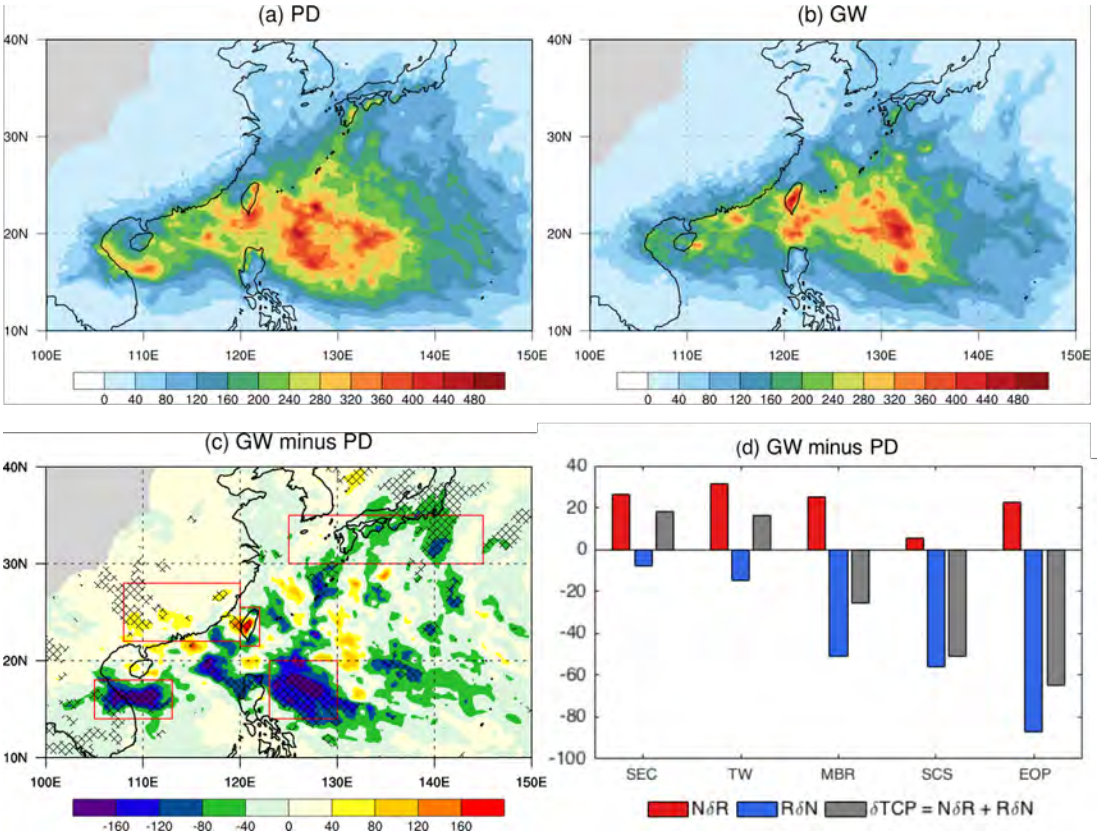

*Fig. 2.15: (a) Present-day, (b) Globally-warmed future accumulated TC rainfall per season in MJJAS based on MRI-AGCM simulations. (c) Difference between (b) and (a). (units: mm) (d) Globally-warmed minus present-day accumulated TC rainfall per MJJAS season due to change of TC intensity (*red*), due to change of TC storm days (*blue*) and their sum (*grey*) based on MRI-AGCM simulations, for Southeastern China (22-28N, 108-120E), Taiwan (21.5-25.5N, 120-122E), Meiyu-Baiu rainband (30-35N, 125-145E), South China Sea (14-18N, 105-113E), and east of the Philippines (14-20N, 123-130E). Cross-hatches in (c) indicate that the differences are statistically significant at the 90% confidence level or above according to the two-sided Student's t test.*

Finally, in order to assess the contribution of TCs to precipitation extremes, we have further stratified rainfall rates into five categories, namely those within 0.1-1 mm day^{-1}, 1-10 mm day^{-1}, 10-50 mm day^{-1}, 50-200 mm day^{-1} and more than 200 mm day^{-1}, and for TC and non-TC related events separately. Fig. 2.16 gives the GW minus PD number of TC and non-TC related rainfall events per season over Southeastern China, the Meiyu-Baiu and Taiwan regions. In Southeastern China, the likelihood of events under 10 mm day^{-1} are projected to decrease; for more intense precipitation

events with rain rates greater than 10 mm day^{-1}, their probability will increase under the global warming influence (see Fig. 2.16a). Based on the AGCM present-day simulations, the average non-TC (TC) rainfall frequency over SEC is 81.0 (3.04) days per season, and it will decrease by 0.80% (2.8%). For the Meiyu-Baiu region, again there is a similar increase (decrease) of the occurrence of more (less) intense precipitation events (see Fig. 2.16b). TC-related rainfall, on the other hand, is projected to decrease regardless of their intensity. This is consistent with the significant reduction of TC activity in this region (see again Fig 2.14). In fact, changes in TC rainfall appear to have substantial contribution to the overall precipitation statistics in this region. The computed changes in SDII and Prec95p based on non-TC rainfall events are 1.32 mm day^{-1} and 5.16 mm day^{-1} respectively, which are larger than those without removing the TC rainfall events (1.15 mm day^{-1} and 4.31 mm day^{-1} respectively). This implies that non-TC weather systems will lead to an exacerbation of the daily precipitation extremes, which are partially offset by a reduction in TC-related extremes. The AGCM-simulated number of non-TC (TC) rainfall events in Meiyu-Baiu region is 98.7 (4.28) days per season on average in the present climate, and it is expected to decrease by 0.28% (37%) in the future. For Taiwan, actually TCs are projected to contribute to the increase of both the seasonal mean precipitation rate (from 0.223 mm day^{-1} to 0.432 mm day^{-1}) and SDII (from 0.223 mm day^{-1} to 0.465 mm day^{-1}). Further inspection revealed that this is likely related to the enhanced occurrence of TC-related rainfall events with 200 mm day^{-1} or more in the GW compared to the PD simulations. For less intense TC rainfall events, their frequencies are projected to decrease (Fig. 2.16c). Overall, rainfall events more (less) 1 mm day^{-1} are expected to occur more (less) frequently. For Taiwan, the average number of non-TC (TC) rainfall events is 103 (8.30) days per season, based on the PD simulations.

The number of non-TC and TC related rainfall events are projected to increase by 2.3% and decrease by 18% respectively in the globally-warmed future.

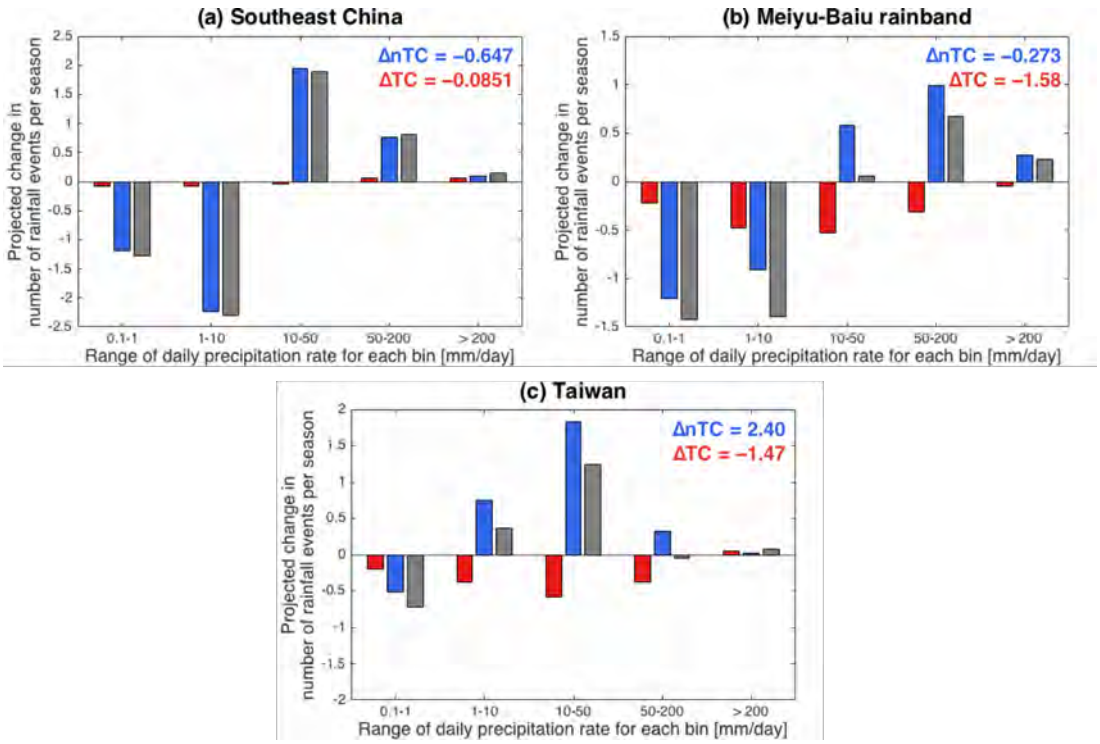

Fig. 2.16: Globally-warmed minus present-day TC (red), non-TC (blue) rainfall event number per season, as well as their sum total (grey), as a function of daily precipitation intensities, over (a) Southeastern China (22-28N, 108-120E), (b) Meiyu-Baiu rainband (30-35N, 125-145E), and (c) Taiwan (21.5-25.5N, 120-122E). The change in number of non-TC and TC related rainfall events is shown in upper right corner of each figure. See text for details.

2.6 Limitations and uncertainties

Firstly, despite very high resolution, the AGCM still cannot resolve TCs and it might truncate extremely intense TCs in both PD and GW simulations. Secondly, certain detection algorithm is needed to classify vortices as tropical storms in model simulations, and is not universal among TC impact studies. Thirdly, cold wake in the surface ocean after a tropical cyclone is ignored as the AGCM does not simulate interactions with the ocean (i.e. no ocean coupling).

Sources of uncertainties includes the uncertainty regarding the future scenarios for greenhouse gases emissions or concentrations. Regional forcing other than GHGs (e.g. land use change and urbanization) is not considered and there is limited aerosol varying forcing. Also, projected changes in TC activity are strongly dependent on projected changes in spatial pattern of tropical SST and indeed there are three clusters of patterns of SST changes in CMIP3 (also CMIP5) projections. However, note that the SST pattern prescribed in AGCM experiment is a product of a multi-model-ensemble projection, which sort of reduces systematic biases due to different configurations of GCMs. Besides, since only a single set of AGCM simulations is considered (i.e. no initial-condition-ensemble), errors arise due to the AGCM internal variability. At last, signal to noise ratio becomes smaller when it comes smaller regions (e.g. Taiwan). Recently, Huang et al. (2016) projected a reduction of TC-related rainfall over Taiwan. In their results, this is due to the southwestward extension of the WNP subtropical high which suppresses TCs in the vicinity of Taiwan. Apparently, more studies are needed to ascertain future characteristics of TCs, intense precipitation and other extremes, and for understanding their uncertainties by conducting and analysing various high-resolution model climate projections for the Asian monsoon area.

2.7 Summary

We have assessed the performance of the MRI AGCM version 3.2S in simulating extreme precipitation (including that induced by TCs) in boreal summer over the Asian monsoon region, and have examined how global warming might influence these extremes in the model environment. Overall, the AGCM performs well in capturing the seasonal mean as well as extreme precipitation patterns in Southeast and East Asia.

The model daily precipitation extremes tend to be underestimated when compared to TRMM; on the other hand, they appear to be reasonable, according to estimates based on APHRODITE data over land areas. By comparing the GW with PD experiments, the summertime mean rain rate is projected to increase over many locations in the Asian monsoon region. It is worth mentioning that when it comes to the impact of climate change on Asian monsoon, one should be careful about changes in monsoon circulation versus changes in monsoon rainfall. This is the case of an enhanced monsoon rainfall despite a weakened monsoon wind circulation (a weakened Indian monsoon wind but a strengthened East Asian monsoon wind) in the future climate projection. In particular, low-level westerlies will be reduced over the tropical Indian Ocean and SCS; at the same time, the strength of the low-level monsoon trough east of the Philippines is also projected to decrease under the influence of global warming.

Over the regions of Eastern China, the Meiyu-Baiu rainbelt, BOB, and central India there are robust increase in both the seasonal mean precipitation and extreme rainfall. Summertime mean daily (extreme) rain rates over these areas are projected to increase by about 0.5-1.6 (0.9-6.9) mm day^{-1}. Further inspection revealed that PDFs for daily precipitation in these regions from the GW runs are significantly different from their PD counterparts, with the greatest increase in probability found in the higher percentiles. We have also investigated the model precipitation characteristics in different Asia monsoon regions using the parametric gamma function. It was found that PDFs of daily rain rates over Eastern China and BOB can be well represented by the gamma distribution. Such parametric approach was then used to study how global warming might impact on precipitation behaviour in these two regions. There is robust increase of the scale parameter in the two regions (20.9% and 20.8% in Eastern China and BOB, respectively), leading to enhanced probability precipitation rates in the

higher percentiles. Slight reductions of the shape parameters were also found (-3.72% and -4.62% in Eastern China and BOB respectively). It appears that the gamma fitting provides a concise way to describe the change of daily rain rates, accurate up to about the 95th percentile. For even more extreme precipitation events, however, the gamma distribution tends to overestimate the change of their occurrence frequency compared to that computed based on the actual PDFs.

We have also compared the increment of extreme rainfall due to global warming with that given by the CC relation. Based on the model-projected increase of about 2.98 K in the MJJAS mean lower-tropospheric air temperature, the change of precipitation extremes per unit change of the lower-tropospheric temperature were computed. In three out of four aforementioned domains with robust increase of extreme rain rates, namely Eastern China, BOB and central India, the results are about 5.5 to 8 % K^{-1}, which is roughly consistent with the CC relation. The only exception to this scaling rule is found over south of Japan in the Baiu region, where the change is only about 3% K^{-1}. In fact, we have checked that the model precipitable water increases by about 6 to 7% K^{-1} in the same region (see Fig. 2.17). This suggests that the relatively modest increase of extreme rain rates is not due to limitations in the amount of precipitable water; instead, dynamic changes might play an important role in this region (see, e.g., Emori and Brown 2005). Further study is needed to unveil what dynamical factors might be responsible for the sub-CC scaling in this domain.

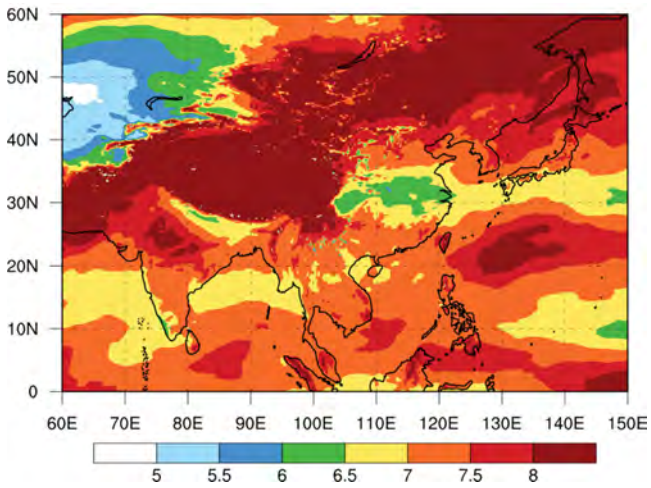

Fig. 2.17: Globally-warmed minus present-day precipitable water (PW) per unit degree warming of low tropospheric warming (unit: % K^{-1}).

We have also investigated how TC-related rainfall might be influenced by global warming. There is an overall reduction of TC numbers over the WNP basin, when comparing GW with PD experiments. This is likely due to the reduced low-level relative vorticity over a broad area in this domain; also, the variance of high-frequent vorticity fluctuations is reduced east of the Philippines and part of SCS (see Fig. 2.14e). On the other hand, TC-related rain rate is projected to increase, in conjunction with TCs becoming more intense in a warmer climate. Overall, the combined effect of these two competing factors leads to more (less) TC rainfall over southeastern China/northern SCS and Taiwan (east of the Philippines and southern Japan). Further analyses indicated that indeed the reduced TC rainfall east of the Philippines and southern Japan can be attributed to the suppression of TC activity there; the increased TC rainfall over part of Southeastern China and Taiwan is due to more intense TC rain rate. Finally, by analyzing TC and non-TC related rainfall data, it was found that the enhanced daily precipitation extremes cover many locations can be mainly attributed to non-TC weather systems. In Southeastern China, both TC and non-TC related rainfall events contribute to the increase of extremes, with the latter weather type being

the main contributor. For the Meiyu-Baiu rainband, there is also an increase of the frequency of the most intense precipitation; this is again due to non-TC rainfall, while TCs are expected to partially offset such an increase. The notable exception is Taiwan, where heavy TC-related rainfall events (with daily accumulated rainfall exceeding 200 mm day^{-1}) play a role to the increase of both the seasonal mean precipitation rate and SDII; however, changes in the extremes are projected to be insignificant in an overall sense.

Chapter 3

Diurnal Cycle of Precipitation over Southeast Asia

3.1 Background

Latent heat over Southeast Asia is an important driver of both the Hadley and Walker circulations. Variations in convective activity and precipitation (including sub-daily variations) in this region are particularly important in shaping the global climate. Therefore, many researchers have focused on DC over this region such as Indochina peninsula (e.g. Yin et al. 2009; Takahashi et al. 2010; Huang and Chan 2012; Huang and Chen 2015) and Indonesian Maritime Continent (e.g. Wu et al. 2003; Mori et al. 2004; Ichikawa and Yasunari 2006; Zhou and Wang 2006; Ichikawa and Yasunari 2008).

It is widely recognised that DC has an out-of-phase difference between precipitation peak hours over land and over sea, due to a fundamental land-sea contrast in their atmospheric responses to radiative forcing. However, this idealized picture is complicated by various physical processes such as land-sea and mountain-valley breezes (e.g. Yang and Slingo 2001; Zhou and Wang 2006), diurnal gravity waves (e.g. Shige and Satomura 2000; Mapes et al. 2003), modulation associated with intraseasonal variability (e.g. Ichikawa and Yasunari 2006; Ichikawa and Yasunari 2008), interaction between local and large-scale circulations (e.g. Yin et al. 2009; Huang and Chen 2015) and tidal variations in atmospheric pressure (e.g. Dai 2001), based on either ground-based, satellite measurements or numerical simulations.

Besides observational studies, global climate models (GCMs; e.g. (Dai and Trenberth 2004; Hara et al. 2009; Ploshay and Lau 2010; Ichikawa et al. 2012), regional climate models (RCMs; Saito et al. 2001; Evans and Westra 2012) or even convection-resolving models (CRMs; e.g. Ruppert 2016) are also used to investigate

regional characteristics and mechanisms of DC. It is found that GCMs and RCMs tend to produce a DC precipitation peak that is too early in the day, mainly because the cumulus parameterization schemes response as soon as instability arises. Thus, CRMs come into play by resolving cloud processes and allowing a gradual development of convection, and they are found to capture the phase of DC well. However, due to small model domain and very high resolution, CRMs cannot simulate large-scale circulations and they are relatively computational expensive. Indeed, GCMs and RCMs are still used to date and consequently cumulus parameterization is still used in numerical simulations of SEA circulation. A good simulation of DC is necessary for models to reproduce the observed climate, especially over the tropics. Improper representation of DC may affect modes of climate variability at longer timescales (e.g. Masson et al. 2012; Ruppert 2016). For example, using an idealized CRM, Ruppert (2016) shows that DC accelerates the evolution of deep convection by amplifying the daily-mean cumulus heating and forcing of large-scale circulations through nonlinear rectification.

The International Centre for Theoretical Physics (ICTP) Regional Climate Model version 4 (RegCM4) is a RCM that is popular among climate researchers (e.g. the Coordinated Regional Downscaling Experiment (CORDEX) project). There are limited studies on the performance of RegCM4 in simulating diurnal rainfall, although da Rocha et al. 2009 and Huang et al. 2013 examined DC in earlier versions of RegCM. As compared to its previous versions, RegCM4 is updated with two major changes, namely a new option of land surface scheme and a “mixed convection scheme” (which will be discussed in subsection 3.2). Although Diro et al. (2012) have investigated DC simulations in RegCM4, their domain is Central America and they mainly study the sensitivity of DC to the new land surface scheme, but not the mixed

convection scheme. Therefore, in this chapter, we are motivated to examine the sensitivity of precipitation simulations over the CORDEX-Southeast Asia (SEA) domain to the cumulus convection scheme used in RegCM4, with a primary focus on DC in the region. The advantages of these experiments are to allow users to examine the sensitivity of simulated precipitation statistics to cumulus convection schemes within the framework of RegCM4, to recognize the biases of individual schemes, and finally to optimize the model performance; however, the results might depend on choices of domain, configuration of the control experiment or even model framework (e.g. model version), which is one limitation of these sensitivity experiments.

3.2 Model experiments and methodology

3.2.1 Model configuration and experimental setup

The RCM used in this chapter is the regional climate model RegCM version 4.4 (RegCM4) from ICTP. RegCM4 has a hydrostatic dynamical core, with an Arakawa B-staggering horizontal grid and a terrain-following sigma vertical coordinate (Grell et al. 1994). The model physics includes grid-scale cloud and precipitation processes, subgrid-scale convection, radiative transfer, turbulence mixing, land and ocean surface processes. A more detailed model description is given by Giorgi et al. 2012.

Compared to its previous versions, RegCM4 has been updated with improved model code and new physical parameterizations. It is noticed that the performance of the cumulus convection schemes show regional dependence, particularly over land versus ocean areas. For example, the Emanuel scheme (Emanuel 1991; Emanuel and Živković-Rothman 1999) tends to produce excessive precipitation over land areas; whereas the Grell scheme (Grell 1993) tends to produce weak precipitation over tropical oceans (Giorgi et al. 2012). (For a more detailed discussion on the

performance of the Emanuel and Grell schemes, refer to section 1.2). These lead to the development of an option in which users can run different convection schemes over land and over ocean; this is referred to as the “mixed convection scheme”. The configuration of using the Grell scheme over land and the Emanuel scheme over ocean provides the best precipitation statistics over most CORDEX domains, particularly over tropical regions (Giorgi et al. 2012).

Another important update is the addition of the Community Land Model (CLM; Oleson et al. 2008) for representing land surface processes. Compared to the other available land surface scheme BATS (Dickinson et al. 1993), CLM generally tends to inhibit precipitation over land due to its reduced soil moisture availability in the soil-precipitation feedback (Steiner et al. 2009). In addition, when using CLM, the Emanuel scheme (everywhere) outperforms other cumulus convection schemes in simulating temperature and precipitation in both summer and winter seasons over China (Gao et al. 2016). Among different combinations of cumulus, land, and ocean surface schemes, the combination of Emanuel, CLM and Zeng2 (for parameterizing ocean surface processes; Zeng et al. 1998) gives the best overall results in summertime rainfall and circulations over East-to-southeast Asia and the western north Pacific (Li et al. 2016).

It is also known that the Emanuel scheme overestimates convective precipitation in the tropical oceanic region with high SST (i.e. rich low-level moisture and high CAPE) by ignoring unfavorable large-scale atmospheric environment (Chow et al. 2006). For example, since SST of South China Sea (SCS) is relatively high during summer, the Emanuel scheme tends to produce excessive convective rainfall there, which is usually suppressed by the subtropical high over WNP. Therefore, convection suppression criteria such as relative humidity criterion (RHC), which is

based on the average relative humidity from cloud base to cloud top, have been applied to improve the performance over the Asian monsoon region (Chow et al. 2006; Zou and Zhou 2013). Relative-humidity-based suppression is found to allow effective accumulation of low-level moisture, thereby improving representation of deep convection in model simulations (e.g. Ichikawa et al. 2012). By conducting several test runs, we find that the threshold value of RHC = 0.73 (as suggested in Zou et al. 2014) is suitable for reducing the bias over SCS without impairing the Asian monsoon circulations. A newly-implemented prognostic DCSST scheme of Zeng and Beljaars 2005, which calculates the diurnal variations of the ocean skin temperature based on energy budget calculations, has also been tested and was found to be insignificant in improving the simulation of diurnal precipitation. This is consistent with the study of Diro et al. (2014) , in which the impact of DCSST scheme on DC simulations in RegCM4 over Central America was found to be relatively small.

Based on the aforementioned findings, results of two sensitivity tests are presented and discussed explicitly in this chapter. Using CLM4.5 (Oleson et al. 2010) and Zeng2 as the land and ocean surface schemes respectively, a modified Emanuel scheme (with RHC = 0.73) is used everywhere as cumulus convection scheme in the first experiment; whereas the second experiment employs a mixed convection scheme of the modified Emanuel scheme over ocean and Grell scheme (with AS-type closure) over land. The two sensitivity experiments are hereafter referred to as “EE” and “MC” respectively (“EE” and “MC” are the abbreviations for “Emanuel scheme everywhere” and “mixed convection schemes”). Other physical parameterizations adopted in the experiments include a modified radiative transfer scheme of the National Center for Atmospheric Research (NCAR) Community Climate Model version 3 (CCM3; Kiehl et al. 1996), a modified non-local planetary boundary layer

scheme of Holtslag et al. (1990) , and a resolved scale precipitation scheme based on SUBEX of Pal et al. (2000) .

For the experimental design, the simulation domain is set to the CORDEX Southeast Asia (SEA) domain (i.e. 15°S-27°N, 90-147°E), with a lateral buffer zone of 12 grid points with exponential relaxation. The model is run at a horizontal resolution of 50 km and a vertical configuration of 18 sigma levels, with the model top at 10 hPa. The initial, lateral boundary conditions and the SSTs are derived from the 6hourly, 1.5°×1.5° European Centre for medium-range weather forecast (ECMWF) ERA-Interim reanalysis data (Dee et al. 2011). The ERA-Interim driven runs are integrated continuously for 11 years (from 0000UTC on 1st Jan 2000 to 2100UTC on 31st Dec 2010) and model outputs are saved every 3 hour. The first year serves as model spin-up and therefore is excluded from the analysis. Table 3.1 summarises the model configuration and experimental settings for the sensitivity runs. To evaluate the model performance in reproducing the climatological annual, seasonal and sub-daily precipitation statistics, 3-hourly precipitation dataset TRMM3B42v7 is again used for the study period of 2001-2000. Also, where appropriate, meteorological variables such as winds, temperature and geopotential height from the ERA-Interim reanalysis data are also used for model validation.

Table 3.1: Model configuration and experimental settings used.

Contents	Description
Domain	15S-27N, 90-147E
Horizontal resolution	50 km
Vertical layers (Top)	18 (10 hPa)
Radiation	NCAR CCM3
Planetary boundary layer	Holtslag
Cumulus convection	(1) Modified Emanuel (RHC=0.73) everywhere (2) Modified Emanuel (RHC=0.73) over ocean and Grell with Arakawa Schubert type closure over land
Grid-scale precipitation	Subgrid explicit moisture scheme (SUBEX)
Land surface	NCAR CLM4.5
Ocean surface fluxes	Zeng2
Simulation period	Jan 2000- Dec 2010 (1st year for spin-up)

3.2.2 Methodology

To analyze the sub-daily variations of precipitation, we followed the EOF analysis suggested by Kikuchi and Wang (2008), except without reducing the horizontal resolution in EOF calculation. The steps are as follows: 1) The mean 24-hour cycle (i.e. 0000, 0300, …, 1800 and 2100 UTC, in total 8 time-steps) of precipitation are computed for every grid point; 2) At each grid point, the 24-hour time-series are converted from the Coordinated Universal Time (UTC) to Local Time (LT) based on its longitude; 3) The precipitation rates at given LT (i.e. 0000, 0300, …, 1800 and 2100 LT) are computed by Fourier interpolation; 4) Then, the mean 24-hour cycles of precipitation anomalies (δpr) of all grid points within the study domain are subjected to a EOF analysis; 5) Last, to facilitate comparison between model outputs and observation, the resulting EOF patterns are standardized by their respective spatial standard deviations over the whole domain. The corresponding PC time series is then multiplied by the spatial standard deviation accordingly such that the product of the standardized EOF patterns and the new PC time series remains the same as the sub-

daily variations. As a complementary method in our study, a Fourier analysis according to Ploshay and Lau (2010) was also performed. In fact, it agrees with the EOF results well so only those results based on EOF analysis are given.

Similarly, for any meteorological variable $X(t)$, its mean 24-hour evolution can be decomposed into:

$$X(t) = \bar{X} + \delta X(t) \tag{3.1}$$

where $\bar{X}$ represents a mean state over time, $\delta X(t)$ represents a time-dependent anomaly term, and t is 0000, 0300, …, 1800 or 2100 LT. Hereafter, $\bar{X}$ and δX denote the time-mean state and the time-varying anomaly of any given variable X respectively.

Fig. 3.1 shows the study domain, model topography, and four sub-regions (*dashed boxes*) for which the annual cycle of precipitation is analyzed, namely western Indochina (WIC; 15°-25°N, 92-98°E), southeastern China (SEC; 20°-25°N, 108-120°E), Sumatra (6°S-6°N, 95-107°E), and Borneo (4°S-7°N, 109-119°E). Also, to examine their spatio-temporal characteristics of diurnal precipitation explicitly, time-distance cross diagrams of δpr are generated along the *red dashed* arrow, averaged in the four sub-regions (*red boxes*). The direction of the arrow is chosen to be eastward (such that a more positive x in the cross diagrams indicates further to the east), and to be perpendicular to the direction of local coastline geometry or mountain orientation. The seasonal mean and diurnal precipitation are analyzed for four seasons, with primary focus on summer (JJA).

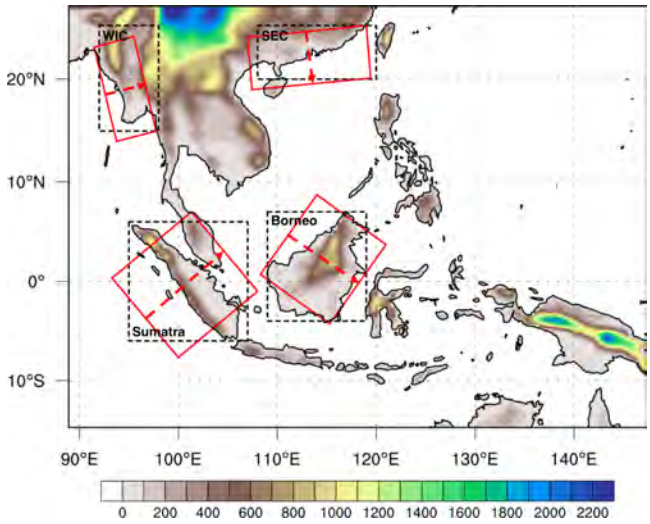

Fig. 3.1: Model domain, topography (shading; units: m). The dashed boxes show the eight sub-regions for which the annual cycle of precipitation is analyzed, namely western Indochina (WIC; 15°-25°N, 92-98°E), southeastern China (SEC; 20°-25°N, 108-120°E), Sumatra (6°S-6°N, 95-107°E), and Borneo (4°S-7°N, 109-119°E). The four red boxes denote the calculation domains for the time-distance cross diagrams in Figs 7, 8, 9, 10 and 11. See text for details.

3.3 Evaluation on simulated seasonal mean and annual cycle

3.3.1 Seasonal mean precipitation, winds and temperature

Before examining the performance in reproducing diurnal precipitation, we first begin by assessing the capability of the two model settings in capturing the summertime low-level circulation and precipitation over Southeast Asia. Figs 3.2a, 3.2b and 3.2c present the simulated and observed JJA mean precipitation in this region. Both simulations can reasonably capture the spatial distribution of the characteristic rainfall features, including the rainfall pattern over WIC, that over SEC, and the monsoon trough rainband spanning from SCS to east of the Philippines. However, they both over(under)-estimate the summer-time rainfall amount over the SCS and east of the Philippines (offshore areas of WIC and the equatorial western North Pacific). On the other hand, they show substantial differences in terms of their biases over different geographical regions. It can be seen that MC improves summer-time rainfall

simulations over SCS and east of the Philippines by reducing the overestimation there, compared to EE simulations. On the other hand, MC under(over)-estimates rainfall over land in SEC (western coastlines of Indochina and the Philippines). Similar bias patterns over this region are also reported in previous studies based on earlier versions of this model (e.g. Im et al. 2008; Zou et al. 2014), and also for the present version (e.g. Oh et al. 2014). Li et al. (2016) suggest rainfall overestimation over SCS and east of the Philippines are related to the positive latent heat flux biases in the vicinity. In our study, MC tends to have a lower near-surface specific humidity around eastern Indochina and northern SCS, compared to EE. This might lead to reduced latent heat flux biases, thereby causing reductions in rainfall biases in these locations. Such reduction in rainfall in turn leads to negative diabatic heating anomalies over these two regions (as reflected by the cold biases in Figs. 3.2d and 3.2e). Two low-level anticyclonic anomalies, which can be interpreted as Rossby wave response to diabatic heating, are formed to the west of the suppressed heating. This in turn leads to northeasterly wind branches related to the anticyclonic flow, which weakens the southwesterly monsoon wind. Therefore, precipitation reductions are found over these two regions, while that over the western coastlines of Indochina and the Philippines is enhanced. Also shown in Figs. 3.2a, 3.2b and 3.2c are the corresponding JJA mean wind fields at 850 hPa from two sets of runs and the ERA-Interim reanalysis. Compaerd to the reanalysis, both runs can reasonably capture the low-level wind branches that are associated with the East Asian, WNP monsoon systems and subtropical high during the summer. However, they show easterly anomalies over the southern SCS, Borneo and the equatorial WNP, which lead to an enhanced low-level wind convergence over SCS, with EE simulation showing a more pronounced convergence as compared to the reanalysis (figure not shown).

Figs. 3.2d, 3.2e and 3.2f compare the simulated JJA mean 850 hPa air temperature with the same field from the reanalysis. Both simulations can capture the latitudinal variations as well as the distinct peak over the Yungui Plateau. However, cold biases are found over the southern Indochina, northern SCS and northern Philippines, with MC simulations giving more negative biases over these regions. Although with reduced magnitude, these much colder biases in MC relative to EE simulations are persistent in other seasons, in accordance with other studies (Im et al. 2008; Gao et al. 2016). These colder biases are probably associated with the reductions in diabatic heating in MC compared to EE simulations, as discussed previously.

The pattern correlation between JJA mean precipitation from EE (MC) simulation and TRMM data is 0.584 (0.595). Table 3.2 summarises the performance of EE and MC in simulating precipitation in different seasons, by giving the pattern correlation coefficient, mean bias and root-mean-square error when compared with TRMM. It was found that both EE and MC have fair skills in capturing the observed geographical distribution of precipitation, with pattern correlation coefficients ranging from 0.47 to 0.71 in different seasons. For both EE and MC, PCC is lower in MAM and JJA than SON and DJF (which is primarily due to the overestimated rainfall amount in SCS), although RMSE is roughly the same in all seasons.

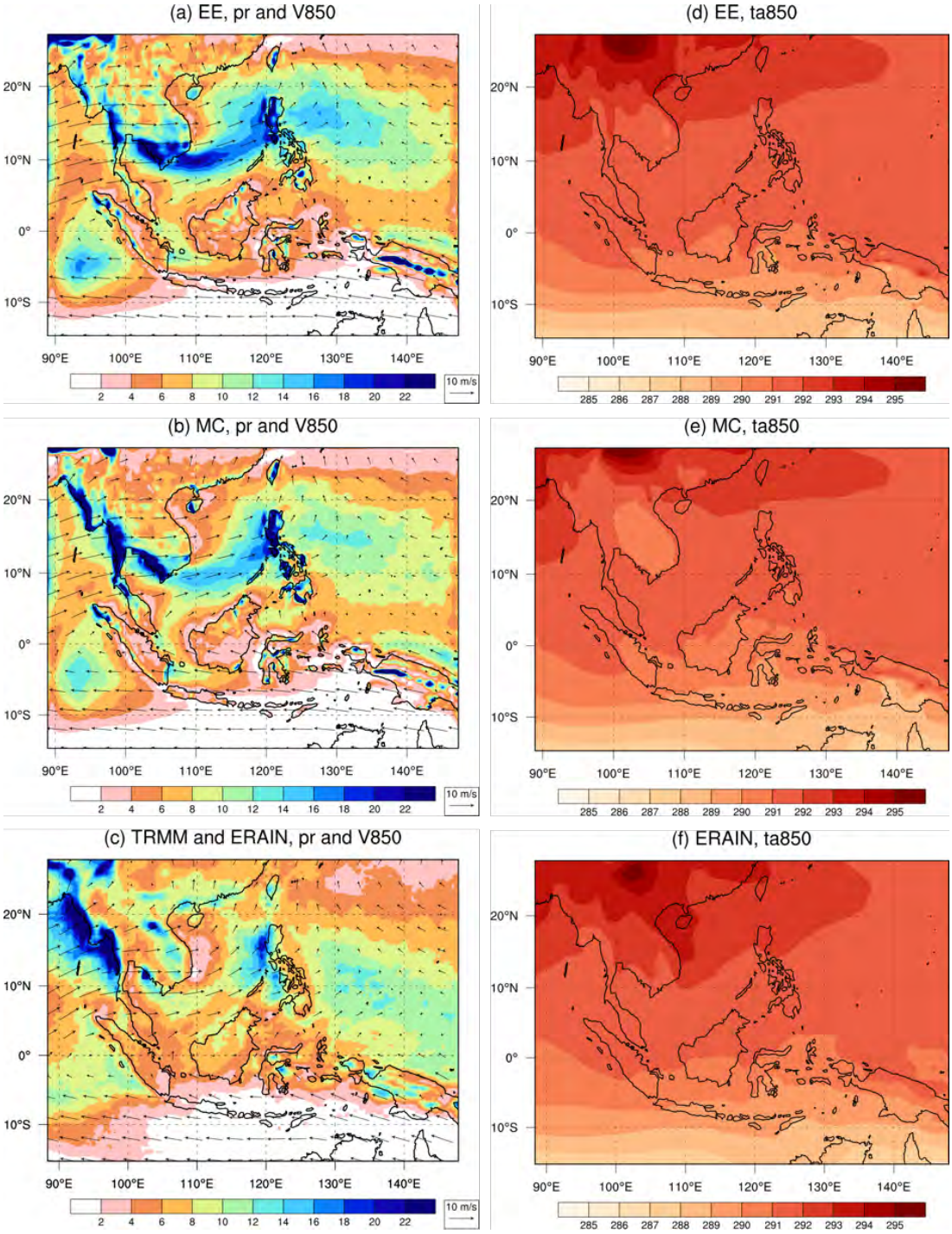

Fig. 3.2: JJA mean precipitation (shading; units: mm day^{-1}) and 850 hPa winds (see scale arrow at bottom right) from (a) EE, (b) MC simulations, and (c) TRMM3B42v7. JJA mean air temperature at 850 hPa (units: K) from (d) EE, (e) MC simulations, and (f) ERA-Interim reanalysis. The JJA mean values of the meteorological variables are computed for the period of 2001-2010.

Table 3.2: Pattern correlation coefficient (PCC), mean bias, and root-mean-square error (RMSE) between daily precipitation statistics from RegCM4 simulations and TRMM3B42v7 over the domain of 15S-27N, 90-147E in different seasons.

		DJF	MAM	JJA	SON
EE	PCC	0.647	0.522	0.584	0.702
	Mean Bias (mm day^{-1})	-0.246	0.208	0.0935	-0.0456
	RMSE (mm day^{-1})	3.53	3.55	4.46	3.21
MC	PCC	0.652	0.466	0.595	0.712
	Mean Bias (mm day^{-1})	-0.340	-0.406	-0.174	-0.281
	RMSE (mm day^{-1})	3.39	3.03	4.56	2.93

3.3.2 Annual cycle of precipitation

Fig. 3.3 compares the simulated annual cycle of 15-days running mean precipitation in four sub-regions with the TRMM data. In general, both simulations can reasonably capture the onset and end times of wet summer season that are associated with the Asian summer monsoon systems (Figs. 3.3a and 3.3b). In WIC, both MC and EE runs can produce a reasonable onset time of the Indian summer monsoon, but with an earlier retreat. MC simulations overestimate the summertime rainfall up to 6 mm day^{-1}; whereas EE's underestimation is about 2 to 4 mm day^{-1} (Fig. 3.3a). In SEC, both runs can capture the onset and end of East Asian summer monsoon, but are not able to reproduce characteristic active (in early-to-mid June), break (in mid-July) and revival phases (in early August) in this region. In general, EE improves the summer-time rainfall simulation over SEC, although both schemes underestimate the rainfall peak in June (Fig. 3.3b). The underestimated rainfall over SEC might be related to the overestimated rainfall over SCS, as suggested by Chow et al. (2006).

Over the Maritime Continent, EE simulations show better performance relative to MC in reproducing the annual cycle (Figs. 3.3c and 3.3d). In Sumatra, EE outperforms MC by capturing the temporal variations but it overestimates the rainfall

amount by around 2 mm day^{-1} from March to August (Fig. 3.3c). Also in Borneo, MC fails to produce the annual cycle (e.g. intraseasonal features); whereas EE reproduces reasonable temporal variations albeit with the rainfall from November to March underestimated (Fig. 3.3d).

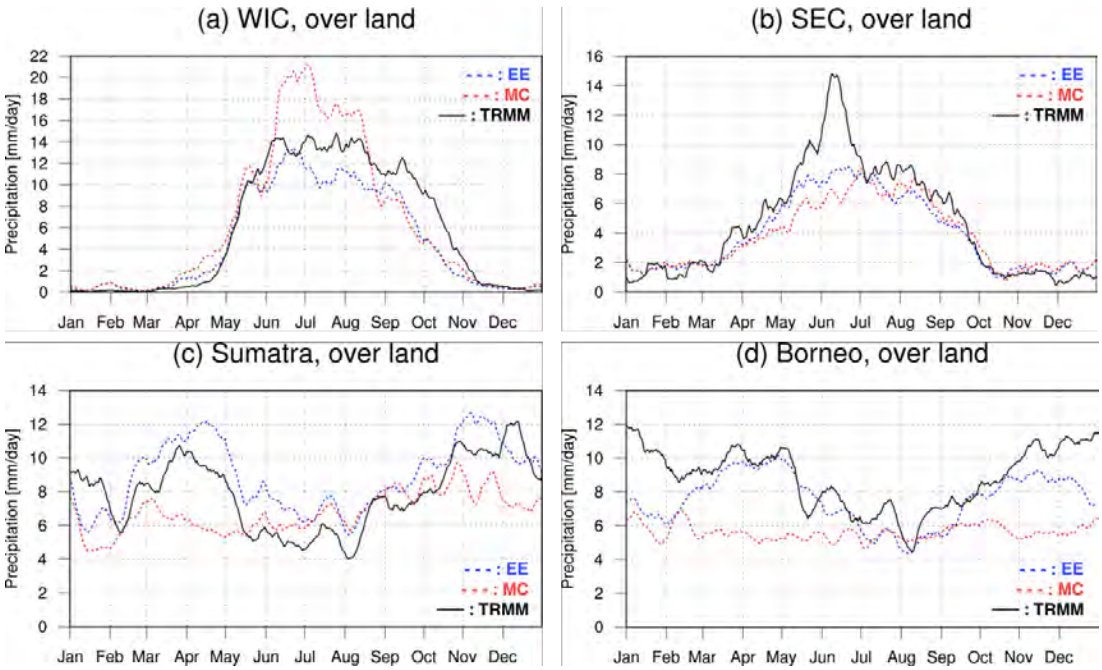

Fig. 3.3: Annual cycle of three-pentad running mean precipitation (units: mm day^{-1}) in the TRMM3B42v7 data and the RegCM4 simulations, averaged over (a) land area of western Indochina, (b) land area of southeastern China, (c) South China Sea, (d) the western North Pacific region, (e) the equatorial western North Pacific, (f) land area of Sumatra, (g) land area of Borneo and (f) land area of New Guinea, for the period of 2001-2010. The EE and MC simulations are shown by dashed blue and red lines respectively; whereas the TRMM3B42v7 data is shown by a solid black line.

3.4 Evaluation on simulated diurnal precipitation

3.4.1 Diurnal range

To quantify the amplitude of diurnal precipitation, we adopt the diurnal range (DR) following Kikuchi and Wang (2008). It is defined as the maximum minus minimum precipitation rate in its climatological mean 24-hour cycle. Fig. 3.4 shows DR of precipitation during JJA, computed based on outputs of the two sensitivity

experiments and the TRMM data. It is worth noting that the magnitude of DR is comparable to the seasonal mean precipitation, indicating the importance of diurnal rainfall over this region (see Figs. 3.2 and 3.4). In general, both simulations can reproduce large amplitudes of diurnal precipitation in regions with steep topography and near the coast. For example, strong DR is found along the Downa Range, Tenasserim Range, Cardamom Mountains in WIC, and over the Maritime Continent in both runs, with qualitative agreement with TRMM data. However, both of them cannot capture the pronounced DR along the Annamite Range in eastern Indochina. This is probably related to the coarse representation of orography in the model environments. Also, DR over SCS and equatorial WNP are slightly under-estimated in both simulations. In comparison to EE, MC simulations significantly underestimate DR along the western coastline of Indochina, the coastal areas of SEC, the Barisan Mountains in western Sumatra, the central mountain chains, southern part of Borneo, the Central Range and southern part of New Guinea up to 5 mm day^{-1}. Such underestimated amplitudes of diurnal rainfall by MC relative to EE are also found in other seasons (Fig. 3.5), but with their locations different in different seasons. For example, underestimations are mainly found over the Maritime Continent during winter (DJF). Furthermore, sensitivity tests are also conducted over another EA domain, which also leads to the same conclusion that MC underestimates the amplitude of DC as compared to EE simulations (Fig. 3.6).

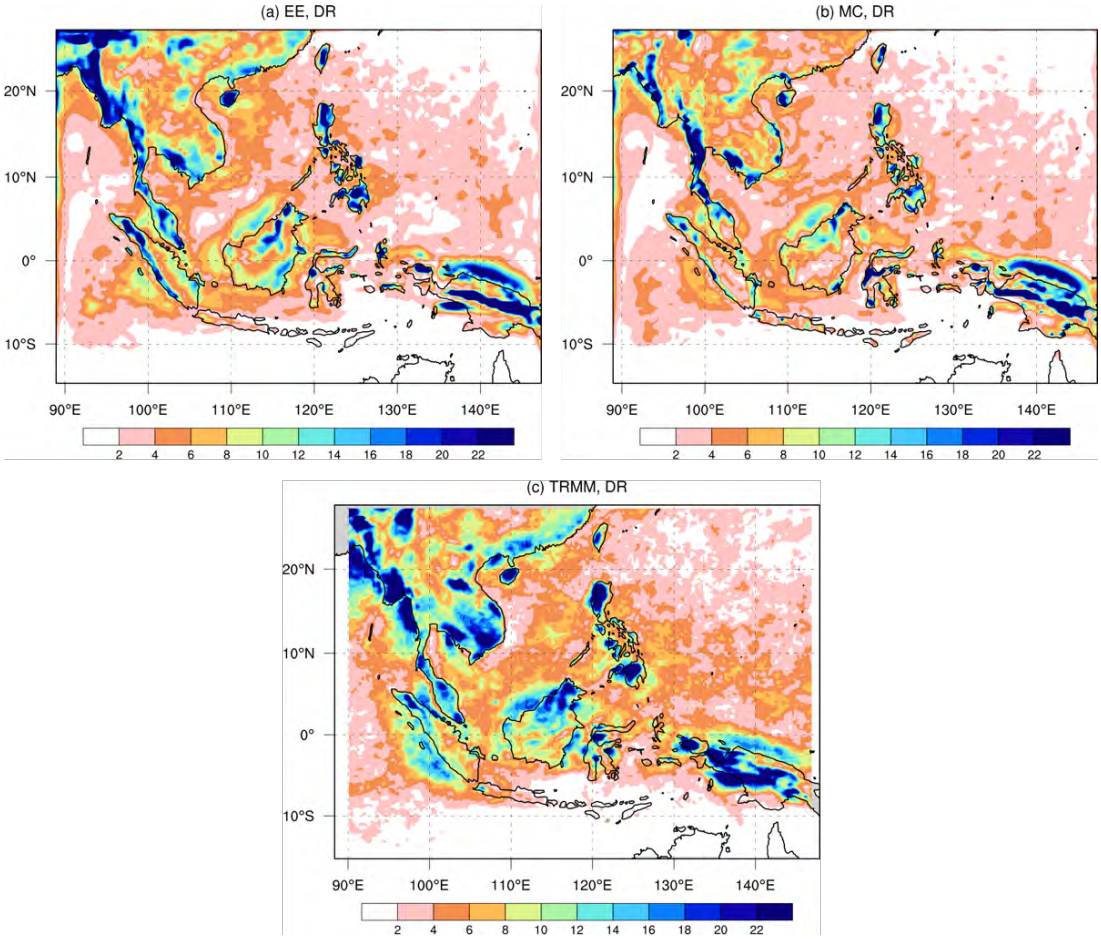

Fig. 3.4: Diurnal range (unit: mm day^{-1}) of precipitation during JJA computed based on (a) EE simulation, (b) MC simulation, and based on (c) TRMM3B42v7 for the period of 2001-2010.

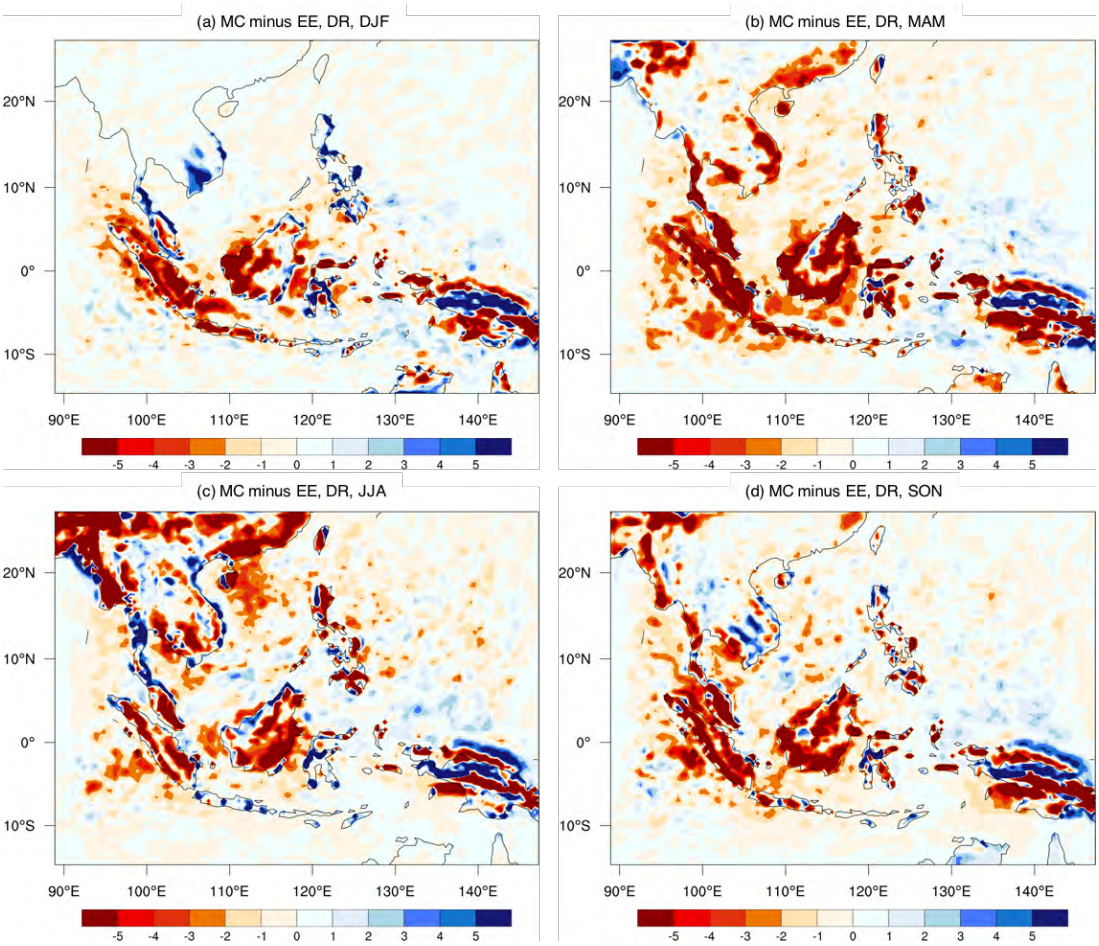

Fig. 3.5: MC minus EE diurnal range of precipitation (unit: mm day^{-1}) during (a) DJF, (b) MAM, (c) JJA, and (d) SON, for the period of 2001-2010.

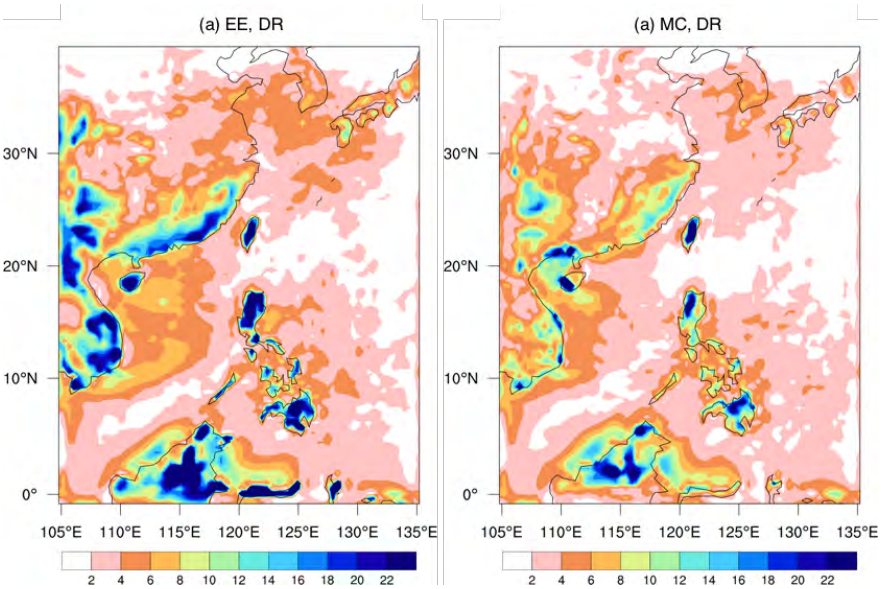

Fig. 3.6: As in Figs. 3.4a and 3.4b but for EA domain.

3.4.2 EOF analysis

Figs. 3.7 and 3.8 present the first two EOF patterns and the corresponding PC time series, derived from the JJA mean 24-hour cycle of δpr, based on the two sets of simulations and the TRMM data. For both EE and MC simulations, the first and second modes together can explain 87% and 85% of total domain integrated variance respectively, which is close to that of TRMM (83%). Indeed, the first two modes together represent the diurnal cycle; whereas the third and fourth modes combined act as a complementary semi-diurnal cycle to the sub-daily variations of precipitation. Kikuchi and Wang (2008) treated the first mode as a universal land-sea contrast that is associated with the marked difference in atmospheric response to solar radiation forcing over continents versus oceans. The second mode is regarded as a geographic variation to divide the coastal regime into two sub-regimes, namely seaside and landside coastal regimes. In our study, both simulations can reproduce such geographical variations that mark the different diurnal precipitation regimes in the tropics. For instance, positive EOF1 and negative EOF2 can be found over inland coastal areas of northern Borneo while negative EOF1 and positive EOF2 can be seen over the surrounding oceans around Borneo, which agree with the TRMM. However, they both fail to reproduce the robust feature over the Annamite Range in eastern Indochina; this is consistent with the underestimated DR there (see Fig. 3.5).

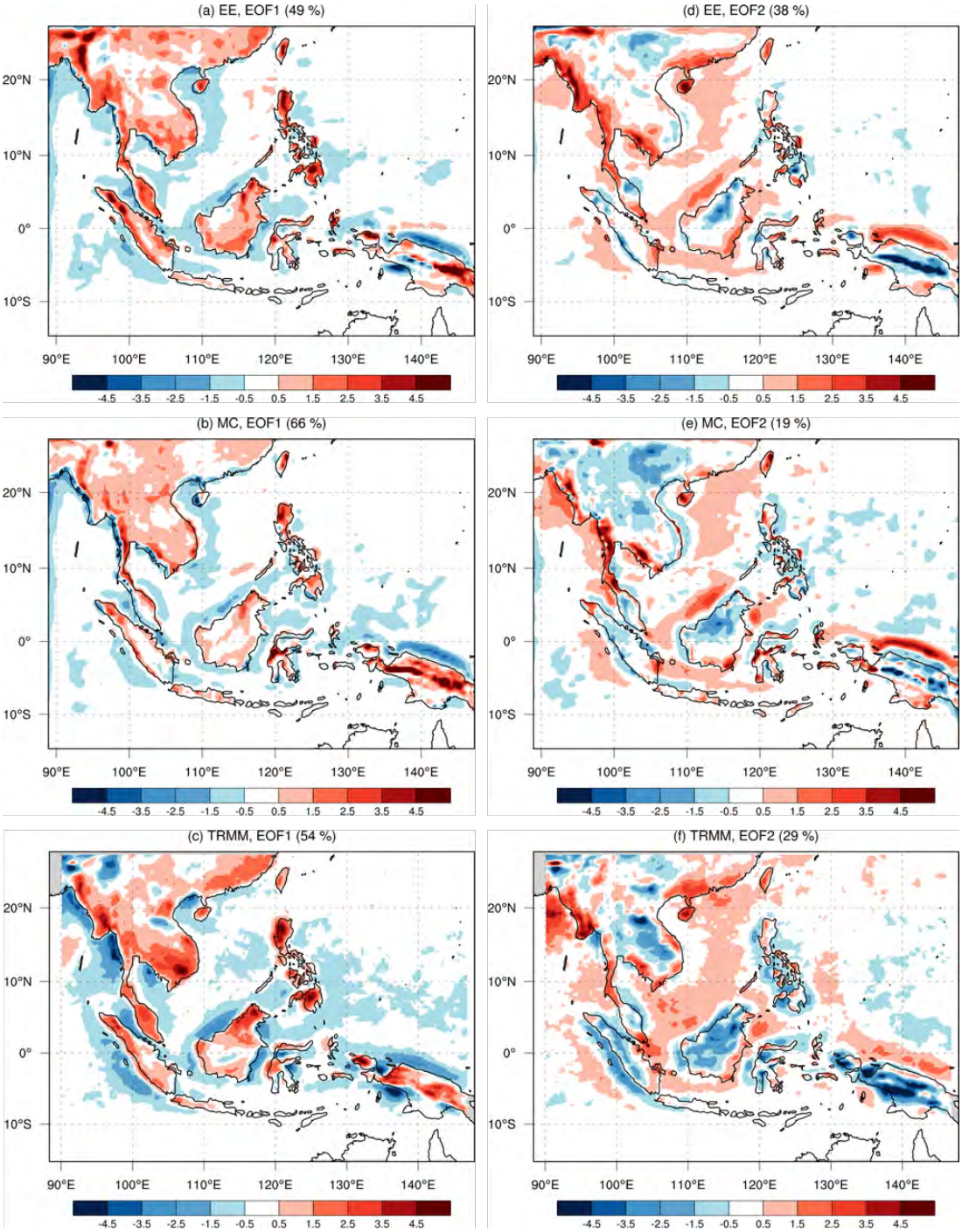

Fig. 3.7: The first EOF pattern (standardized) of JJA mean 24-hour cycle of precipitation anomalies (δpr), computed based on (a) EE simulation, (b) MC simulation, and based on (c) TRMM3B42v7 for the period of 2001-2010; (d), (e) and (f) as in (a), (b) and (c), but for the second standardized EOF pattern. The percentage of total variance explained by the respective EOF pattern is shown in the parentheses on the top of each sub-figure.

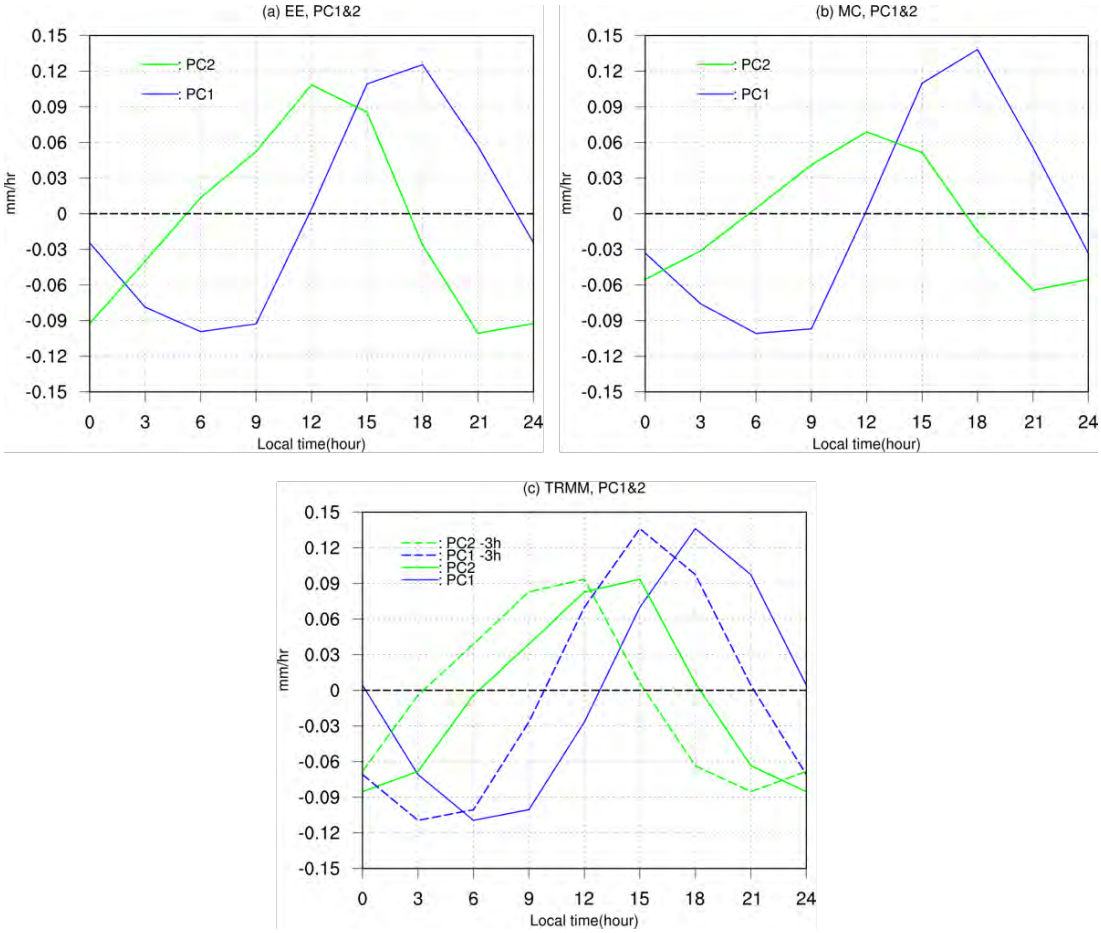

*Fig. 3.8: The corresponding first (*purple*) and second (*green*) PC time series of JJA mean 24-hour cycle of precipitation anomalies (δpr), computed based on (a) EE simulation, (b) MC simulation, and based on (c) TRMM3B42v7 for the period of 2001-2010. A minus-3h adjustment has been applied to TRMM data (*in dashed lines*) in (c), as suggested by Kikuchi and Wang 2008.*

For EE simulations, both EOF1 and 2 patterns compare well with those based on TRMM data, except over the eastern Indochina, SCS and WNP (Figs. 3.7a, 3.7c, 3.7d and 3.7f). The amplitude and phase of PC1 match well with those in TRMM, with its peak times found at 1800LT and 0600LT over land and ocean respectively. Besides, the amplitude of PC2 is slightly larger than that in TRMM, and with its phase lagging behind by 3-hour (Figs. 3.8a and 3.8c). For MC simulations, there is a significant reduction in the importance of EOF2 (Fig. 3.7f). Both EOF1 and 2 patterns match fairly well with those in TRMM, except over regions where EE does not

perform well. In fact, there are also locations where the MC-simulated EOF2 pattern does not match that from TRMM, e.g. the coastal areas of SEC and inland part of Indochina (Figs. 3.7b, 3.7c, 3.7e and 3.7f). Similar to EE, the amplitude and peak time of PC1 in MC simulations compare reasonably well with those in TRMM. However, the amplitude of PC2 is significantly underestimated and its phase also lags behind TRMM by 3 hours (Figs. 3.8b and 3.8c).

This underestimated amplitude in PC2 corresponds to a reduced afternoon peak (1200 to 1500 LT) in regions with positive EOF2 values and a reduced evening/midnight peak (2100 to 0000 LT) in regions with negative EOF2 values. In other seasons, reduced DR of precipitation is also mainly associated with the suppression of the second mode in MC simulation (see Figs. 3.9 and 3.10). Kikuchi and Wang (2008) argued that the diurnal phase derived from TRMM3B42 was systematically lagged by about 3h, by comparing the TRMM3B42 and 3G68 datasets, and suggested to add a minus-3h adjustment to the TRMM3B42 time series. If we consider their suggestion, the peak time of PC1 (PC2) time series of both simulations will lag behind (match with) that in TRMM.

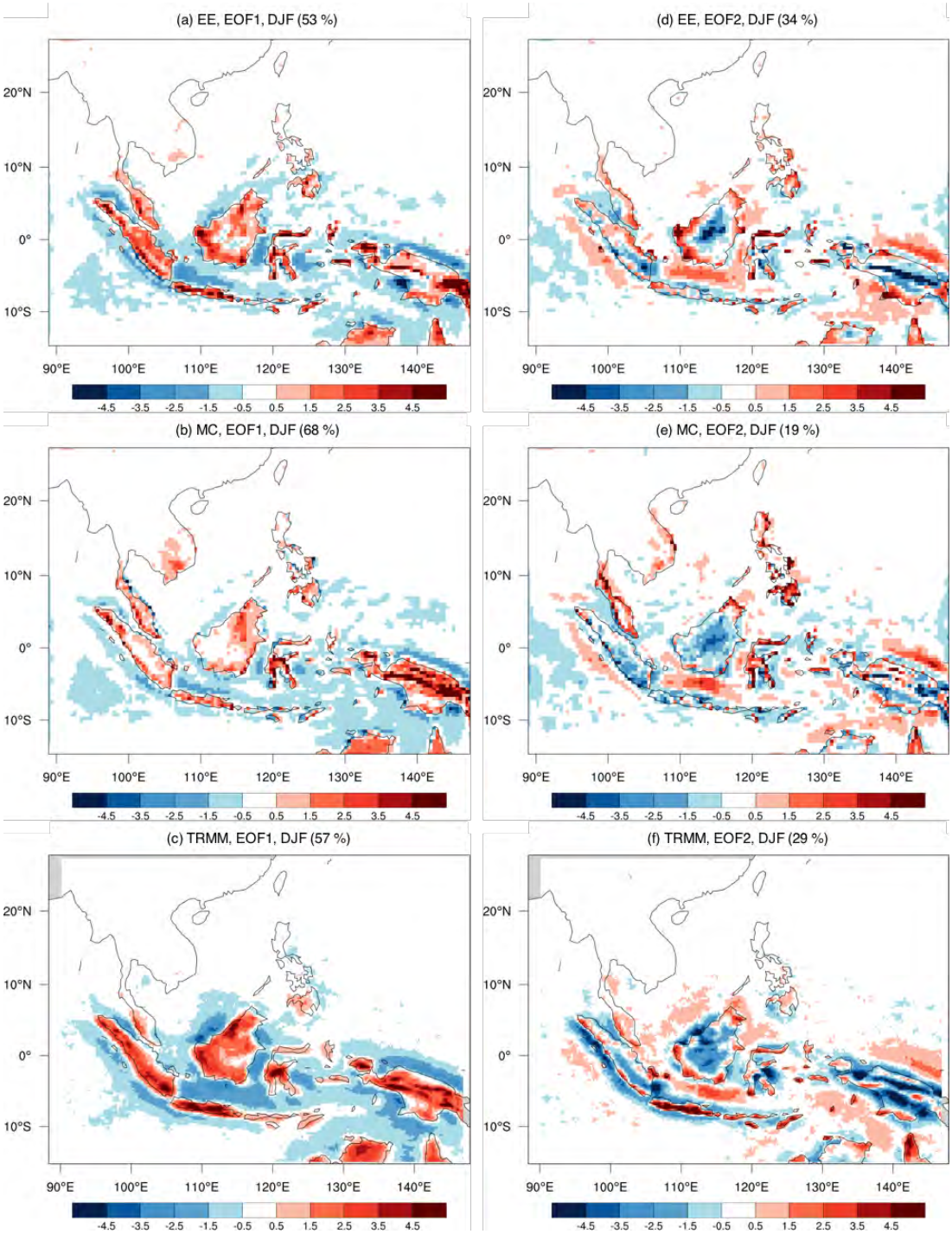

Fig. 3.9: As in Fig. 3.7 but for DJF.

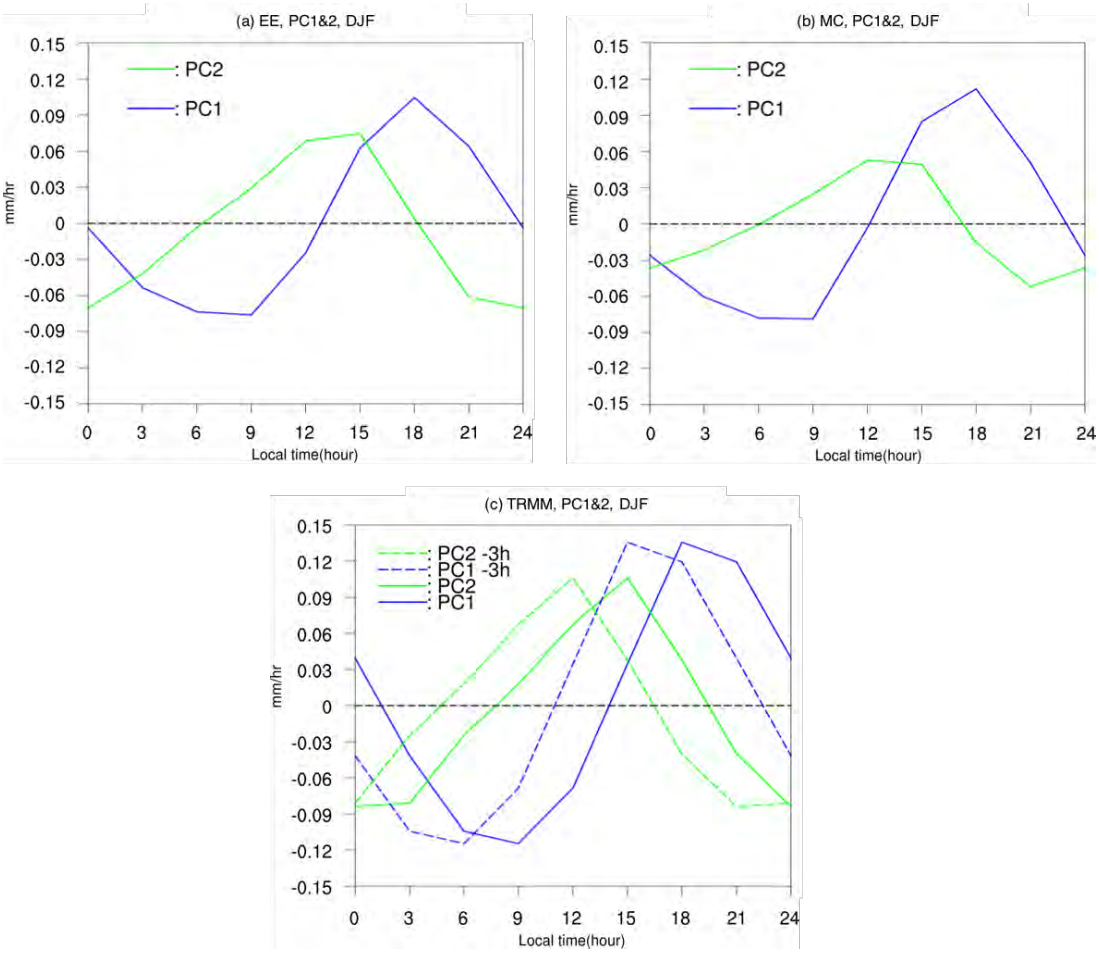

Fig. 3.10: As in Fig. 3.8 but for DJF.

3.4.3 Suppressed afternoon and evening precipitation peaks

Figs. 3.11a, 3.11b and 3.11c show time-distance cross diagrams of δpr in SEC, derived from EE simulation, MC simulation, and TRMM3B42v7 data respectively. The lower panels of Figs. 3.11a, 3.11b and 3.11c show the average topographic height in SEC. EE simulation can capture well the spatio-temporal characteristics of diurnal rainfall over SEC, including the morning and afternoon peaks in coastal and inner regions respectively, as compared to the TRMM; whereas MC simulation fails to capture these features. In the seaside coastal area of SEC (within 100km offshore), EE simulation produces a rainfall peak at around 0900LT, which is 3-hour later than the observed (Figs. 3.11a and 3.11c). The simulated magnitude of this morning peak is close to the

observed value (2 to 4 mm day^{-1}). On the other hand, over the inland area of SEC (at least 100 km inshore), EE simulation produces another rainfall peak around 1200 to 1500LT, which is slightly earlier than the observed (1500LT) and weaker than the observed by 2 mm day^{-1}. Phase propagation of diurnal rainfall from the seaside coastal areas to inner areas of SEC is observed in TRMM, and an afternoon rainfall maximum is observed at around 150 km away from the coast. The phase propagation and the afternoon rainfall maximum are captured in EE simulation but the simulated location of maximum rainfall is found to be slightly closer to the coast. In contrast, MC simulation produces a too early morning peak (0300LT) in the seaside coastal area and a too weak afternoon peak (an underestimation up to 6 mm day^{-1}) in the inland area of SEC, as compared to TRMM (Figs. 3.11b and 3.11c).

Figs. 3.11d, 3.11e and 3.11f show time-distance cross diagrams of δpr in Borneo, derived from EE simulation, MC simulation, and TRMM3B42v7 data respectively, and the average terrain height in lower panels. Ichikawa and Yasunari (2006) showed that there are two regimes for the diurnal rainfall over Borneo, namely easterly and westerly regimes, which are defined by the predominating low-level wind direction. Although both simulations are able to reproduce the easterly regime, EE simulation outperforms MC simulation in terms of the timing and magnitude of the rainfall peak. In MC simulation, the rainfall peak is found to be 3-hour earlier and weaker (by 4 mm day^{-1}) as compared to TRMM. However, both simulations cannot reproduce the westerly regime which is associated with the passage of intraseasonal atmospheric disturbance, with MC simulation somewhat captures the eastward migration of rainfall system. The absence of westerly regime could be attributed to the overestimated easterly over Borneo in JJA in model simulations as compared to reanalysis (Figs. 3.2a, 3.2b and 3.2c) and the strong easterly over Borneo in model

simulations might be associated with its performance to capture the interaction of intraseasonal disturbances such as MJO with the large-scale circulation there.

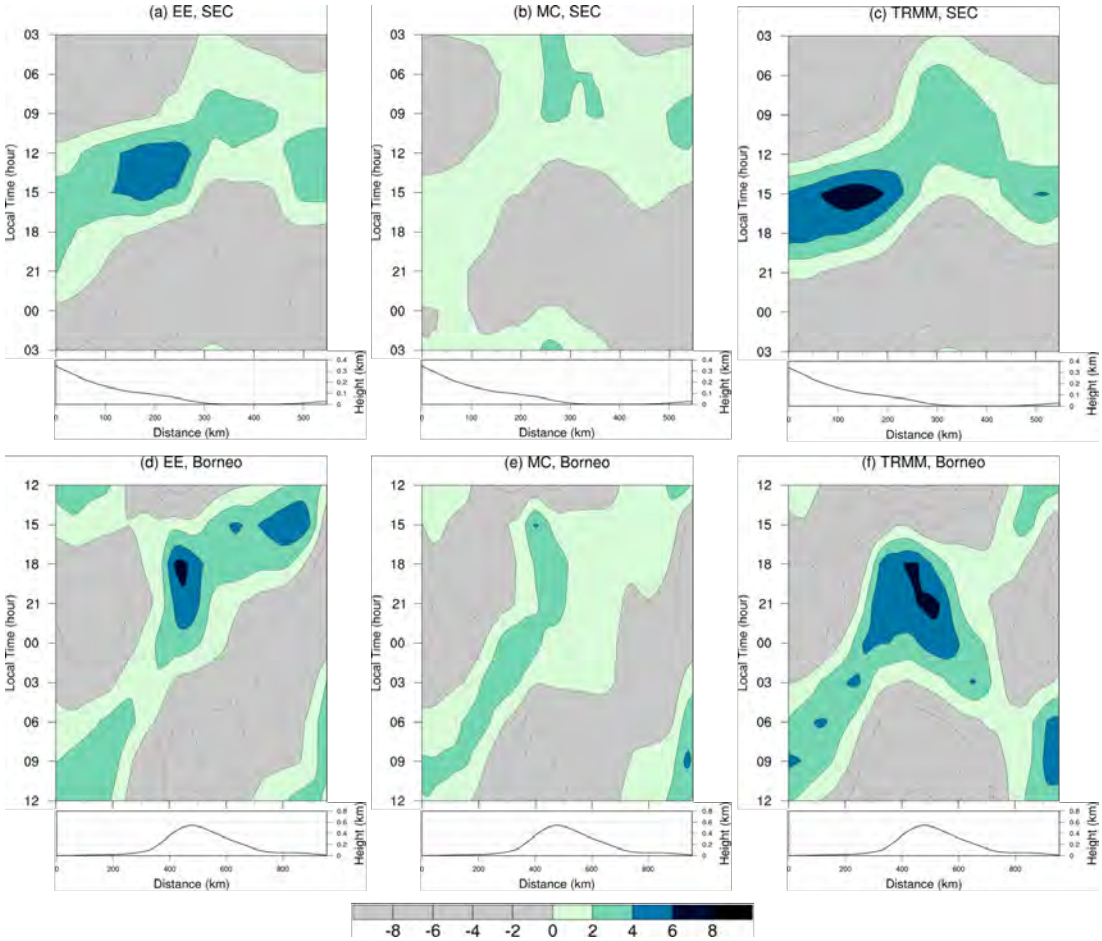

Fig. 3.11: Time-distance cross diagrams of precipitation anomalies (δpr; units: mm day^{-1}) along the direction of red dashed arrow (as shown in Fig. 3.1), averaged over southeastern China. The diagrams are derived based on the JJA mean departure of precipitation from its 24-hour cycle, based on (a) EE simulation, (b) MC simulation, and (c) TRMM3B42v7 data, for the period of 2001-2010. The lower panels of (a), (b) and (c) indicate the terrain height, averaged over southeastern China. (d), (e) and (f) as in (a), (b) and (c) but for Borneo.

In addition, the spatio-temporal variations of the diurnal rainfall over WIC, Sumatra, and New Guinea (not shown) are also better captured in EE simulation, as compared to MC simulation. For example, EE simulation can reproduce well the propagating feature of diurnal phase across the coastline of WIC and the afternoon

peak over the inland areas, as compared to TRMM; whereas, MC simulation is again not able to produce the pronounced afternoon peak at the Downa Range, which lies parallel to and around 200 km away from the western coastline of Indochina (see Figs. 3.12a, 3.12b, 3.12c). Likewise, EE simulation can reproduce well the evening peak near Barisan Mountains of western Sumatra as well as its northeastward phase migration towards inland region, but the evening peak is found to be 3-hour earlier than the observed; whereas MC simulation underestimates this evening peak by about 4 mm day^{-1} and barely produces the observed northeast migration of rainfall peak. (see Figs. 3.12d, 3.12e, 3.12f).

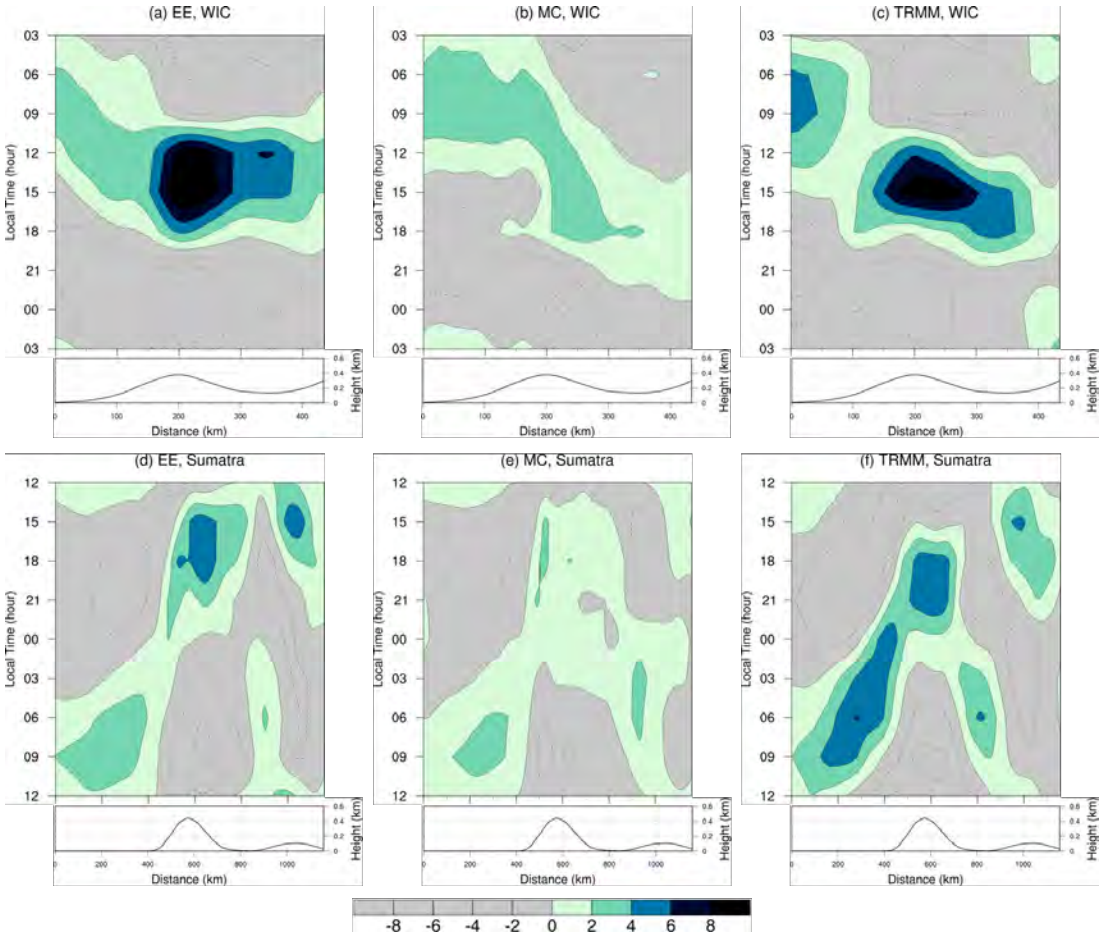

Fig. 3.12: As in Fig. 3.11, but for western Indochina and Sumatra.

3.4.4 Suppressed low-level moisture convergence

In order to explain the discrepancy in the magnitude of afternoon precipitation peak over the inland areas of SEC between two simulations, we have compared the vertical cross sections of the convergence of moisture fluxes as well as the projections of wind vectors between two simulations. It is found that in EE simulation, there is a strong low-level (from 1000hPa to 850hPa level) moisture convergence signal starting at 0900LT near the terrain-slope of SEC (around 100 km inshore; see Fig. 3.13a); whereas, in MC simulation, the convergence of moisture fluxes is weak there (Fig. 3.13c). Consistently, MC simulation shows weaker upward motion, suggesting a less intense convection, as compared to EE simulation. At around 1200 to 1500LT, convective precipitation reaches its maximum (i.e. afternoon peak). Meanwhile, the strong low-level moisture convergence signal further migrates towards the inland area and continues to lift moist air up, though it is weakened (Fig. 3.13b), and consequently the diurnal phase propagates inshore. Again, the low-level moisture convergence as well as the upward motion in MC simulation remain weaker than those in EE simulation (by up to 0.05 Pa s^{-1} for pressure velocity; Fig. 3.13d).

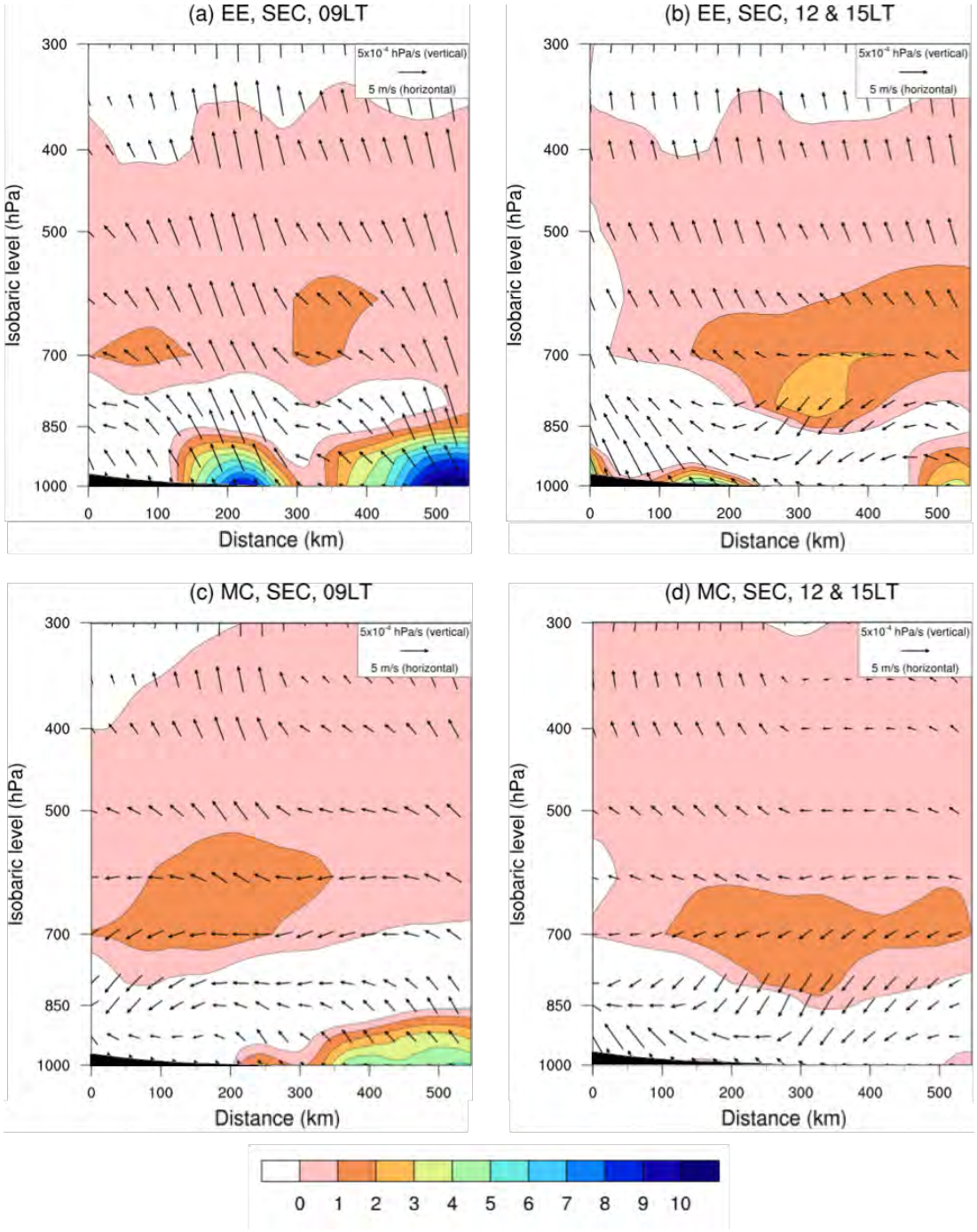

Fig. 3.13: The vertical cross section of convergence of moisture fluxes (shading; units:10^{-5} g kg^{-1} s^{-1}) along the direction of red dashed arrow (as shown in Fig. 3.1), averaged over southeastern China (a) at 0900LT, (b) averaged between 1200LT and 1500LT, over JJA based on EE simulation. Also superimposed on (a) and (b) are the vertical cross section of the projection of winds on the cross section plane (vectors; see scale arrow at upper right). Note that the horizontal and vertical velocity vectors are not on same scale. (c) and (d) as in (a) and (c), but based on MC simulation. Black shading indicates the terrain.

Similarly, to explain the weak evening precipitation peak on the leeward side (western side) of central mountain range of Borneo in MC simulation, we have also compared the vertical cross sections of the convergence of moisture fluxes as well as the projections of wind vectors there in two simulations. At 1500LT, a strong low-level moisture convergence is found near western Borneo in the EE simulation, with a deep convection developing (Fig. 3.14a); whereas, the moisture convergence and upward motion are relatively weaker in MC simulation (Fig. 3.14c). At around 1800 to 2100LT, convergence of low-level moisture persists and migrates further westward at the leeward side, under influence of the predominating low-level easterlies (Fig. 3.14b). Deep convection continues to develop vertically and propagates offshore, probably due to the intense intrusion of easterly winds from the windward side into the leeward side and also the associated gravity wave response (one mechanism as proposed by Satomura 2000). In the meantime, convective precipitation reaches its maximum (i.e. evening peak). However, in MC simulation, the low-level moisture convergence as well as the associated convection are relatively weaker (Fig. 3.14d), which might be related to the poor representation of the interaction between local circulation (e.g. land breezes) and the complex terrain from late afternoon to evening.

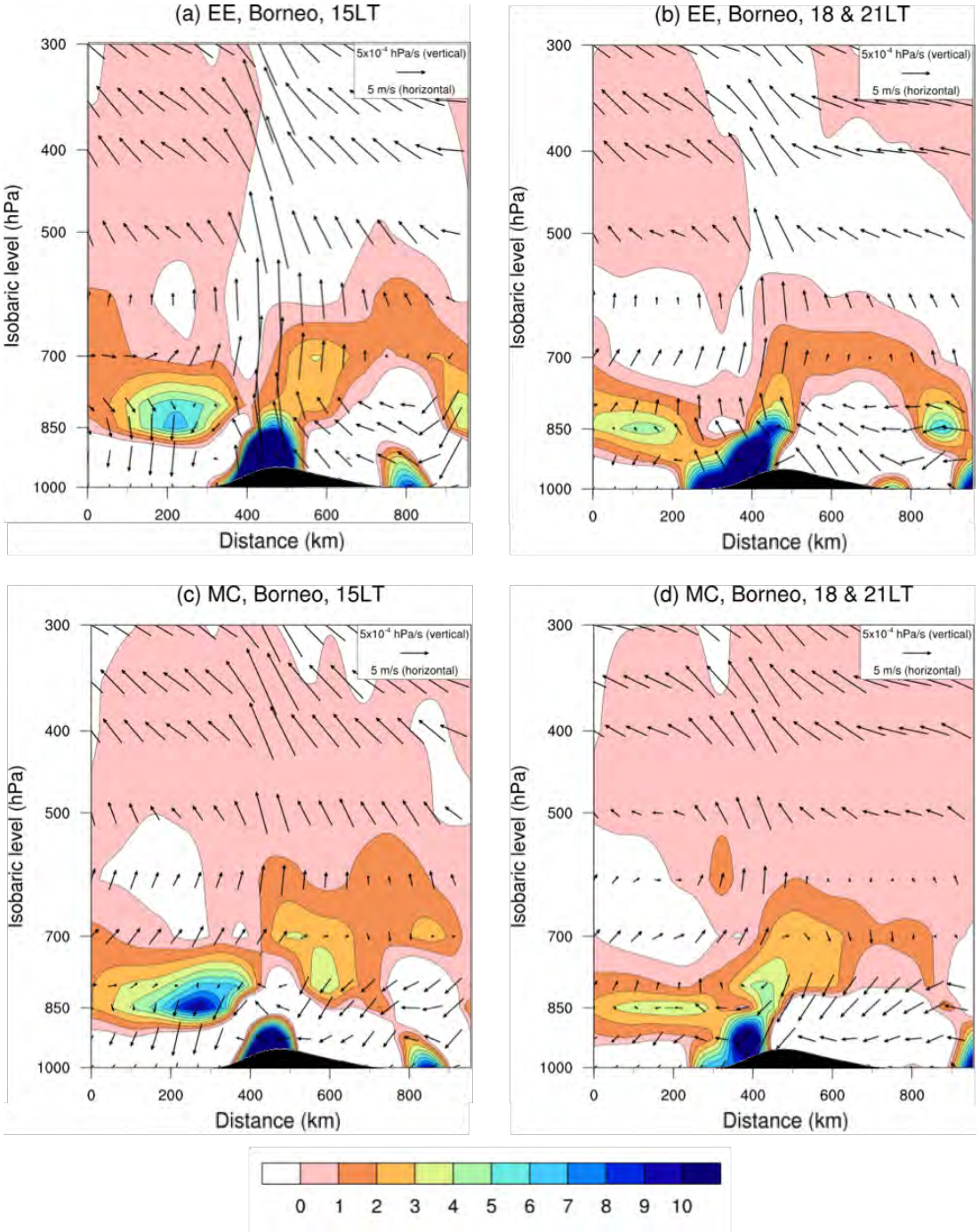

Fig. 3.14: (a) as in Figs. 3.13a, but at 1500LT over Borneo. (b) as in Figs. 3.13b, but averaged between 1800LT and 2100LT over Borneo. (c) and (d) as in (a) and (c), but based on MC simulation. Black shading indicates the terrain.

Huang et al. (2013) proposed that in the previous version of RegCM4, some cumulus schemes, such as Grell scheme with AS-type closure, have biases on the position of upward motion of the sea breeze circulation in SEC as compared to

observation, thereby leading to anomalous downward motion and moisture flux divergence over the inner regions of SEC. In addition to their proposed mechanism, the suppressed low-level moisture convergence in the inland area of SEC in MC simulation might also be related to the other differences in the performance of Emanuel and Grell schemes.

Fig. 3.15 shows the mean 24-hour cycle of 2-m air temperature, 2-m specific humidity, and cloud area fraction, over SEC and Borneo in JJA based on EE and MC simulations. Firstly, the overall surface temperature over SEC is lower in MC simulation than in EE simulation in the 24-hour cycle, which in turn probably reduces the overall convective instability there in MC simulation (Fig. 3.15a). Secondly, there is less available surface moisture in MC simulation, as compared to EE simulation (Fig. 3.15b). Lastly, as Emanuel scheme is more efficient in developing intense convection and drying out the atmospheric moisture, the cloud amount is reduced (Fig. 3.15c) and more shortwave radiation can reach the surface, thereby further enhancing low-level temperature in the afternoon and increasing convective instability, as compared to Grell scheme. As a result, the surface temperature is even more cooler and the low-level atmosphere is relatively more stable around 1200LT in MC simulation, as compared to EE simulation (Fig. 3.15b). Thus, convection is suppressed and convective precipitation is less intense in the afternoon over SEC in MC simulation.

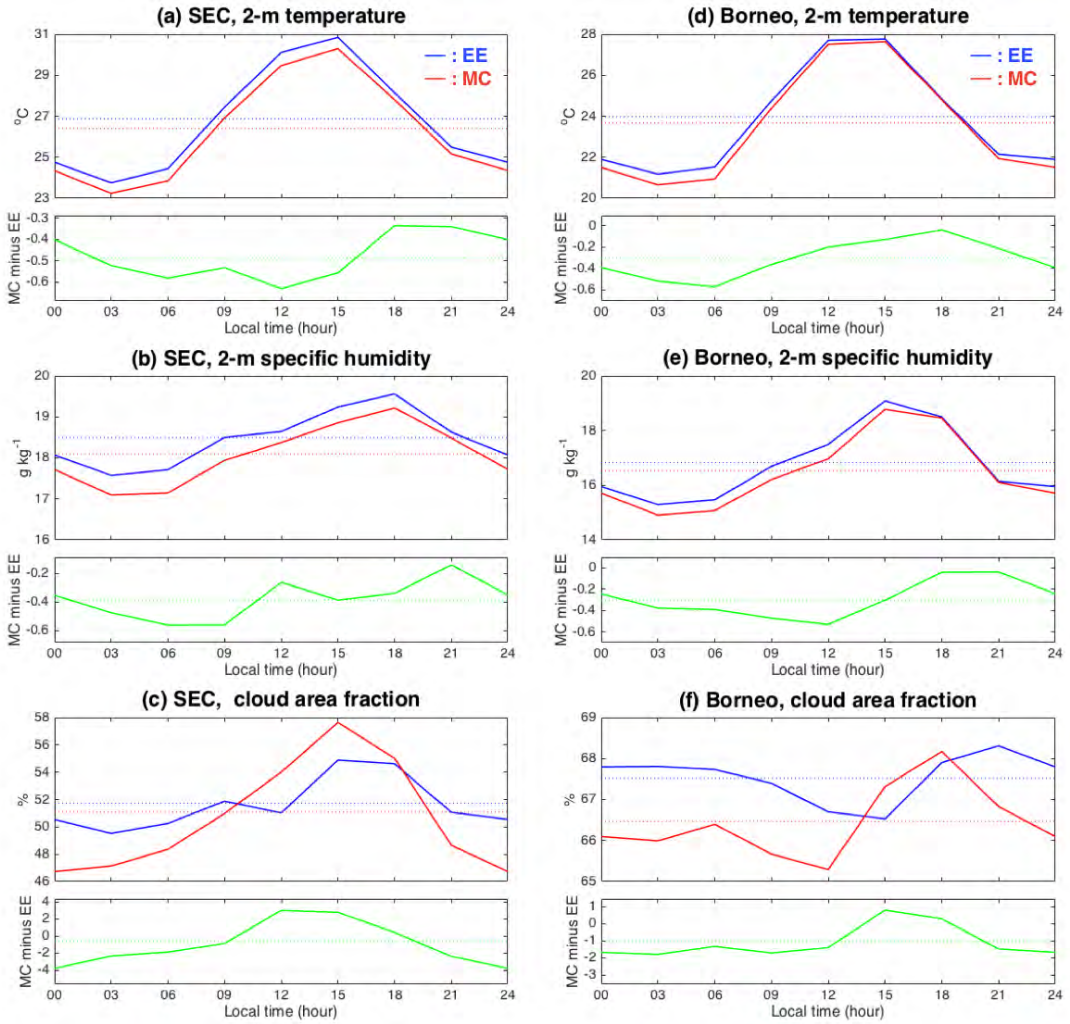

Fig. 3.15: The mean 24-hour cycle of (a) surface air temperature (units: ℃), (b) surface specific humidity (units: g kg^{-1}), and (c) cloud area fraction, averaged over southeastern China in JJA, based on EE simulation (in solid red) and MC simulation (in solid blue). The dotted horizontal lines represent the 24-hour mean. (d), (e) and (f) as in (a), (b) and (c), but over Borneo. Lower panel in each figure gives the MC minus EE values (in solid green). The dotted horizontal green line represent the difference in mean values between MC and EE simulations.

However, the mechanisms governing the suppression (as compared to EE simulation) of low-level moisture convergence and correspondingly the afternoon (i.e. around 1200 and 1500LT) and evening (i.e. around 1800 and 2100LT) precipitation peaks over SEC and Borneo in MC simulation appear to be different to some extent. Despite the overall cooler surface air temperature and the lower surface moisture availability (Figs. 3.15d and 3.15e), the poorer representation of interactions between

local land breezes, large-scale low-level winds and complex terrain may also be responsible for the suppressed low-level moisture convergence on the leeward side (i.e. western side) of central mountains of Borneo in MC simulation, as compared to EE simulation. One possible mechanism is that again Grell scheme produces less intense convection and is less efficiently in drying out the atmosphere as compared to Emanuel scheme, thereby favoring low-level cloud formation (Fig. 3.15f), reducing outgoing longwave radiation, heating up the low level atmosphere and disrupting the night-time land breeze circulation locally. Another possible mechanism may be the poor representation of the intrusion of low-level easterly winds from eastern side to western side of Borneo and the associated gravity wave response (see Fig. 3.14).

In order to attribute the suppressed low-level moisture convergence to poor representation of evening local circulation in particular over Borneo in MC simulation. Based on the moisture budget analysis, we have computed the anomalies of vertically-integrated low-level moisture convergence ($\delta LLMC$):

$$\begin{aligned}\delta LLMC &= -\int_{p_s}^{500\,hPa} \boldsymbol{\nabla}\cdot(q\mathbf{V}-\bar{q}\overline{\mathbf{V}})\frac{dp}{g}\\ &= -\int_{p_s}^{500\,hPa} \boldsymbol{\nabla}\cdot\delta q\overline{\mathbf{V}}\frac{dp}{g}-\int_{p_s}^{500\,hPa} \boldsymbol{\nabla}\cdot\bar{q}\,\delta\mathbf{V}\frac{dp}{g}-\int_{p_s}^{500\,hPa} \boldsymbol{\nabla}\cdot\delta q\delta\mathbf{V}\frac{dp}{g}\\ &= \delta LLMC_I+\delta LLMC_{II}+\delta LLMC_{III} \qquad (3.2)\end{aligned}$$

where p_s is the surface pressure, q is the specific humidity at pressure level p, $\mathbf{V}$ is the horizontal wind vector in the pressure coordinate, and g is the gravitational acceleration. The three components represent the production or loss of moisture convergence due to the advection of moisture perturbations by mean wind, the advection of mean moisture by perturbed wind, and the advection of moisture perturbations by perturbed wind, respectively.

Subsequently, we have subtracted $\delta LLMC$ (and its individual components) in EE simulation from MC simulation (Fig. 3.16). The difference in $\delta LLMC$ between EE and MC simulations was found to be up to 10 mm day^{-1} near the central mountains in Borneo at around 1800LT and 2100LT. It is mainly caused by the suppressed $\delta LLMC_{II}$ (see Fig. 3.16c), which is associated with the mean moisture as well as the perturbed local winds in the evening (e.g. night-time land breeze circulation). This suggests that the evening local circulation over Borneo might be poorly represented in MC simulation.

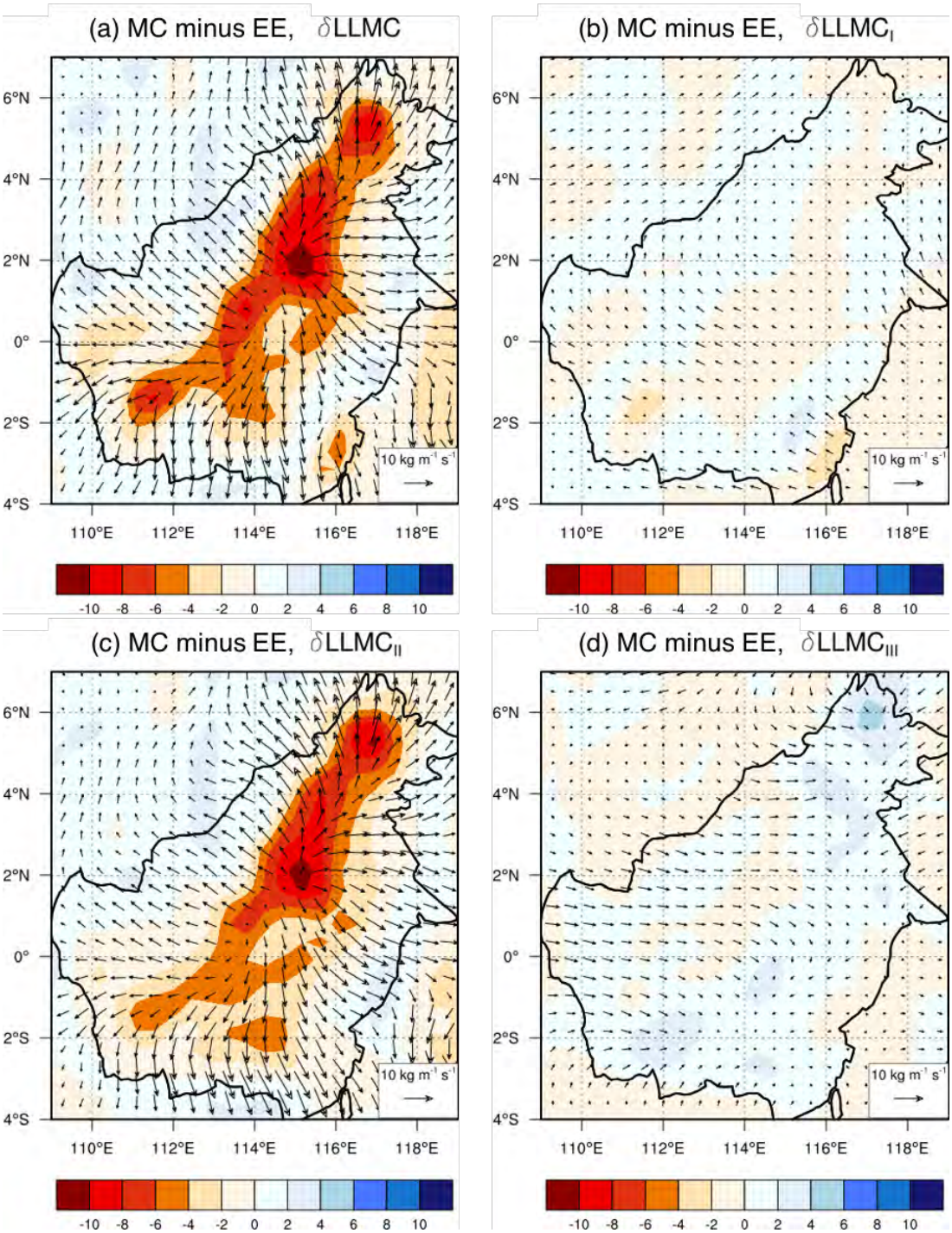

Fig. 3.16: MC minus EE anomalies of (a) vertically-integrated low-level moisture convergence (δLLMC; units: mm day^{-1}), (b) the corresponding first component (δLLMC$_I$; units: mm day^{-1}), (c) the second component (δLLMC$_I$; units: mm day^{-1}), and (d) the third component (δLLMC$_{III}$; units: mm day^{-1}). Also superimposed on each figure is the corresponding vertically-integrated moisture flux vectors (see scale arrow at bottom right). The values are averaged over 1800LT and 2100LT. See text for details.

3.5 Summary

In general, both simulations can reasonably capture the JJA mean precipitation features, including summer monsoon trough and orographic rainfall over WIC, and the low-level circulation in Southeast Asia, as compared to TRMM and ERA-Interim reanalysis. MC simulation improves rainfall over the SCS and east of the Philippines, but through Rossby wave response of two negative convective heating over these two regions it under(over)-estimates rainfall over land in SEC (western coastlines of Indochina and the Philippines). EE and MC simulations show cold biases in 850 hPa air temperature over the southern Indochina, northern SCS and northern Philippines, but with the latter showing even colder biases. These colder biases are associated with reduced diabatic heating.

Both simulations can capture most of the temporal variations in the annual cycle of precipitation over WIC and SEC regions, although discrepancies are usually found in summer season. Summer-time rainfall over WIC is under(over-)estimated in EE (MC) simulation; whereas that over SEC is improved in EE simulation, although both simulations cannot reproduce the characteristic phases of summer monsoon. For annual cycle over the Maritime Continent, EE simulation in general outperforms MC simulation. In Sumatra and Borneo, EE simulation outperforms MC simulation by reproducing the temporal variations, although it overestimates the rainfall amount from March to August and November to March respectively.

Regarding the DC of precipitation, it is found that RegCM4 can reproduce well its characteristics in SEA, but notable underestimation of its amplitude is found in MC simulation as compared to EE simulation. Such bias is also found in other seasons and another East Asia domain. Based on EOF analysis, the peak hour of PC1 time series of both simulations matches well with TRMM but that of PC2 lags behind TRMM by

3 hour. The aforementioned bias in amplitude of DC is reflected in the suppressed amplitude of PC2 in MC simulation relative to EE simulation. The suppressed amplitude in PC2 corresponds to a suppressed afternoon peak (1200 to 1500LT) in SEC and WIC, and a suppressed evening/midnight peak (1800 to 0000LT) in Borneo, Sumatra and New Guinea.

In the seaside coastal area of SEC, EE simulation produces a rainfall peak of magnitude close to the observed, which is however 3-hour later than the observed. In the inland area of SEC, EE simulation produces another rainfall peak around 1200 to 1500LT, which is weaker and 3-hour earlier than the observed. In contrast, MC simulation produces a too early morning peak in the seaside coastal area and a too weak afternoon peak in the inland area of SEC.

In addition to an overall cooler mean surface temperature and lower mean surface moisture, the suppressed afternoon rainfall peak in inland areas of SEC (also in WIC) in MC simulation is mainly attributed to the less intense convection as well as the less efficient drying of the atmosphere particularly in the afternoon in Grell scheme (as compared to Emanuel scheme). This leads to enhanced cloudiness and reduced shortwave radiation, which further reinforces the low-level cooling and low-level atmospheric stability. Therefore, low-level moisture convergence and the precipitation peak over the inland area of SEC are suppressed in MC simulation.

For Borneo, both simulations can reproduce the easterly regime, but with EE simulation outperforms MC simulation in terms of timing and magnitude of the evening peak over the inland area; whereas in MC simulation, the rainfall peak is found to be 3-hour earlier and weaker than the observed. However, both simulations cannot reproduce the westerly regime (i.e. the southeastward phase migration), which could be attributed to the overestimated low-level easterly over Borneo in JJA in both

model simulations as compared to reanalysis and the model performance to capture the interaction of intraseasonal disturbances with the large-scale circulation there.

In contrast to the case in SEC, the poor representation of interactions between local land breezes, large-scale low-level background winds and complex terrain may also be responsible for the suppressed low-level moisture convergence in the western Borneo in MC simulation, as compared to EE simulation. Further moisture budget analysis reveals that the difference in the low-level moisture convergence anomalies between EE and MC simulations is mainly caused by the moisture convergence due to the advection of mean moisture by perturbed wind (i.e. $\delta LLMC_{II}$), which in turn is related to the mean moisture and the perturbed local winds in the evening (e.g. night-time land breeze circulation).

Chapter 4

Conclusion and Future Direction

4.1 Major conclusions

4.1.1 Future changes in Asian Summer Precipitation Extremes

The summertime mean precipitation is projected to increase over many locations in the Asian monsoon region, despite a weakened low-level westerly monsoon wind in the future climate projection. Meanwhile, the summertime extreme precipitation is expected to be enhanced by about 0.9-6.9 mm day^{-1} over Eastern China, the Meiyu-Baiu rainband, Bay of Bengal and Central India, as inferred from increases of the simple daily precipitation intensity index and the 95th percentile of daily precipitation. PDFs for daily precipitation in these regions are expected to be modified significantly under global warming, with the greatest increase in probability found in the higher percentiles. Our result also suggests that the parametric gamma fitting method is an alternative way to accurately describe the change of daily precipitation rates up to about the 95th percentile, provided that the model-simulated PDFs of daily precipitation rates can be represented by gamma distribution. Under a model-projected warming of about 2.98 K in the lower-troposphere during MJJAS, precipitation extremes in Eastern China, BOB and central India were expected to increase at a rate of 5.5 to 8 % K^{-1}, which is roughly consistent with the Clausius-Clapeyron relation. The exception is Baiu rainband, where extreme precipitation scales as ~ 3% K^{-1} only.

TC numbers is projected to be reduced east of the Philippines and part of SCS, which is associated with the reduced low-level relative vorticity as well as the reduced variance of high-frequent vorticity fluctuations there. With TCs becoming more intense in a warmer climate, the TC-related rain rate is projected to increase. By considering these two competing factors separately, it was found that over northern

South China Sea and southeastern China, the accumulated TC-related rainfall will increase due to more intense TC rainrate; whereas over east of the Philippines and in southern Japan, it will decrease due to suppressed TC occurrence there in the future climate. In general, non-TC weather systems are the main contributor to enhanced precipitation extremes in various locations. The exception is Taiwan, where TC-related rainfall contributes to the increase of both the seasonal mean precipitation and daily rainfall intensity.

4.1.2 Precipitation simulations over Southeast Asia

Under the dynamical framework of RegCM4, MC and EE simulations are equally good in reproducing the JJA mean precipitation features as well as the low-level circulation in Southeast Asia. MC simulation improves rainfall over South China Sea and east of the Philippines but under(over)-estimates rainfall over land in SEC (western coastlines of Indochina and the Philippines). Regarding the annual cycle of precipitation, both simulations can capture its temporal variations over WIC, SEC and SCS regions although discrepancies are found in summer season. In particular, summertime rainfall over WIC is under(over-)estimated in EE (MC) simulation; whereas that over SEC (SCS) is improved in EE (MC) simulation. For annual cycle over Sumatra and Borneo, EE simulation outperforms MC simulation by capturing the temporal variations, although it overestimates the rainfall amount from March to August and November to March respectively.

It is found that MC simulation underestimates the amplitude of DC, in comparison to EE simulation. EOF analysis indicates that MC undermines the representation of DC by suppressing the second EOF mode as compared to EE. The suppressed second EOF mode corresponds to reduction of afternoon peaks over

coastal inland areas of western Indochina and southeastern China, and evening/midnight peaks over the mountain ranges of Sumatra, Borneo and New Guinea. Underestimations over western Indochina and southeastern China are mainly related to reduced low-level air temperature as well as enhanced cloudiness around 1200 to 1500 local time; whereas those over Sumatra, Borneo and New Guinea are associated with suppressed low-level moisture convergence due to poor representation of interaction between local circulation and complex terrain around 1800 to 0000 local time.

4.2 Future directions

The model-projected rate of amplification of extreme precipitation over the Baiu region is only about 3% K^{-1}, though precipitable water is expected to scale up by about 6 to 7% K^{-1} there. Future work is needed to investigate what dynamical factors might be responsible for the sub-CC scaling in this region. Besides, more work can be done for explaining the physical mechanism behind the CC scaling of extreme precipitation over Eastern China, Bay of Bengal and Central India, including the impacts of climate change on the large-scale circulations and the occurrence of various types of weather systems.

Also, the RegCM4 tuned in this study can be used to downscale coarse resolution CMIP5 GCM outputs to project future climate over East Asia. This way, one can use the downscaled products to address issues such as future changes in diurnal cycle of precipitation and other weather systems under global warming, and their impacts on extreme events over the EA region.

Bibliography

Alexander L V., Zhang X, Peterson TC, et al (2006) Global observed changes in daily climate extremes of temperature and precipitation. J Geophys Res Atmos 111:1–22. doi: 10.1029/2005JD006290

Allan RP, Soden BJ (2008) Atmospheric Warming and the Amplification of Precipitation Extremes. Science (80-) 321:1481–1484. doi: 10.1126/science.1160787

Allen MR, Ingram WJ (2002) Constraints on future changes in climate and the hydrologic cycle. Nature 419:224–32. doi: 10.1038/nature01092

Chang CP, Lei Y, Sui CH, et al (2012) Tropical cyclone and extreme rainfall trends in East Asian summer monsoon since mid-20th century. Geophys Res Lett 39:1–6. doi: 10.1029/2012GL052945

Chen C-S, Chen Y-L, Liu C-L, et al (2007) Statistics of Heavy Rainfall Occurrences in Taiwan. Weather Forecast 22:981–1002. doi: 10.1175/WAF1033.1

Cho H-K, Bowman KP, North GR (2004) A Comparison of Gamma and Lognormal Distributions for Characterizing Satellite Rain Rates from the Tropical Rainfall Measuring Mission. J Appl Meteorol 43:1586–1597. doi: 10.1175/JAM2165.1

Chow KC, Chan JCL, Pal JS, Giorgi F (2006) Convection suppression criteria applied to the MIT cumulus parameterization scheme for simulating the Asian summer monsoon. Geophys Res Lett 33:1–6. doi: 10.1029/2006GL028026

da Rocha RP, Morales C a., Cuadra S V., Ambrizzi T (2009) Precipitation diurnal cycle and summer climatology assessment over South America: An evaluation of Regional Climate Model version 3 simulations. J Geophys Res 114:1–19. doi: 10.1029/2008JD010212

Dai A (2001) Global Precipitation and Thunderstorm Frequencies. Part I: Seasonal

and Interannual Variations. J Clim 14:1092–1111. doi: 10.1175/1520-0442(2001)014<1092:GPATFP>2.0.CO;2

Dai A, Trenberth KE (2004) The diurnal cycle and its depiction in the community climate system model. J Clim 17:930–951. doi: 10.1175/1520-0442(2004)017<0930:TDCAID>2.0.CO;2

Dee DP, Uppala SM, Simmons AJ, et al (2011) The ERA-Interim reanalysis: Configuration and performance of the data assimilation system. Q J R Meteorol Soc 137:553–597. doi: 10.1002/qj.828

Dickinson RE, Henderson-Sellers A, Kennedy PJ (1993) Biosphere–atmosphere transfer scheme (BATS) version 1e as coupled to the NCAR community climate model.

Ding Y, Chan JCL (2005) The East Asian summer monsoon: An overview. Meteorol Atmos Phys 89:117–142. doi: 10.1007/s00703-005-0125-z

Diro GT, Giorgi F, Fuentes-Franco R, et al (2014) Tropical cyclones in a regional climate change projection with RegCM4 over the CORDEX Central America domain. Clim Change 125:79–94. doi: 10.1007/s10584-014-1155-7

Diro GT, Rauscher SA, Giorgi F, Tompkins AM (2012) Sensitivity of seasonal climate and diurnal precipitation over Central America to land and sea surface schemes in RegCM4. Clim Res 52:31–48. doi: 10.3354/cr01049

Donat MG, Lowry AL, Alexander L V., et al (2016) More extreme precipitation in the world's dry and wet regions. Nat Clim Chang 6:508–513. doi: 10.1038/nclimate2941

Easterling DR (2000) Climate Extremes: Observations, Modeling, and Impacts. Science (80-) 289:2068–2074. doi: 10.1126/science.289.5487.2068

Emanuel KA (2013) Downscaling CMIP5 climate models shows increased tropical

cyclone activity over the 21st century. Proc Natl Acad Sci 110:12219–12224. doi: 10.1073/pnas.1301293110

Emanuel KA (1991) A Scheme for Representing Cumulus Convection in Large-Scale Models. J. Atmos. Sci. 48:2313–2329.

Emanuel KA, Živković-Rothman M (1999) Development and Evaluation of a Convection Scheme for Use in Climate Models. J Atmos Sci 56:1766–1782. doi: 10.1175/1520-0469(1999)056<1766:DAEOAC>2.0.CO;2

Emori S, Brown SJ (2005) Dynamic and thermodynamic changes in mean and extreme precipitation under changed climate. Geophys Res Lett 32:1–5. doi: 10.1029/2005GL023272

Evans JP, Westra S (2012) Investigating the mechanisms of diurnal rainfall variability using a regional climate model. J Clim 25:7232–7247. doi: 10.1175/JCLI-D-11-00616.1

Fischer EM, Beyerle U, Knutti R (2013) Robust spatially aggregated projections of climate extremes. Nat Clim Chang 3:1033–1038. doi: 10.1038/nclimate2051

Frich P, Alexander L V., Della-Marta P, et al (2002) Observed coherent changes in climatic extremes during the second half of the twentieth century. Clim Res 19:193–212. doi: 10.3354/cr019193

Fujibe F (2013) Clausius-Clapeyron-like relationship in multidecadal changes of extreme short-term precipitation and temperature in Japan. Atmos Sci Lett 14:127–132. doi: 10.1002/asl2.428

Gao X-J, Shi Y, GiorgiI F (2016) Comparison of convective parameterizations in RegCM4 experiments over China with CLM as the land surface model. Atmos Ocean Sci Lett 2834:1–9. doi: 10.1080/16742834.2016.1172938

Giorgi F (2006) Regional climate modeling: Status and perspectives. J Phys IV

139:101–118. doi: 10.1051/jp4:2006139008

Giorgi F, Coppola E, Solmon F, et al (2012) RegCM4: Model description and preliminary tests over multiple CORDEX domains. Clim Res 52:7–29. doi: 10.3354/cr01018

Giorgi F, Jones C, Asrar GR (2009) Addressing climate information needs at the regional level: The CORDEX framework. World Meteorol Organ Bull 58:175–183.

Grell G a. (1993) Prognostic Evaluation of Assumptions Used by Cumulus Parameterizations. Mon. Weather Rev. 121:764–787.

Grell GA, Dudhia J, Stauffer DR (1994) A description of the Fifth-generation Penn State/NCAR Mesoscale Model (MM5).

Groisman PY, Karl TR, Easterling DR, et al (1999) Changes in the probability of heavy precipitation: Important indicators of climatic change. Clim. Change 42:243–283.

Groisman PY, Knight RW, Easterling DR, et al (2005) Trends in intense precipitation in the climate record. J Clim 18:1326–1350. doi: 10.1175/JCLI3339.1

Hara M, Yoshikane T, Takahashi HG, et al (2009) Assessment of the Diurnal Cycle of Precipitation over the Maritime Continent Simulated by a 20 km Mesh GCM Using TRMM PR Data. J Meteorol Soc Japan 87A:413–424. doi: 10.2151/jmsj.87A.413

Hirai M, Sakashita T, Kitagawa H, Tsuyuki T (2007) Development and Validation of a New Land Surface Model for JMA’s Operational Global Model Using the CEOP Observation Dataset. J Meteorol Soc Japan 85:1–24. doi: 10.2151/jmsj.85A.1

Holtslag a. a. M, De Bruijn EIF, Pan H-L (1990) A High Resolution Air Mass Transformation Model for Short-Range Weather Forecasting. Mon. Weather Rev. 118:1561–1575.

Huang W-R, Chang Y-H, Hsu H-H, et al (2016) Dynamical downscaling simulation and future projection of summer rainfall in Taiwan: Contributions from different types of rain events. J Geophys Res Atmos 121:13,973-13,988. doi: 10.1002/2016JD025643

Huang W-R, Chen K-C (2015) Trends in pre-summer frontal and diurnal rainfall activities during 1982–2012 over Taiwan and Southeast China: characteristics and possible causes. Int J Climatol 35:2608–2619. doi: 10.1002/joc.4159

Huang WR, Chan JCL (2012) Seasonal variation of diurnal and semidiurnal rainfall over Southeast China. Clim Dyn 39:1913–1927. doi: 10.1007/s00382-011-1236-5

Huang WR, Chan JCL, Au-Yeung AYM (2013) Regional climate simulations of summer diurnal rainfall variations over East Asia and Southeast China. Clim Dyn 40:1625–1642. doi: 10.1007/s00382-012-1457-2

Huang WR, Wang SY (2013) Impact of land-sea breezes at different scales on the diurnal rainfall in Taiwan. Clim Dyn 1–13. doi: 10.1007/s00382-013-2018-z

Huffman GJ, Bolvin DT, Nelkin EJ, et al (2007) The TRMM Multisatellite Precipitation Analysis (TMPA): Quasi-Global, Multiyear, Combined-Sensor Precipitation Estimates at Fine Scales. J Hydrometeorol 8:38–55. doi: 10.1175/JHM560.1

Ichikawa H, Masunaga H, Tsushima Y, Kanzawa H (2012) Reproducibility by climate models of cloud radiative forcing associated with tropical convection. J Clim 25:1247–1262. doi: 10.1175/JCLI-D-11-00114.1

Ichikawa H, Yasunari T (2008) Intraseasonal variability in diurnal rainfall over New Guinea and the surrounding oceans during austral summer. J Clim 21:2852–2868. doi: 10.1175/2007JCLI1784.1

Ichikawa H, Yasunari T (2006) Time-space characteristics of diurnal rainfall over Borneo and surrounding oceans as observed by TRMM-PR. J Clim 19:1238–1260. doi: 10.1175/JCLI3714.1

Im E-S, Ahn J-B, Remedio AR, Kwon W-T (2008) Sensitivity of the regional climate of East/Southeast Asia to convective parameterizations in the RegCM3 modelling system. Part 1: Focus on the Korean peninsula. Int J Climatol 28:1861–1877. doi: 10.1002/joc.1664

IPCC (2012) Managing the risks of extreme events and disasters to advance climate change adaptation.

Japan Meteorological Agency (2007) Outline of the operational numerical weather prediction at the Japan Meteorological Agency (Appendix to WMO numerical weather prediction progress report).

Jiang H, Zipser EJ (2010) Contribution of Tropical Cyclones to the Global Precipitation from Eight Seasons of TRMM Data: Regional, Seasonal, and Interannual Variations. J Clim 23:1526–1543. doi: 10.1175/2009JCLI3303.1

Jiang Z, Song J, Li L, et al (2012) Extreme climate events in China: IPCC-AR4 model evaluation and projection. Clim Change 110:385–401. doi: 10.1007/s10584-011-0090-0

Kamiguchi K, Arakawa O, Kitoh A, et al (2010) Development of APHRO_JP, the first Japanese high-resolution daily precipitation product for more than 100 years. Hydrol Res Lett 4:60–64. doi: 10.3178/hrl.4.60

Kharin V V., Zwiers FW (2005) Estimating extremes in transient climate change

simulations. J Clim 18:1156–1173. doi: 10.1175/JCLI3320.1

Kiehl JT, Hack JJ, Bonan GB, et al (1996) Description of the NCAR Community Climate Model (CCSM3). NCAR Tech Note NCAR/TN-420+STR. doi: 10.5065/D6FF3Q99

Kikuchi K, Wang B (2008) Diurnal precipitation regimes in the global tropics. J Clim 21:2680–2696. doi: 10.1175/2007JCLI2051.1

Klein Tank AMG, Zwiers FW, Zhang X (2009) Guidelines on Analysis of extremes in a changing climate in support of informed decisions for adaptation. Clim Data Monit 52.

Knutson TR, McBride JL, Chan J, et al (2010) Tropical cyclones and climate change. Nat Geosci 3:157–163. doi: 10.1038/ngeo779

Knutson TR, Sirutis JJ, Garner ST, et al (2008) Simulated reduction in Atlantic hurricane frequency under twenty-first-century warming conditions. Nat Geosci 1:359–364. doi: 10.1038/ngeo202

Knutson TR, Sirutis JJ, Zhao M, et al (2015) Global projections of intense tropical cyclone activity for the late twenty-first century from dynamical downscaling of CMIP5/RCP4.5 scenarios. J Clim 28:7203–7224. doi: 10.1175/JCLI-D-15-0129.1

Kossin JP, Emanuel KA, Camargo SJ (2016) Past and Projected Changes in Western North Pacific Tropical Cyclone Exposure. J Clim JCLI-D-16-0076.1. doi: 10.1175/JCLI-D-16-0076.1

Lau K-M, Wu H-T (2007) Detecting trends in tropical rainfall characteristics, 1979-2003. Int J Climatol 27:979–988. doi: 10.1002/joc

Lenderink G, van Meijgaard E (2008) Increase in hourly precipitation extremes beyond expectations from temperature changes. Nat Geosci 1:511–514. doi:

10.1038/ngeo262

Li Y Bin, Tam CY, Huang WR, et al (2016) Evaluating the impacts of cumulus, land surface and ocean surface schemes on summertime rainfall simulations over East-to-southeast Asia and the western north pacific by RegCM4. Clim Dyn 46:2487–2505. doi: 10.1007/s00382-015-2714-y

Manganello J V., Hodges KI, Dirmeyer B, et al (2014) Future changes in the western North Pacific tropical cyclone activity projected by a multidecadal simulation with a 16-km global atmospheric GCM. J Clim 27:7622–7646. doi: 10.1175/JCLI-D-13-00678.1

Mapes BE, Warner TT, Xu M (2003) Diurnal Patterns of Rainfall in Northwestern South America. Part III: Diurnal Gravity Waves and Nocturnal Convection Offshore. Mon Weather Rev 131:830–844. doi: 10.1175/1520-0493(2003)131<0830:DPORIN>2.0.CO;2

Masson S, Terray P, Madec G, et al (2012) Impact of intra-daily SST variability on ENSO characteristics in a coupled model. Clim Dyn 39:681–707. doi: 10.1007/s00382-011-1247-2

Meehl GA, Zwiers F, Evans J, et al (2000) Trends in extreme weather and climate events: Issues related to modeling extremes in projections of future climate change. Bull Am Meteorol Soc 81:427–436. doi: 10.1175/1520-0477(2000)0812.3.co;2

Mellor GL, Yamada T (1974) A Hierarchy of Turbulence Closure Models for Planetary Boundary Layers. J. Atmos. Sci. 31:1791–1806.

Min S-K, Zhang X, Zwiers FW, Hegerl GC (2011) Human contribution to more-intense precipitation extremes. Nature 470:378–381. doi: 10.1038/nature09763

Mizuta R, Yoshimura H, Endo H, et al (2012) Climate Simulations Using MRI-

AGCM3.2 with 20-km Grid. J Meteorol Soc Japan 90:233–258. doi: 10.2151/jmsj.2012-A12

Mori S, Jun-Ichi H, Tauhid YI, et al (2004) Diurnal Land–Sea Rainfall Peak Migration over Sumatera Island, Indonesian Maritime Continent, Observed by TRMM Satellite and Intensive Rawinsonde Soundings. Mon Weather Rev 132:2021–2039. doi: 10.1175/1520-0493(2004)132<2021:DLRPMO>2.0.CO;2

Murakami H, Wang B, Kitoh A (2011) Future change of western North Pacific typhoons: Projections by a 20-km-mesh global atmospheric model. J Clim 24:1154–1169. doi: 10.1175/2010JCLI3723.1

Murakami H, Wang Y, Yoshimura H, et al (2012) Future changes in tropical cyclone activity projected by the new high-resolution MRI-AGCM. J Clim 25:3237–3260. doi: 10.1175/JCLI-D-11-00415.1

Oh SG, Park JH, Lee SH, Suh MS (2014) Assessment of the RegCM4 over East Asia and future precipitation change adapted to the RCP scenarios. J Geophys Res Atmos 119:2913–2927. doi: 10.1002/2013JD020693

Oleson KW, Lawrence DM, Gordon B, et al (2010) Technical Description of version 4 . 0 of the Community Land Model (CLM).

Oleson KW, Niu GY, Yang ZL, et al (2008) Improvements to the community land model and their impact on the hydrological cycle. J Geophys Res Biogeosciences. doi: 10.1029/2007JG000563

Pal JS, Small EE, Eltahir E a. B (2000) Simulation of regional-scale water and energy budgets: Representation of subgrid cloud and precipitation processes within RegCM. J Geophys Res Atmos 105:29579–29594. doi: 10.1029/2000JD900415

Pall P, Allen MR, Stone DA (2007) Testing the Clausius-Clapeyron constraint on

changes in extreme precipitation under CO2 warming. Clim Dyn 28:351–363. doi: 10.1007/s00382-006-0180-2

Ploshay JJ, Lau N-C (2010) Simulation of the Diurnal Cycle in Tropical Rainfall and Circulation during Boreal Summer with a High-Resolution GCM. Mon Weather Rev 138:3434–3453. doi: 10.1175/2010MWR3291.1

Qian W, Kang HS, Lee DK (2002) Distribution of seasonal rainfall in the East Asian monsoon region. Theor Appl Climatol 73:151–168. doi: 10.1007/s00704-002-0679-3

Qian W, Lin X (2005) Regional trends in recent precipitation indices in China. Meteorol Atmos Phys 90:193–207. doi: 10.1007/s00703-004-0101-z

Randall DA, Harshvardhan, Dazlich DA (1991) Diurnal Variability of the Hydrologic Cycle in a General Circulation Model. J. Atmos. Sci. 48:40–62.

Rayner NA, Parker DE, Horton EB, et al (2003) Global analyses of sea surface temperature, sea ice, and night marine air temperature since the late nineteenth century. J Geophys Res 108:4407. doi: 10.1029/2002JD002670

Ruppert JH (2016) Diurnal timescale feedbacks in the tropical cumulus regime. J Adv Model Earth Syst 8:1483–1500. doi: 10.1002/2016MS000713

Saito K, Keenan T, Holland G, Puri K (2001) Numerical Simulation of the Diurnal Evolution of Tropical Island Convection over the Maritime Continent. Mon Weather Rev 129:378–400. doi: 10.1175/1520-0493(2001)129<0378:NSOTDE>2.0.CO;2

Satomura T (2000) Diurnal Variation of Precipitation over the indo-China Peninsula-Two-dimensional numerical simulation.pdf. J Meteorol Soc Japan 78:461.

Semenov V, Bengtsson L (2002) Secular trends in daily precipitation characteristics: Greenhouse gas simulation with a coupled AOGCM. Clim Dyn 19:123–140.

doi: 10.1007/s00382-001-0218-4

Shige S, Satomura T (2000) The gravity wave response in the troposphere around deep convection. J Meteorol Soc Japan 78:789–801.

Sillmann J, Kharin V V., Zwiers FW, et al (2013) Climate extremes indices in the CMIP5 multimodel ensemble: Part 2. Future climate projections. J Geophys Res Atmos 118:2473–2493. doi: 10.1002/jgrd.50188

Sillmann J, Roeckner E (2008) Indices for extreme events in projections of anthropogenic climate change. Clim Change 86:83–104. doi: 10.1007/s10584-007-9308-6

Sohn SJ, Tam CY, Ashok K, Ahn JB (2012) Quantifying the reliability of precipitation datasets for monitoring large-scale East Asian precipitation variations. Int J Climatol 32:1520–1526. doi: 10.1002/joc.2380

Solomon S, Qin D, Manning M, et al (2007) Climate change 2007-the physical science basis: Working group I contribution to the fourth assessment report of the IPCC. Cambridge University Press

Steiner AL, Pal JS, Rauscher SA, et al (2009) Land surface coupling in regional climate simulations of the West African monsoon. Clim Dyn 33:869–892. doi: 10.1007/s00382-009-0543-6

Sugi M, Murakami H, Yoshimura J (2009) A Reduction in Global Tropical Cyclone Frequency due to Global Warming. Sola 5:164–167. doi: 10.2151/sola.2009-042

Sun Y, Solomon S, Dai A, Portmann RW (2007) How often will it rain? J Clim 20:4801–4818. doi: 10.1175/JCLI4263.1

Takahashi HG, Fujinami H, Yasunari T, Matsumoto J (2010) Diurnal rainfall pattern observed by Tropical Rainfall Measuring Mission Precipitation Radar (TRMM-

PR) around the Indochina peninsula. J Geophys Res 115:D07109. doi: 10.1029/2009JD012155

Vecchi GA, Soden BJ (2007) Global warming and the weakening of the tropical circulation. J Clim 20:4316–4340. doi: 10.1175/JCLI4258.1

Wang Y, Zhou L (2005) Observed trends in extreme precipitation events in China during 1961-2001 and the associated changes in large-scale circulation. Geophys Res Lett 32:1–4. doi: 10.1029/2005GL022574

Wilby R, Wigley TML (1997) Downscaling general circulation model output: a review of methods and limitations. Prog Phys Geogr 21:530–548.

Wilby RL, Wigley TML (2002) Future changes in the distribution of daily precipitation totals across North America. Geophys Res Lett 29:1135. doi: 10.1029/2001gl013048

Wu L, Chou C, Chen C-T, et al (2014) Simulations of the Present and Late-Twenty-First-Century Western North Pacific Tropical Cyclone Activity Using a Regional Model. J Clim 27:3405–3424. doi: 10.1175/JCLI-D-12-00830.1

Wu P, Hamada J-I, Mori S, et al (2003) Diurnal Variation of Precipitable Water over a Mountainous Area of Sumatra Island. J Appl Meteorol 42:1107–1115. doi: 10.1175/1520-0450(2003)042<1107:DVOPWO>2.0.CO;2

Xie P, Yatagai A, Chen M, et al (2007) A Gauge-Based Analysis of Daily Precipitation over East Asia. J Hydrometeor 8:607–626. doi: 10.1175/JHM583.1

Yang GY, Slingo J (2001) The diurnal cycle in the tropics. Mon Weather Rev 129:784–801. doi: 10.1175/1520-0493(2001)129<0784:TDCITT>2.0.CO;2

Yatagai A, Yasutomi N, Hamada A, et al (2012) APHRODITE : Constructing a Long-term Daily Gridded Precipitation Dataset for Asia Based on a Dense

Network of Rain Gauges. 14:6995. doi: 10.1175/BAMS-D-11-00122.1

Yin S, Chen D, Xie Y (2009) Diurnal variations of precipitation during the warm season over China. Int J Climatol 29:1154–1170. doi: 10.1002/joc.1758

Yokoi S, Takayabu YN, Chan JCL (2009) Tropical cyclone genesis frequency over the western North Pacific simulated in medium-resolution coupled general circulation models. Clim Dyn 33:665–683. doi: 10.1007/s00382-009-0593-9

Yukimoto S, Yoshimura H, Hosaka M, et al (2011) Meteorological Research Institute-Earth System Model Version 1 (MRI-ESM1). Tech Reports 64:88. doi: 10.11483/mritechrepo.64

Zanis P, Douvis C, Kapsomenakis I, et al (2009) A sensitivity study of the Regional Climate Model (RegCM3) to the convective scheme with emphasis in central eastern and southeastern Europe. Theor Appl Climatol 97:327–337. doi: 10.1007/s00704-008-0075-8

Zeng X, Beljaars A (2005) A prognostic scheme of sea surface skin temperature for modeling and data assimilation. Geophys Res Lett 32:1–4. doi: 10.1029/2005GL023030

Zeng X, Zhao M, Dickinson RE (1998) Intercomparison of bulk aerodynamic algorithms for the computation of sea surface fluxes using TOGA COARE and TAO data. J Clim 11:2628–2644. doi: 10.1175/1520-0442(1998)011<2628:IOBAAF>2.0.CO;2

Zhai P, Zhang X, Wan H, Pan X (2005) Trends in total precipitation and frequency of daily precipitation extremes over China. J Clim 18:1096–1108. doi: 10.1175/JCLI-3318.1

Zhang L, Karnauskas KB, Donnelly JP, Emanuel K (2017) Response of the North Pacific tropical cyclone climatology to global warming: Application of

dynamical downscaling to CMIP5 models. J Clim 30:1233–1243. doi: 10.1175/JCLI-D-16-0496.1

Zhang X, Alexander L, Hegerl GC, et al (2011) Indices for monitoring changes in extremes based on daily temperature and precipitation data. Wiley Interdiscip Rev Clim Chang 2:851–870. doi: 10.1002/wcc.147

Zhao M, Held IM, Lin S-J (2012) Some Counterintuitive Dependencies of Tropical Cyclone Frequency on Parameters in a GCM. J Atmos Sci 69:2272–2283. doi: 10.1175/JAS-D-11-0238.1

Zhao T, Yatagai A (2014) Evaluation of TRMM 3B42 product using a new gauge-based analysis of daily precipitation over China. 2762:2749–2762. doi: 10.1002/joc.3872

Zhou L, Wang Y (2006) Tropical rainfall measuring mission observation and regional model study of precipitation diurnal cycle in the New Guinean region. J Geophys Res Atmos 111:1–18. doi: 10.1029/2006JD007243

Zou L, Qian Y, Zhou T, Yang B (2014) Parameter tuning and calibration of RegCM3 with MIT-emanuel cumulus parameterization scheme over CORDEX East Asia domain. J Clim 27:7687–7701. doi: 10.1175/JCLI-D-14-00229.1

Zou L, Zhou T (2013) Improve the simulation of western North Pacific summer monsoon in RegCM3 by suppressing convection. Meteorol Atmos Phys 121:29–38. doi: 10.1007/s00703-013-0255-7

Zwiers FW, Alexander L V, Hegerl GC, et al (2013) Climate Extremes: Challenges in Estimating and Understanding Recent Changes in the Frequency and Intensity of Extreme Climate and Weather Events. Springer 339–389. doi: 10.1007/978-94-007-6692-1